DESIGN AND MANUFACTURING OF AN ULTRA-LIGHTWEIGHT SEMI-RIGID INDOOR AIRSHIP FOR UNDERGROUND EXPLORATION

by

Afsaneh KHEIRANI

MANUSCRIPT-BASED THESIS PRESENTED TO ÉCOLE DE TECHNOLOGIE SUPÉRIEURE
IN PARTIAL FULFILLMENT OF A MASTER'S DEGREE
WITH THESIS IN MECHANICAL ENGINEERING
M.A.Sc.

MONTREAL, FEBRUARY 9, 2026

ÉCOLE DE TECHNOLOGIE SUPÉRIEURE
UNIVERSITÉ DU QUÉBEC

BOARD OF EXAMINERS

THIS THESIS HAS BEEN EVALUATED

BY THE FOLLOWING BOARD OF EXAMINERS

Mr. David St-Onge, Thesis supervisor
Department of Mechanical Engineering, École de Technologie Supérieure

Mr. Ilyass Tabiai, Thesis Co-Supervisor
Department of Mechanical Engineering,École de technologie supérieure

Ms. Martine Dubé, Chair, Board of Examiners
Department of Mechanical Engineering, École de Technologie Supérieure

Mr. Mohammed Jahazi, Member of the Jury
Department of Mechanical Engineering, École de Technologie Supérieure

THIS THESIS WAS PRESENTED AND DEFENDED

IN THE PRESENCE OF A BOARD OF EXAMINERS AND THE PUBLIC

ON JANUARY 27, 2026

AT ÉCOLE DE TECHNOLOGIE SUPÉRIEURE

ACKNOWLEDGEMENTS

I would first like to express my deepest gratitude to my supervisors, Professor David St-Onge and Professor Ilyass Tabiai, for their guidance, availability, and support throughout this research. Their insightful feedback and encouragement have been invaluable in the completion of this thesis. I am especially thankful for their patience with my many iterations, for their openness to unconventional ideas, and for constantly challenging me to refine my work. I also gratefully acknowledge the financial support of the Fonds de recherche du Québec – Nature et technologies (FRQNT), through the Team Research Project grant, which made this work possible.

I am equally indebted to the technical staff at ÉTS for their precious assistance in accessing laboratory resources and experimental facilities. In particular, I would like to acknowledge Serge Plamondon, Mario Corbin, and Mohammad Saadati, whose expertise, generosity with their time, and willingness to share practical knowledge made a significant difference throughout this project.

I extend my thanks to my colleagues at the INIT Robots Lab[1] and the LIPEC Lab[2] for their support, camaraderie, and for making the lab a place of both learning and friendship. I am also grateful for the many collaborations and discussions with other laboratories and partners, including the NXI Gestatio[3] (Prof. Reeves) at UQAM, which enriched the scope and creativity of this research.

Finally, I would like to express my heartfelt gratitude to my family for their constant encouragement, and above all, to my husband, Mojtaba, whose love, patience, and support have been a continuous source of strength throughout this journey.

---

[1] https://initrobots.ca/equipe

[2] https://www.etsmtl.ca/en/labs/lipec

[3] https://www.nxigestatio.org

To my wonderful husband, whose love and support made it possible for me to lock myself in my office for days at a time to complete research, coursework, and writing, yet still return to a loving home. And for the fortunate circumstances and timely opportunities that helped everything fall into place.

CONCEPTION ET FABRICATION D'UN DIRIGEABLE D'INTÉRIEUR SEMI-RIGIDE ULTRA-LÉGER POUR L'EXPLORATION SOUTERRAINE

Afsaneh KHEIRANI

RÉSUMÉ

L'exploration robotique d'environnements confinés ou dangereux – tels que les tunnels, les installations industrielles et les cavernes souterraines – demeure limitée par les contraintes d'endurance, de sécurité et de perturbation associées aux plateformes aériennes conventionnelles. Bien que les drones multirotors offrent un contrôle précis et une capacité de vol stationnaire, leur dépendance à une poussée continue restreint fortement la durée de vol et la capacité utile. Les plateformes LTA constituent une alternative prometteuse. En générant la portance par flottabilité plutôt que par propulsion, elles permettent une consommation énergétique réduite, une perturbation aérodynamique minimale et une interaction intrinsèquement plus sûre avec leur environnement.

Alors que d'importants progrès ont été réalisés dans la conception de grands dirigeables pour des missions stratosphériques ou captives – où la charge utile et l'endurance dominent les priorités de conception –, les Lighter-Than-Air (LTA) d'intérieur opèrent à une échelle beaucoup plus réduite (environ un mètre cube), ce qui leur permet d'évoluer dans des couloirs étroits et à travers des passages confinés. À cette échelle, des contraintes de masse très strictes signifient que même une légère augmentation de la masse structurelle réduit la charge utile et l'autonomie. L'enveloppe, pouvant représenter plus de 30% de la portance disponible, devient ainsi le composant le plus critique déterminant la performance et la fiabilité globales du système.

Cette thèse relève ces défis à travers une étude expérimentale et numérique intégrée portant sur le développement d'enveloppes de dirigeables d'intérieur à la fois robustes et ultra-légères. La caractérisation mécanique de matériaux candidats a conduit à la mise au point d'une bladder polymère enduite, optimisée pour une masse minimale, une durabilité mécanique accrue et une meilleure rétention du gaz, adaptée aux environnements de mission exigeants. En complément, un cadre de modélisation par éléments finis a été développé dans Abaqus/Explicit afin d'évaluer les réponses structurelles sous pressurisation et lors d'impacts à basse vitesse contre des obstacles environnementaux, en comparant des enveloppes purement gonflables à des conceptions semi-rigides renforcées par des squelettes légers destinés à protéger le système de vol dans des milieux encombrés.

Les résultats démontrent que le renforcement semi-rigide atténue efficacement la déformation et les dommages lors des impacts, permettant à l'enveloppe de conserver son intégrité structurelle et de continuer à fonctionner tout en préservant les marges de flottabilité. La bladder développée présente un excellent compromis entre résistance mécanique et perméabilité, et elle a été validée avec succès lors d'une mission d'exploration souterraine, confirmant ses performances au-delà des essais en laboratoire. Les principales contributions de ce travail incluent (i) une nouvelle base de données des propriétés mécaniques des membranes ultrafines comparées à des matériaux conventionnels, (ii) la conception brevetée d'une bladder enduite destinée aux plateformes LTA

d'intérieur, et (iii) un cadre de simulation d'impact reproductible pour les configurations de systèmes LTA semi-rigides et non rigides. Dans l'ensemble, cette recherche fait progresser le développement d'une nouvelle génération de véhicules LTA d'intérieur capables d'évoluer de manière sûre, persistante et économe en énergie dans des environnements auparavant inaccessibles.

Mots-clés: Dirigeable plus léger que l'air (LTA), Robotique d'intérieur, Structures gonflables, Simulation par éléments finis, Impact, Enveloppe semi-rigide

DESIGN AND MANUFACTURING OF AN ULTRA-LIGHTWEIGHT SEMI-RIGID INDOOR AIRSHIP FOR UNDERGROUND EXPLORATION

Afsaneh KHEIRANI

ABSTRACT

Robotic exploration of confined or hazardous environments, such as tunnels, industrial interiors, and underground caverns, remains constrained by the endurance, safety, and disturbance limits of conventional aerial platforms. Although multirotor drones offer precise control and hovering capability, their reliance on continuous thrust severely limits flight duration and payload capacity. Lighter-Than-Air (LTA) airship platforms offer a promising alternative. By generating lift through buoyancy rather than propulsion, they enable lower energy consumption, reduced aerodynamic disturbance, and inherently safer operation.

While significant progress has been made in the design of large, outdoor airships for stratospheric or tethered missions, where payload and endurance dominate design priorities, indoor LTAs operate at a drastically smaller scale (approximately one cubic meter), enabling navigation through narrow corridors and doorways. At this scale, stringent weight constraints mean that even marginal increases in structural mass reduce useful payload and endurance. The envelope, which can account for more than 30% of available lift, therefore becomes the most critical component governing overall system performance and reliability.

This thesis addresses these challenges through an integrated experimental and numerical investigation of robust but ultra-light indoor airship envelopes. Mechanical characterization of candidate materials led to the development of a coated polymer envelope optimized for minimal mass, mechanical durability, and improved gas retention, suitable for use in harsh mission environments. Complementing this effort, a finite element modeling framework was established in Abaqus/Explicit to evaluate structural responses under pressurization and low-velocity impact with environmental obstacles, comparing purely inflatable envelopes with semi-rigid designs reinforced by lightweight skeletons intended to protect the flight system in cluttered environments.

The findings demonstrate that semi-rigid reinforcement effectively mitigates deformation and damage during impacts, allowing the envelope to maintain structural integrity and continue operating while preserving buoyancy margins. The developed envelope achieved an excellent balance between strength and permeability and was successfully validated during an underground exploration mission, confirming performance beyond laboratory testing. The main contributions of this work include (i) a new dataset of mechanical properties for ultra-thin membranes benchmarked against conventional materials, (ii) a patented coated envelope design for indoor LTA platforms, and (iii) a reproducible impact simulation framework for semi-rigid and non-rigid LTA system configurations. Collectively, this research advances the development of next-generation indoor LTA vehicles capable of persistent, safe, and energy-efficient operation in previously inaccessible environments.

Keywords: Lighter-Than-Air Airship (LTA), Indoor robotics, Inflatable structures, finite element analysis (FEM) simulation, Impact, semi-rigid envelope

TABLE OF CONTENTS

Page

INTRODUCTION 1

CHAPTER 1 LITERATURE REVIEW 3
1.1 Outdoor versus indoor airship design requirements 5
1.2 Airship Shapes 7
1.3 Structural and Envelope Classification 8
1.4 Envelope joining methods and seam behavior 13
1.5 Indoor airships versus multicopters 14
1.6 Indoor LTA Vehicle Design Challenges 15
1.7 Structure of the dissertation 17

CHAPTER 2 OBJECTIVE AND METHODOLOGY 21
2.1 Objective 1: Development of an ultralight coated envelope for indoor airship envelopes 21
2.1.1 Experimental Tools 22
2.2 Objective 2: Design of an airship simulation for impact and damage assessment to protect the thin envelope 22
2.2.1 Modeling Tools 23

CHAPTER 3 VEHICLE ENVELOPE WITH LIGHTWEIGHT ULTRA-FILM FOR MINIMAL LEAKAGE (VELUM) 25
3.1 Abstract 25
3.2 Introduction 26
3.3 Background: Membrane performance 29
3.4 Materials and Methods 33
3.4.1 Density and Thickness Measurements 33
3.4.2 Tear Test 34
3.4.3 Puncture Test 35
3.4.4 Tensile Strength of Sealed Joints 35
3.4.5 Gas Barrier Test 36
3.4.6 Wettability Properties 37
3.4.7 Thermal Welding 38
3.4.8 Validation of Burt Behavior 39
3.5 Fabrication of Coated LDPE Membranes 40
3.5.1 Gore Preparation 40
3.5.2 LDPE Envelope Thermal Welding 41
3.5.3 Surface Coating 42
3.6 Results and Discussion 45
3.6.1 Density Measurements 45
3.6.2 Tear Test 47

3.6.3 Puncture Test 47
3.6.4 Tensile Strength of welded joints 47
3.6.5 High specific strength 48
3.6.6 Gas Barrier Test 48
3.6.7 Wettability Properties 49
3.6.8 Thermal Welding Test 50
3.6.9 Validation of Burt Behavior 50
3.7 Field Demonstration 51
3.8 Conclusion 55
3.9 Acknowledgements 56

CHAPTER 4 FINITE ELEMENT SIMULATION OF SLTA ENVELOPES: NON-RIGID VS. SEMI-RIGID STRUCTURES 57
4.1 Introduction 57
4.2 Explicit Dynamic Analysis for thin-wall membranes 57
4.3 Model Geometry and Discretization 58
4.3.1 Main bladder 59
4.3.2 Bladder exoskeleton 62
4.3.3 Rigid Obstacle 63
4.4 Pressurization Behavior Analysis 64
4.4.1 Internal Pressurization Modeling 64
4.4.2 Mesh convergence evaluation and time-period selection 65
4.4.3 Interaction Modeling (system II) 67
4.4.4 Boundary Condition at Pressurization 68
4.5 Impact Behavior Analysis 70
4.5.1 Boundary Condition at Impact 71
4.5.2 Impact step duration and time-window selection 73
4.5.3 Load 75
4.6 Results and Discussion 76
4.6.1 Stress and global deformation at pressurization 76
4.6.2 Stress and global deformation at impact 79
4.6.3 Impact visualization and experimental reference 83
4.7 Structural behavior and operational implications for SLTA Operation 84

CONCLUSION AND RECOMMENDATIONS 87

APPENDIX I FACILITIES 91

APPENDIX II ABAQUS MODELING DETAILS 93

BIBLIOGRAPHY 99

LIST OF TABLES

Page

Table 1.1 Literature-based comparison of commonly used indoor airship envelope membranes. Each entry summarizes reported advantages and limitations relative to key requirements for ultra-light indoor LTA platforms. 12

Table 1.2 Comparison overview of an indoor LTA airship and a multicopter. 20

Table 3.1 Gas permeability of different polymeric and elastomeric film materials used for LTA envelope applications at standard testing conditions. Taken from Joshi, Adak & Butola (2018); Shamini & Yusoh (2014). 32

Table 3.2 Initial Weights of LDPE, PU, and Mylar Pillows for Gas Barrier Evaluation 37

Table 3.3 Physical properties of selected materials: Mylar (silver), PU (white), and LDPE pure / coated (transparent). Reported density values correspond to mean values obtained from helium pycnometry (ten repetitions per sample; standard deviations were 0.0065, 0.0160, and 0.0044 g/cm^3 for Mylar, PU, and LDPE, respectively), and thickness was determined with a digital micrometer (0.001 mm device resolution, five measurements per sample). All measurements were conducted at ambient temperature (about 25 °C). 46

Table 3.4 Normalized strength-to-weight ratios for envelope materials (tear, puncture, and tensile performance), calculated as force (N) divided by surface density (g/m^2). The higher these values, the more mechanically efficient the material is for lightweight airship applications. 48

Table 3.5 Decision matrix for material selection, comparing LDPE, PU, and Mylar across key parameters. Final ranking indicates overall performance for specific applications. 53

Table 3.6 Performance parameters for single-body indoor airships made from LDPE and PU, highlighting key metrics for material suitability. 54

Table 4.1 Geometrical parameters of the bladder and bladder exoskeleton (in SI units). 60

Table 4.2 Mechanical properties of the LDPE implemented in simulation. 61

Table 4.3 Material properties of the exoskeleton (carbon tube). 62

Table 4.4 Summary of peak stress and deformation metrics during the pressurization step for system I and system II. 78

Table 4.5 Summary of peak stress, deformation, and internal energy metrics during the impact step for system I and system II. 82

LIST OF FIGURES

Page

Figure 1.1 (a) Conventional shape airships. (b) Unconventional shape airships. Adapted from Lobner (2024a, p. 9–81) and Stockbridge, Ceruti & Marzocca (2012, p. 175). 7

Figure 1.2 (a) Cutaway view of a typical non-rigid airship (blimp), showing internal ballonets and an envelope maintained solely by gas pressure. (b) Cutaway view of a typical rigid airship (zeppelin), showing an internal framework and multiple gas cells. Taken from Stockbridge *et al.* (2012) 9

Figure 3.1 Tear test methodology: (a) Double-notch specimen geometry prepared in compliance with ASTM D1004 standards. Experimental setup for evaluating tear resistance in (b) PU film, (c) LDPE film, and (d) Mylar film. 34

Figure 3.2 Joint configurations used in the sealed-joint tensile tests (ASTM F88/F88M-21): (a) T1, superimposed joint configuration; (b) T2, flap joint configuration. These labels (T1 and T2) are used throughout the paper to identify the tensile test configuration. The figure presents visual representations of these two joint configurations, which are commonly used in structural applications. Understanding the differences between these joint types is essential for selecting appropriate joining methods in engineering design. 35

Figure 3.3 Representative tensile specimens prepared according to ASTM F88/F88M-21, showing the tested material–configuration combinations: (a) LDPE, configuration T1 (superimposed joint); (b) LDPE, configuration T2 (flap joint); (c) PU, configuration T1; (d) Mylar, configuration T1. Only LDPE was tested in both configurations (T1 and T2) to isolate the effect of joint geometry. 36

Figure 3.4 Schematic of load cell setup for helium leakage performance measurement in pillow-shaped samples. The load cell measured the lift force exerted by the pillow, which correlated with internal helium pressure and retention. 38

Figure 3.5 Gas barrier comparison of pillows made from (a) LDPE film, (b) Mylar film, and (c) PU film. All pillows had identical dimensions and were tested under the same conditions, inflated to the same internal pressure,

and placed in a temperature-controlled, isolated room with minimal airflow or external disturbances (e.g., airflow or motion caused by nearby personnel). 38

Figure 3.6 Flowchart illustrating the LDPE airship envelope fabrication process used in this study. The figure outlines the sequential steps involved, from the initial design of the envelope shape to the final quality check and deployment. 40

Figure 3.7 Components and setup for the envelope fabrication process: (a) Heat roller and mattress for thermal welding of gores and auxiliary components; (b) Thermally welded patches; (c) Envelope thermal welding using a custom-made fixture. 43

Figure 3.8 Surface morphology of LDPE samples observed with a VHX-7000 digital microscope: (a) non-coated surface, (b) after spraying, (c) after wiping, and (d) after spray-wipe coating. The spray-wipe method produced the most homogeneous and defect-free layer. 44

Figure 3.9 Coated envelope. The figure illustrates the main steps and resulting appearance of the coating. 45

Figure 3.10 Force–displacement curves from mechanical testing: (a) tear resistance, (b) puncture resistance, and (c) tensile strength of sealed joints. Curves are representative responses from repeated tests; the annotated peak values correspond to the mean of four specimens for each material/configuration. 46

Figure 3.11 Results of gas barrier tests: (a) Helium leakage rates of pillow-shaped envelopes fabricated from LDPE, Mylar, and PU; (b) leakage rates of the same samples after mechanical agitation in a dryer; and (c) leakage rates of full-scale LDPE and PU envelopes. For cases (a) and (b), curves represent mean values obtained from three repeated tests per material. Together, these results highlight the relative effectiveness of each material in limiting gas loss, a critical parameter for assessing their suitability in practical airship applications. 49

Figure 3.12 Mean contact angles of various films, illustrating wettability: (a) Uncoated LDPE film (92.75° ± 1.38°), (b) Fluoro-siloxane sol-gel coated LDPE (117.53° ± 1.89°), (c) PU film (95.88° ± 1.44°), and (d) Mylar film (73.95 ° ± 1.35 °) 50

Figure 3.13 Pressure-time profiles from biaxial inflation burst tests of Mylar, PU, and LDPE envelopes, illustrating inflation behavior and rupture progression under increasing internal pressure. 51

Figure 3.14 Rupture sequences for inflated envelopes (1200 × 800 mm): (a) Mylar, (b) PU, and (c) LDPE. Sequences show key stages of inflation and rupture under biaxial loading, highlighting material-specific rupture initiation, failure modes, and tear propagation. 52

Figure 3.15 Envelope performance during a mission in a cave environment: (a) LDPE envelope with a one-way valve assembled in the laboratory, and (b) PU envelope. 54

Figure 4.1 Airship configurations: (a) non-rigid/system I (main bladder) and (b) semi-rigid/system II (main bladder reinforced with a lightweight exoskeleton). 58

Figure 4.2 Cylindrical body with a heptagonal cross-section, designed by Louis Catar *et al.* within the framework of the same research project (Catar, Tabiai & St-Onge, 2024). 60

Figure 4.3 Finite element geometries used in simulations: (a) inflatable envelope (main bladder) with partitions, (b) exoskeleton, and (c) rigid obstacle for impact testing. 63

Figure 4.4 Finite element meshes used in simulations: (a) bladder with M3D3 elements, (b) exoskeleton with B32 beam elements, and (c) rigid obstacle with R3D3 elements. 64

Figure 4.5 Comparison of the hoop stress component S_{11} in the central cylindrical region for two global mesh sizes (0.03 m and 0.01 m) and three simulation durations (180 s, 60 s, and 30 s). The color contours represent the magnitude of S_{11}, with red indicating higher stress levels and blue indicating lower stress levels. For the cases shown, the maximum stress value is approximately 10.5 MPa and the minimum stress value is approximately −2.6 MPa, as indicated by the contour legends. 66

Figure 4.6 Interaction between the bladder and the exoskeleton: (a) attachment/contact surface on the bladder in the numerical model, (b) attachment patches on the physical bladder in the experiment. 68

Figure 4.7 Inflation sequence of system I (non-rigid), extracted from the evolving von Mises stress field. The color contours represent the magnitude of the von Mises stress during inflation, with minimum and maximum values of approximately 2.05 MPa and 9.4 MPa, respectively. The values are summarized in Table 4.4 69

Figure 4.8 Inflation sequence of system II (semi-rigid), extracted from the evolving von Mises stress field. The maximum von Mises stress reaches 496 MPa (red) in the exoskeleton and 10.4 MPa (red) in the bladder, while the minimum stress value is approximately 0.20 MPa (blue) for both components. The values are summarized in Table 4.4. 70

Figure 4.9 Close-up view of the corner region involved in impact, highlighting local stress concentration, wrinkling, and deformation for system I, system II, and the bladder. The corresponding maximum deformation values are summarized in Table 4.5. 72

Figure 4.10 Impact sequence of the first system (system I). Quantitative peak stress and deformation values corresponding to this impact event are summarized in Table 4.5. 73

Figure 4.11 Impact sequence of the first system (system II). Quantitative peak stress and deformation values corresponding to this impact event are summarized in Table 4.5. 74

Figure 4.12 Maximum displacement magnitude at the pressurization equilibrium state (P = 1500 Pa) for system I and system II. The corresponding quantitative displacement values are summarized in Table 4.4. 77

Figure 4.13 Directional displacement components at the pressurization equilibrium state (P = 1500 Pa) for system I and system II. 78

Figure 4.14 Comparison of maximum von Mises stress at impact. The plot shows stress evolution for system I, system II at the assembly level, and the bladder and exoskeleton components of system II plotted separately. 80

Figure 4.15 Internal energy in system I and system II at impact. 81

Figure 4.16 Experimental impact sequence of a pressurized Mylar pillow impacting a rigid wall, used for qualitative validation of the impact simulation methodology. 83

LIST OF ABBREVIATIONS

ETS	École de Technologie Supérieure
LTA	Lighter Than Air
FEM	Finite Element Methods
VELUM	Vehicle Envelope with Lightweight Ultrafilm for Minimal Leakage
CAE	Computer-Aided Engineering
LDPE	Low-Density Polyethylene
LLDPE	Linear low-density polyethylene
PU	Polyurethane
BoPET	biaxially oriented polyethylene terephthalate (a polyester film).
Mylar	Trade name for BoPET
CAD	Computer-aided design
HTA	heavier-than-air
HAPs	high-altitude platforms
RP	reference point
SLTA	Small Lighter-Than-Air
DOF	Degree of Freedom
SPOS	Surface Positive Orientation (Abaqus)
SNEG	Surface Negative Orientation (Abaqus)
TPU	Thermoplastic Polyurethane

UAV	Unmanned Aerial Vehicle
CA	Static water contact angle
EVOH	Ethylene vinyl alcohol copolymer
GPS	Global Positioning System
HDPE	High-density polyethylene
He	Helium
MFI	Melt flow index
MTS	Mechanical testing system (MTS Alliance RF/200)
PVDC	Polyvinylidene chloride
RF	Radio-frequency
VCA	Video contact angle (system)

LIST OF SYMBOLS AND UNITS OF MEASUREMENTS

m^2	square meter (area)
m	meter (length, thickness, geometric dimensions)
sec	second (time)
kg	kilogram (mass)
kg/m^3	kilogram per cubic meter (density)
Pa	pascal (pressure or stress)
MPa	megapascal
J	joule (energy)
J/m^2	joule per square meter (fracture energy)
t	membrane or bladder thickness
$P(t)$	internal gas pressure as a function of time
P_0	initial internal gas pressure
P_{max}	maximum internal pressure
$V(t)$	internal cavity volume at time t
V_0	initial cavity volume
γ	adiabatic index of the gas ($\gamma = c_p/c_v$)
c_p	specific heat at constant pressure
c_v	specific heat at constant volume
ρ	material density

E	Young's modulus
ν	Poisson's ratio
t	Film thickness
σ	Tensile stress
$\dot{m}_{\mathrm{He}}$	Helium leakage rate (g/h)
$\mathbf{M}$	global mass matrix
$\ddot{\mathbf{u}}$	nodal acceleration vector
$\dot{\mathbf{u}}$	nodal velocity vector
$\mathbf{u}$	nodal displacement vector
$\mathbf{P}^{\mathrm{ext}}$	external force vector
$\mathbf{P}^{\mathrm{int}}$	internal force vector
Δt	explicit time increment
Δt_{crit}	critical stable time increment
L_{min}	smallest characteristic element length
c_d	dilatational wave speed
λ	first Lamé constant
μ	second Lamé constant (shear modulus)
σ	normal stress
σ_{vM}	von Mises equivalent stress
σ_{max}	maximum bladder stress under internal pressurization

S_{11}	longitudinal (hoop) membrane stress component
R_{cyl}	effective radius of the cylindrical section
R_{cap}	effective radius of the end-cap section
U	displacement magnitude
U_1	radial displacement component
U_2	circumferential displacement component
U_3	axial displacement component
U_{max}	maximum displacement magnitude
E_{int}	internal (strain) energy
v_0	initial impact velocity

INTRODUCTION

In recent years, LTA aerial systems, commonly known as airships or aerostats, have re-emerged as promising platforms for civil, defense, and scientific applications. This renewed interest is driven by global efforts toward energy-efficient, low-emission flight and by advances in lightweight materials, autonomous control, and additive manufacturing. Unlike heavier-than-air (HTA) aircraft, such as airplanes and helicopters, LTAs generate lift primarily from buoyancy rather than from aerodynamic lift and thrust alone, enabling sustained flight with minimal power consumption and low vibration. One major advantage of airships is their exceptionally low energy cost: they can hover for extended periods without refueling, and their operational expenses are substantially lower than those of conventional fixed-wing aircraft or rotorcraft (Liao & Pasternak (2009); Shi, Geng & Qian (2019)). These characteristics make them particularly suitable for missions requiring endurance, stability, and precise station-keeping capabilities that are difficult to achieve simultaneously with other types of vehicles.

Airships can operate in outdoor environments exposed to variable atmospheric conditions such as wind, turbulence, and temperature gradients, or in indoor confined spaces where obstacles, limited volume, and restricted access impose additional constraints. While much of the technological development has focused on large outdoor airships for communication, surveillance, or atmospheric observation (Li, Vallabh, Bradford, Kim & Seyam (2022a); Zhai & Euler (2005b)), the potential of LTA technology in confined indoor or subterranean settings remains comparatively underexplored. Yet in many critical scenarios, industrial warehouses, cultural heritage sites, mines, or hazardous facilities, access is challenging for humans and traditional unmanned aerial vehicles (UAVs) due to limited endurance, safety risks, and environmental hazards. In such environments, indoor LTAs offer a promising solution for safe, efficient, and non-intrusive access, especially as advances in materials and autonomy are enabling compact, robust, and long-endurance designs.

In this context, the present thesis focuses on understanding and addressing the specific challenges associated with small lighter-than-air (SLTA) systems intended for indoor operation, to achieve both minimal mass and enhanced structural robustness in demanding mission environments. By analyzing the structural, material, and manufacturing constraints inherent to confined spaces, this work investigates how the intrinsic advantages of buoyant flight can be exploited under stringent mass and volume limitations, an issue that has long been central in aerospace engineering (Hamm, Imtiaz & Raju (2021)). The study introduces the design, fabrication, and testing of an indoor SLTA airship prototype intended for exploration and inspection within narrow, harsh, and underground environments, and presents the technical innovations developed to meet these demanding specifications.

CHAPTER 1

LITERATURE REVIEW

LTA vehicles are flight systems whose overall density is lower than that of the surrounding atmosphere, so that a substantial fraction of their weight is balanced by buoyant lift rather than by aerodynamic lift or rotor thrust. In practice, LTA platforms enclose a volume of low-density lifting gas, typically helium or hydrogen, inside a close envelope, producing a net upward force approximately equal to the weight of the displaced air minus the weight of the gas and structure. This buoyant lift allows LTAs to sustain flight with comparatively low propulsion power, enabling long-endurance missions and quasi-stationary operation that would be energetically prohibitive for conventional HTA aircraft.

Historically, the development of steerable LTA craft (dirigibles/airships) began in the late 19^{th} century. Early pioneers developed non-rigid and semi-rigid dirigibles, while the German Zeppelins later popularized rigid-frame airships during the interwar period. The Hindenburg disaster (1937) marked a turning point (Liu, Zhang, Wang *et al.* (2025)): it was used by political and industrial lobbies to justify regulatory restrictions in several countries, leading to a loss of public confidence and a sharp decline in large-scale airship programs. Despite this setback, airship research persisted in niche domains (military observation, advertising blimps, research platforms), and more recently, a renewed interest has emerged, driven by the need to reduce aviation-related emissions, the availability of advanced lightweight materials and improved design tools, and the emergence of new mission profiles requiring long-endurance, low-disturbance aerial platforms (Liao & Pasternak (2009); Miller, Smith, Johnson *et al.* (2014)). Today, outdoor airships are seen as candidates to fill an operational niche between satellites and conventional fixed-wing or rotorcraft platforms, by offering long-endurance loitering at moderate altitudes with low propulsion power, line-of-sight communications, and relatively large payload capacity at reduced operational cost and vibration (Miller *et al.* (2014)).

Airships can be categorized along several dimensions. From an operational standpoint, airships can be broadly categorized as *outdoor* or *indoor* systems. Structurally, they are often classified

as non-rigid, semi-rigid, or rigid configurations, depending on the presence and extent of internal frameworks and on how the envelope shape is maintained (Liao & Pasternak (2009); Stockbridge *et al.* (2012); Lobner (2024b)). They can also be distinguished by their lift generation method and by their geometric configuration or hull shape. These typologies support consistent comparisons between designs and guide engineering choices related to aerodynamic performance, environmental robustness, and mission suitability.

From a physical standpoint, a typical LTA vehicle comprises four tightly coupled subsystems: the gas-containing envelope (also called hull), internal structural support elements (keels, frames, or load-distribution webs), propulsion and control units (thrusters, control surfaces, and actuation), and the payload and avionics module (Liao & Pasternak (2009); Miller *et al.* (2014)). Among these, the envelope is critical because it simultaneously provides the buoyant volume (acting as the primary barrier between the lifting gas and the surrounding air), the main external aerodynamic surface, and a substantial portion of the load-bearing structure (Zhai & Euler (2005b)). The envelope material must withstand the tensile and bending stresses generated during flight, which enforce practical limits on feasible vehicle size. As internal overpressure increases, it must resist creep, wrinkling, and localized stress concentrations around fittings and seams (Bruyneel, Delsemme, Gort *et al.* (2019)). For these reasons, its performance strongly governs mission feasibility and therefore forms the central focus of this thesis.

Overall LTA performance emerges from the combined behavior of the structural architecture and the envelope membrane. Structural performance determines how loads are distributed, how the vehicle maintains its global shape, and how payloads and control surfaces are supported (Liao & Pasternak (2009)). Envelope performance, by contrast, is defined by coupled mechanical and functional criteria, including mass efficiency (surface density), tensile and tear resistance under biaxial pressurization, puncture tolerance, gas-barrier behavior (helium permeability and leakage), weldability and seam integrity, resistance to environmental effects, and durability under repeated handling and deformation (Zhai & Euler (2005b); Li *et al.* (2022a)). In this context, a well-performing LTA system maintains its intended shape, buoyancy, and operational stability with minimal structural mass and energy expenditure. The remainder of

this chapter uses this coupled structural–envelope perspective to review outdoor and indoor airship designs and to identify the specific material and structural challenges addressed by the present work.

1.1 Outdoor versus indoor airship design requirements

An outdoor airship refers to an LTA vehicle designed to operate freely in the open atmosphere, exposed to external environmental effects such as wind, turbulence, thermal gradients, and solar heating. These airships are typically employed for long-duration missions, including surveillance, communications relay, environmental monitoring, cargo transport, and scientific observation. From an application and industrial perspective, outdoor LTA systems currently dominate the sector, with most commercial and governmental investments focusing on large-scale, long-endurance platforms (Liao & Pasternak (2009); Miller *et al.* (2014)). This market maturity has led to well-established supply chains, robust envelope technologies, and standardized operational frameworks for outdoor missions.

Indoor airships operate in confined spaces, where controllability, collision tolerance, and lightweight construction take precedence over pure aerodynamic efficiency. These vehicles are typically designed for low Reynolds-number regimes, limited ceiling heights, and GPS-denied environments. As a result, indoor airship envelopes commonly adopt near-spherical or low-aspect-ratio geometries. This tendency arises both from physical and structural considerations: in the absence of rigid internal structures, pressurized membranes naturally evolve toward spherical or ellipsoidal shapes, and the sphere provides the optimal surface-to-volume ratio for minimizing envelope mass while maximizing buoyant lift. Soft, collision-tolerant envelopes combined with distributed thrust systems further enable safe operation in proximity to obstacles and infrastructure Mazzei, Teofili, Curti & Gargiulo (2023a); Bhat *et al.* (2024b).

Beyond their geometric differences, outdoor and indoor LTAs diverge fundamentally in terms of design priorities and constraints. Outdoor vehicles must accommodate weather-induced aerodynamic and thermal loads and therefore rely on stiffer structural architectures, multilayer

composite membranes, and higher structural safety margins to maintain stability at larger scales and higher speeds (Tiwari (2024)). Indoor systems, by contrast, operate at drastically smaller volumes, often on the order of one cubic meter, where buoyant lift is inherently limited. This scale introduces a strict mass budget: even modest increases in structural or system mass directly reduce payload capacity and endurance. The environmental scale, therefore, plays a decisive role in design choices. While outdoor airships can tolerate heavier structures because their buoyant volume compensates for added weight, indoor vehicles have almost no such margin, and buoyancy–mass balance becomes the dominant constraint.

Operationally, outdoor platforms are optimized for endurance, altitude capability, and payload performance, whereas indoor vehicles prioritize safe, low-disturbance mobility and precise maneuvering in obstacle-rich spaces. Demonstrations such as inspection operations in the CERN ATLAS detector Mazzei *et al.* (2023a) and collision-tolerant micro-blimp navigation in narrow tunnels Huang, Alonso-Mora & Paull (2019b) exemplify this shift toward lightweight, compliant, and contact-tolerant indoor designs. These contrasting requirements define the broader design landscape and directly motivate the structural, material, and manufacturing strategies examined in the following sections.

Beyond differences in scale, environment, and structural architecture, outdoor and indoor airships also differ in the maturity and scope of the design methodologies commonly applied to them. Large outdoor LTA platforms benefit from decades of development in computational aerodynamics and structural analysis, which have led to established modeling practices for envelope sizing, load assessment, and system integration under environmental loading conditions. These approaches are generally formulated for vehicles with comparatively stiff structures, large buoyant volumes, and well-separated subsystems.

Indoor airships, by contrast, operate at much smaller scales with ultra-light, highly compliant envelopes and tightly constrained mass budgets. At these scales, structural deformation, mass distribution, and vehicle dynamics are inherently more interdependent than in large outdoor platforms. While this coupling is less critical for outdoor vehicles due to their higher structural

stiffness and buoyancy margins, it becomes a defining characteristic of indoor LTA design and directly influences subsequent choices in structure, materials, and system integration.

1.2 Airship Shapes

For airships, the external hull shape strongly influences aerodynamic behavior, internal pressure distribution, and overall flight stability. The most common category, known as **conventional shapes**, includes elongated, asymmetric geometries such as ellipsoidal, cylindrical, or teardrop-like hulls. These configurations provide relatively low drag and efficient internal gas distribution, and form the basis of classical non-rigid and semi-rigid airships (Liao & Pasternak (2009)). Most operational blimps and outdoor airships employ such conventional designs, which balance geometric simplicity and aerodynamic efficiency (Fig. 1.1a).

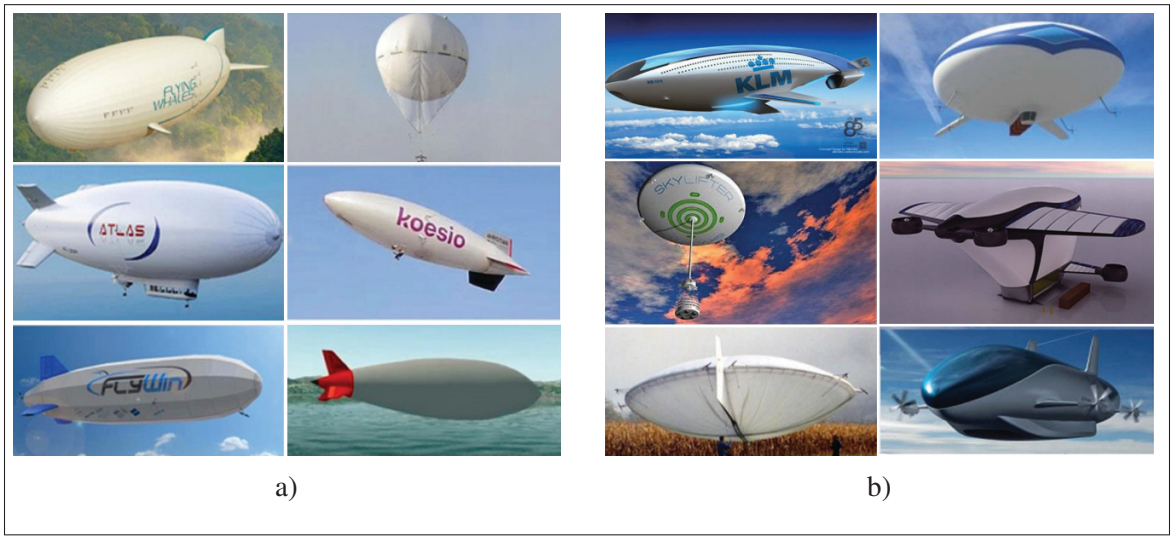

Figure 1.1 (a) Conventional shape airships. (b) Unconventional shape airships. Adapted from Lobner (2024a, p. 9–81) and Stockbridge *et al.* (2012, p. 175).

In contrast, **unconventional shapes** target specialized performance metrics such as improved lift-to-drag ratio, enhanced controllability, or novel payload integration strategies. Notable examples include lenticular (disk-like) hulls, blended lifting bodies, multi-lobed or modular designs, hybrid fuselage–wing configurations, and toroidal concepts such as the “Aeronde ring” airship developed in the early 20th century (Suefuku, Hirayama, Hirakawa & Takayama (2014); Aerospace/LTAS

(2025)). Many of these advanced forms combine buoyant and aerodynamic lift to improve maneuverability and payload performance (Spearman (2002); Taillandier & Farcy (2022)). Recent computational studies have also explored morphing or adaptive envelopes capable of altering their geometry in response to in-flight loading conditions (Eissing, Richter & Schlipf (2022)). Although unconventional geometries remain relatively rare in current fleets, they illustrate the expanding design space and hybridization trends in modern airship architecture. Illustrative examples of such configurations are shown in Fig. 1.1b.

The shape classification in Fig. 1.1 provides one layer of differentiation among airships, emphasizing aerodynamic function and mission role. However, an equally fundamental distinction lies in how the envelope shape is maintained structurally.

1.3 Structural and Envelope Classification

Airships are commonly categorized as non-rigid, semi-rigid, or rigid, based on envelope support and load distribution (Liao & Pasternak (2009); Havill (1974); Harrison (2023)). *Non-rigid airships*, also known as *blimps(non-rigid)*, rely solely on internal gas pressure and balloonets to maintain their form. The bladder(envelope) material carries the tensile loads, and the gondola and tail surfaces are suspended through cables or load-distribution webs. Non-rigid airships are lightweight, inexpensive, and suitable for small to medium volumes, but they are limited in size and structural stiffness (see Fig. 1.2a).

Rigid airships employ an internal structural framework to support the outer envelope. The lifting gas is contained in multiple internal cells, while the outer skin serves primarily as an aerodynamic fairing. This architecture enables very large-scale structures with high payload capacity and well-controlled load paths, at the expense of higher mass and manufacturing complexity. The classic Zeppelins exemplify this category (see Fig. 1.2b).

Semi-rigid airships combine features of both semi-rigid and non-rigid designs, utilizing a stiff keel or partial framework to support the bladder while maintaining its overall shape primarily through gas pressure. Modern examples such as the Zeppelin NT employ this hybrid approach to

combine mechanical robustness with reduced mass (Liao & Pasternak (2009); Taillandier & Farcy (2022)).

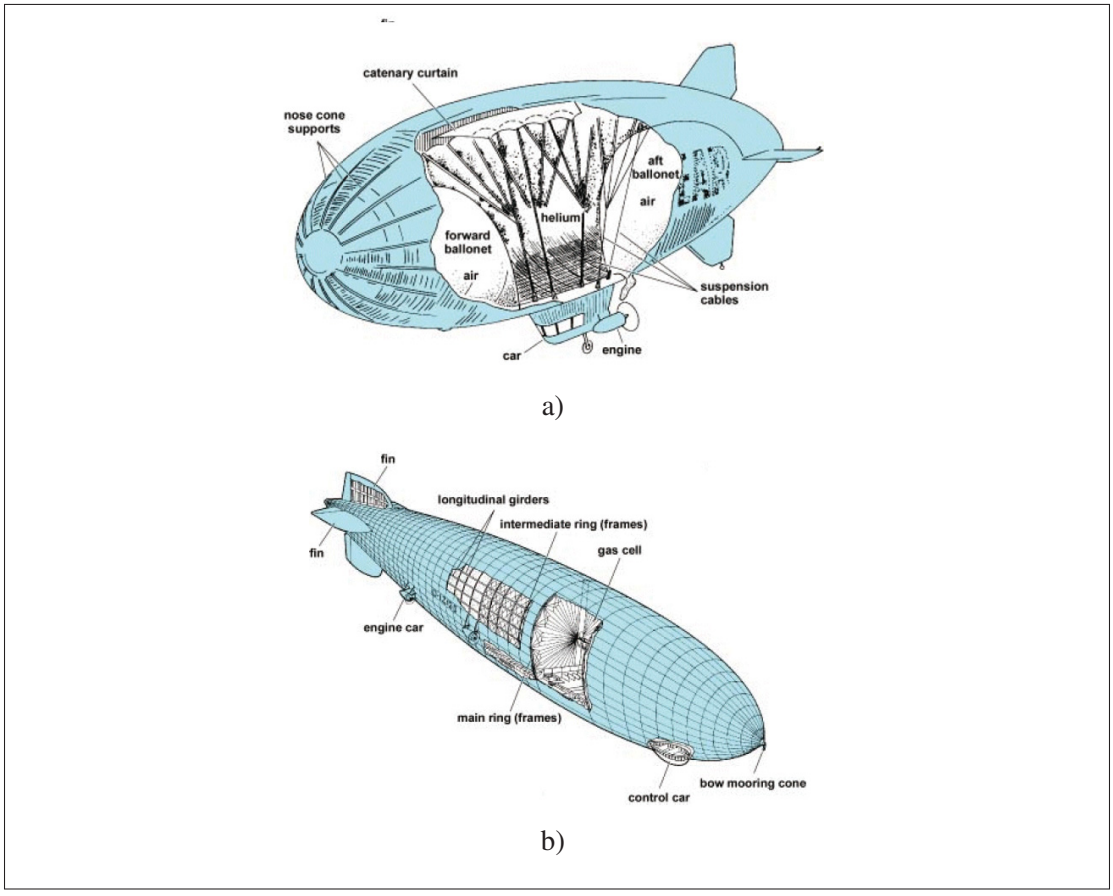

Figure 1.2 (a) Cutaway view of a typical non-rigid airship (blimp), showing internal ballonets and an envelope maintained solely by gas pressure. (b) Cutaway view of a typical rigid airship (zeppelin), showing an internal framework and multiple gas cells. Taken from Stockbridge *et al.* (2012)

Hybrid airships generate lift through both buoyancy and aerodynamics by employing wing-like or lifting-body hulls. Such designs require rigid or semi-rigid frameworks to withstand aerodynamic loads and to support advanced power and control systems; purely non-rigid configurations are generally unsuited to hybrid operation due to the high structural demands (Taillandier & Farcy (2022)). This hybrid approach enables higher payloads, greater operational flexibility, and improved efficiency compared to purely buoyant or purely aerodynamic craft (Hasan (2021); Tatham, Neal & Wu (2017)).

In practice, outdoor airships occupy all of these structural classes, and their realization is closely tied to load and environmental requirements. For large outdoor platforms, these architectures are typically implemented using multilayer composite envelopes reinforced with high-tenacity fabrics and an internal load-bearing exoskeleton whose stiffness is tuned to resist wind, gusts, and manoeuvre loads (Liao & Pasternak (2009); Li *et al.* (2022a); Tiwari (2024)). Most advertising and small surveillance blimps are non-rigid, relying solely on internal gas pressure and fabric strength to maintain their shape (Liao & Pasternak (2009); Stockbridge *et al.* (2012)). Larger operational vehicles, such as the Zeppelin NT, adopt semi-rigid architectures with a keel or partial frame to support payloads and to limit deflection under aerodynamic loads (Taillandier & Farcy (2022)). Very large historical Zeppelins and several proposed hybrid cargo concepts fall into the rigid or hybrid categories, combining composite envelopes and extensive internal frameworks to withstand environmental loads while achieving high payload capacity and improved aerodynamic performance (Lobner (2024b); Hasan (2021)). In all cases, the structural architecture and envelope must be designed together, since the hull both carries loads and provides the buoyant volume (Liao & Pasternak (2009); Stockbridge *et al.* (2012)).

By contrast, most indoor airships are classified as *non-rigid* because the limited buoyant volume can hardly compensate for the mass penalty of internal frames or keels Bhat *et al.* (2024b). The envelope must therefore maintain geometric stability while accommodating local wrinkling or deformation during minor contact events. To satisfy these constraints, indoor hulls almost exclusively employ single-layer ultralight polymer films designed to provide adequate gas retention and flexibility at minimal mass Bhat *et al.* (2024b).

Typical materials include single-layer thermoplastic polyurethane (TPU or PU) and biaxially oriented polyethylene terephthalate (BoPET), commercially known as Mylar. Mylar is a polyester film produced by stretching polyethylene terephthalate in two perpendicular directions, creating a stable, low-permeability material with good tensile strength and dimensional stability. In indoor applications, Mylar is frequently used in combination with a metalized layer to reduce helium diffusion, although its brittleness and susceptibility to creasing make it less suitable for

repeated folding or collision-tolerant designs. PU films, by contrast, offer greater elasticity, puncture resistance, and ease of welding, at the expense of somewhat higher gas permeability.

Because indoor LTA vehicles operate at small volumes, typically on the order of one cubic meter, their envelopes are extremely thin, usually ranging from 10 µm to 150 µm depending on application scale Bhat *et al.* (2024b). Internal pressurization is maintained at very low differential pressures (below 0.5 kPa), sufficient to preserve hull shape while avoiding excessive envelope stress. At these dimensions, the envelope itself serves simultaneously as the aerodynamic surface, load-bearing structure, and gas barrier, eliminating the need for internal frameworks to achieve near-neutral buoyancy.

Table 1.1 summarizes the reported trade-offs of the two envelope families most commonly used in compact indoor LTAs. The comparison highlights that none of these materials satisfies the tight mass budget, tear tolerance, sealability, and helium retention required altogether for long-duration indoor operation. These limitations motivate the material strategy evaluated in the remainder of this work and directly motivate the experimental and numerical bladderevaluation framework developed in Chapter 3.

Table 1.1 Literature-based comparison of commonly used indoor airship envelope membranes. Each entry summarizes reported advantages and limitations relative to key requirements for ultra-light indoor LTA platforms.

Performance criterion	**TPU / PU films**	**BoPET (Mylar), often metalized**
Areal mass efficiency (thickness/weight contribution)	Moderate areal mass; practical indoor envelopes often use thicker grades to ensure durability, which reduces payload margin.	Very low mass achievable with thin films (10–25 µm)
Load-bearing capability under internal pressure	Moderate tensile capacity with high compliance; sustained loading can promote creep and gradual dimensional changes.	High tensile strength and stiffness for a given thickness; low strain-to-failure increases sensitivity to stress concentrations.
Elastic deformation and shape accommodation	Highly elastic; tolerates folding, wrinkling, and low-speed contact without permanent set, at the expense of reduced geometric stiffness.	Limited elastic strain; repeated bending leads to crease formation and permanent set, which localizes stresses.
Resistance to tear and puncture	Good tear and puncture resistance with predominantly ductile failure; performance remains thickness- and grade-dependent.	High initial puncture force due to stiffness; once a defect forms, tear propagation can be rapid, especially in thin gauges.
Behavior under pressurization (burst/overpressure tolerance)	Progressive, ductile response under overpressure; failure is preceded by large deformation and local thinning that may leak.	Higher burst pressures can be reported, but failure tends to be abrupt and localized (brittle), particularly near seams or folds.
Helium retention (permeability/leakage)	Moderate permeability; acceptable for short missions but requires periodic refilling for long-duration operation.	Low permeability, particularly for metalized films; barrier performance can decline when folding damage or defects are present.
Impact and contact tolerance	Typically robust under low-speed indoor contact, abrasion, and scratches remain potential sources of leak initiation.	Lower tolerance to repeated contact and folding; accumulated small defects and creases significantly shorten service life.
Joining and seam integrity	Thermally weldable with a relatively wide processing window; overheating can thin the film locally and introduce micro-defects.	Commonly joined with adhesives or tapes due to limited weldability; seam quality often dominates leakage risk.
Summary for indoor LTA use	Practical baseline for prototyping and collision-tolerant operation, with trade-offs in mass efficiency and gas retention.	Attractive when low leakage is prioritized, but limited by brittleness, folding fatigue, and more demanding manufacturing.

1.4 Envelope joining methods and seam behavior

As part of the selection of the base membrane, the joining technique available to assemble envelope panels is a primary determinant of airship reliability, since seams introduce geometric discontinuities, local stiffness changes, and potential leakage paths. For large aerostats and high-altitude airships, envelope materials are frequently laminated textile composites that incorporate a thermoplastic sealing layer, enabling panel assembly via hot-bar or hot-air welding with lap or butt seam geometries aligned with principal load paths Li, Vallabh, Bradford, Kim & Seyam (2022b). Reported parametric investigations indicate that welding parameters (temperature, pressure, dwell time) strongly influence joint peel strength, tear resistance, and gas-tightness, and that damage often initiates within or adjacent to the heat-affected zone rather than in the undisturbed laminate Li *et al.* (2022b); Lv *et al.* (2022). Mechanical characterization of welded joints further suggests that seam strength and seam stiffness can govern global structural response, with failure modes that are frequently localized and sensitive to process-induced heterogeneity Shi *et al.* (2018).

At smaller scales, particularly for indoor LTA platforms employing ultra-thin and most often single-layer polymer films, these seam-related effects become more severe because the seam mass is more significant with respect to the overall hull mass, and local thermal distortion can dominate envelope behavior. Consequently, alternative joining approaches have been investigated to reduce seam width and additional mass while improving control over the final envelope geometry (minimizing weld-induced shrinkage, wrinkling, and shape distortion) and hermeticity (gas-tightness), including ultrasonic welding, laser transmission welding, and adhesive or hot-melt film lamination Lv *et al.* (2022). These techniques can produce narrow, repeatable seams with reduced heat-affected zones, but they also introduce sensitivities to material compatibility, surface condition, pressure uniformity, and long-term durability of the weld or adhesive interface (e.g., aging, fatigue, and environmental exposure) Lv *et al.* (2022); Shi *et al.* (2018). Overall, the literature consistently identifies seam design and process selection as limiting factors for long-term mechanical robustness and gas retention in envelope structures, motivating systematic assessment of joining strategies for ultra-light indoor membranes.

1.5 Indoor airships versus multicopters

Over the last decade, multicopters have seen increased commercial and paramilitary applications in indoor settings. Indoor airships may present themselves as better suited for some of these applications. While both vehicle types can be employed for confined navigation and inspection, they rely on fundamentally different flight principles. Multicopters generate lift exclusively via powered rotors and require continuous thrust to remain aloft, resulting in high energy consumption, limited endurance, and pronounced downward airflow. Indoor airships, by contrast, achieve lift passively through buoyancy and only require propulsion for translation and attitude stabilization. This enables extended flight duration, low power usage, and minimal disturbance to the surrounding air, which is particularly advantageous for inspection, mapping, and operation in delicate or cluttered environments.

The distinct flight principles of these platforms yield specific operational advantages, summarized in Table 1.2. Quadcopters excel in rapid, accurate maneuvering but pose safety risks in delicate or occupied environments due to high rotor speeds and strong downdrafts. Indoor airships, with their gentle, soft-bodied motion, are better suited for tasks that demand low disturbance, such as infrastructure inspection in proximity to fragile artifacts or sensitive equipment.

Across comparable size classes, airships typically achieve higher payload ratios than multicopters because buoyancy offsets a substantial portion of the vehicle's weight, whereas quadcopters must continuously support their full mass via rotor thrust (for reference, helium provides approximately 1 kg of net lift per cubic meter at standard temperature and pressure, or about 1 g per liter). However, at small indoor scales, the available gas volume is inherently limited; to preserve positive buoyancy, the entire flight system, envelope, propulsion, batteries, avionics, and payload must remain extremely lightweight to satisfy this strict mass budget. Mission selection thus hinges on operational needs: multicopters offer superior maneuverability in small, open workspaces, while airships are preferred for long-duration, low-disturbance monitoring in sensitive or cluttered areas. Ongoing research seeks to refine indoor LTA vehicles to

maximize endurance, payload efficiency, and autonomous control in spatially constrained environments Mazzei *et al.* (2023b); Huang *et al.* (2019b); Gordoniz, Saad & St-Onge (2025).

1.6 Indoor LTA Vehicle Design Challenges

From the previous sections, we acknowledge that indoor LTA vehicles present a unique set of scientific and engineering challenges that differ fundamentally from those encountered in outdoor airships. These challenges arise from the interplay of physical constraints imposed by confined environments, the scaling effects associated with small buoyant volumes, and the manufacturing limitations of ultra-thin polymer membranes. We regroup these challenges into three main topics.

A. A primary difficulty in indoor airship design is the tight coupling between geometry, mass, and buoyancy. The dimensions of the operating space strictly limit the available gas volume; thus, designers must achieve near-neutral buoyancy with minimal structural mass while preserving sufficient mechanical strength and gas retention. As vehicle size decreases, scaling effects become critical: the buoyant force, which depends on volume, diminishes more rapidly than the weight of the structure and onboard components, which scale with surface area. This leaves little margin for excess mass or material imperfections. Even small variations in film thickness, seam stress concentration, or localized wrinkling can shift the buoyancy equilibrium and compromise flight stability Catar *et al.* (2024). Maintaining positive buoyancy, therefore, demands highly controlled envelope fabrication and precise weight balancing throughout the vehicle and the total weight of the airship membrane. While much LTA research has concentrated on autonomy and system integration, comparatively little attention has been devoted to the material properties that govern long-term envelope performance. As outlined in Section 1.3, envelope performance is commonly characterized in terms of surface density, mechanical resilience (tensile, tear, and puncture resistance), gas-barrier behavior, and manufacturability, including weldability and seam quality. In the literature, these criteria are used to compare candidate films and laminates; a quantitative assessment of common indoor airship membranes against them is presented in Chapter 3.

Single-layer films are lightweight but rarely satisfy all requirements simultaneously. Unlike outdoor envelopes, which employ multi-layer laminates for environmental resistance, indoor airship envelopes typically use single-layer films such as biaxially oriented polyethylene terephthalate (Mylar, BoPET) or polyurethane (PU) to maximize mass efficiency Bhat *et al.* (2024b). Though these materials offer favorable strength-to-weight ratios and high flexibility, they are prone to time-dependent creep, seam failure, and elevated helium diffusion rates. Film degradation—including micro-cracking, delamination, and coating wear—further increases leakage and often limits mission duration and envelope reusability to only a few operational cycles.

B. Manufacturing constraints further complicate the use of ultra-thin polymer films (below 50 μm) in indoor airships. These membranes are inherently challenging to handle and join, as welding or sealing often causes local thermal distortion, stiffness, or heterogeneous mechanical properties that concentrate stresses and may result in leakage or rupture. Traditional heat-sealing—standard for outdoor airship envelopes—produces thick seams and variable reliability in thinner indoor films. To address this, advanced fabrication techniques such as laser welding, ultrasonic sealing, and adhesive bonding with controlled curing are increasingly adopted to achieve uniform seam geometry and reduce excess mass Adorno-Rodríguez (2014); Rozhok (2023). Process repeatability also presents a significant challenge: minor fluctuations in temperature, film tension, or alignment during assembly can induce measurable geometric deviations, affecting hull symmetry, aerodynamic performance, and pressure retention. Additionally, imperfect seam bonding can enhance local permeability and accelerate fatigue, ultimately limiting the operational lifespan and consistency of membrane-based indoor airship systems (Shi *et al.* (2018); Wang *et al.* (2017); Yang *et al.* (2019).

C. Finally, system-level integration poses practical constraints in indoor LTA manufacturing. Because every additional gram directly reduces net lift, the selection and placement of components such as batteries, sensors, propulsion units, and electronic modules must be optimized not only for mass but also for accessibility, stability, and maintainability. Power supply remains a critical limitation: small lithium-polymer batteries often account

for 10–15% of the total vehicle mass, constraining endurance despite the inherently low propulsive energy demand of buoyant flight. Research into lightweight tethered power delivery and emerging micro–fuel cell technologies shows promise for extending operational autonomy in confined environments Ryan (2017).

Beyond physical integration, a major unresolved challenge lies in the absence of realistic simulation frameworks capable of assessing the coupled effects of envelope deformation, lightweight structural reinforcement, and payload placement in indoor LTA vehicles. At the small scales and low stiffness levels characteristic of indoor platforms, envelope mechanics, local reinforcement, mass distribution, and vehicle dynamics are strongly interdependent. However, these effects are typically evaluated separately using simplified models, which limits the ability to predict system-level behavior during the design phase. As a result, decisions related to gondola layout, component distribution, and reinforcement strategies often rely on iterative prototyping rather than validated predictive simulations. This limitation complicates early-stage trade-off analysis between structural robustness, stability, and endurance, and represents a key challenge for the systematic design of ultra-light indoor LTA systems.

The principal challenge, and the motivation for this thesis, is enabling thin, lightweight envelopes to withstand the mechanical stresses and collisions characteristic of cluttered indoor spaces. To address this, the present research proposes integrating a protective, ultra-light skeletal framework over a novel ultralight and robust envelope—an innovation inspired by load-distribution strategies used in large-scale and extraterrestrial airship designs (Zhao, Chen & Chen (2022); Gao *et al.* (2023); Feinerman, Sabatino, Ma, Lynch & Tavana (2022)), but here adapted and validated for indoor LTA vehicles.

1.7 Structure of the dissertation

The structure of this dissertation follows a logical progression from the contextual background and prior research, through the stated objectives and methodological development, to experimental

and numerical validation, and concludes with a synthesis of the findings and future directions. The chapters are organized as follows:

The introduction established the research context and motivation, introduced LTA systems for confined environments, and formulated the guiding research questions.

The current Chapter 1 presented a review of relevant literature with a deliberate emphasis on bladder(envelope) materials for compact indoor LTA systems. It first introduced outdoor airship design to establish the broader technological context, including historical development, structural classes, and the distinction between outdoor and indoor operating environments. The chapter then concentrates on bladder materials and joining methods for indoor airships, examining their mechanical, barrier, and manufacturing constraints at small scales. This progression culminates in an analytical summary that identifies the specific gaps in indoor bladder performance and seam behavior that motivate the research carried out in this thesis.

Chapter 2 details the research objectives and methodological framework. Two main thrusts are articulated: (i) the design and characterization of an ultralight bladder with enhanced leakage resistance; and (ii) the development of finite-element simulations for evaluating pressurization and impact scenarios in SLTA structures.

Chapter 3 documents the results of material development for the proposed indoor airship (*VELUM – Vehicle Envelope with Lightweight Ultrafilm for Minimal Leakage*), including material selection, coating strategies, fabrication processes, mechanical testing, and permeation characterization. The selected envelope solution is presented alongside its suitability for prototyping and field deployment. This chapter was submitted for journal publication.

Chapter 4 describes explicit dynamic finite-element analyses comparing non-rigid and semi-rigid SLTA. Model generation, element technology, boundary conditions, and mass-scaling procedures are detailed. Analytical results for pressurization and impact scenarios assess deformation, stress distributions, and the damage mitigation afforded by semi-rigidized structures.

The Conclusion synthesizes the principal findings and contributions, discusses limitations, and proposes directions for future research, with emphasis on localization, actuation, and autonomy for indoor SLTA platforms. Appendices contain supplementary material, and the Bibliography provides a complete list of referenced works.

Table 1.2 Comparison overview of an indoor LTA airship and a multicopter.

Criterion	Indoor LTA vehicle	Multicopter
Carbon Footprint	• Operates with minimal energy due to buoyant lift (Mitra *et al.* (2024)) • Finite helium supply (Dai *et al.* (2021)) • Reduced material and energy footprint	• Continuous rotor power demand (Dai, Zhang & Low (2024); Riboldi & Rolando (2023)) • Carbon-intensive materials (e.g. carbon fiber, batteries)
Impact Resistance	• Structure protects the bladder(envelope) • Low-speed collisions minimize damage (Burri *et al.* (2013); Troub, DePineuil & Montalvo (2017))	• Rigid or Semi-rigid frame withstands bumps • Propellers & electronics prone to damage on impact (May & Strohbach (2025); Troub *et al.* (2017))
Maneuverability	• Slow, stable flight (Riboldi & Rolando (2023); Troub *et al.* (2017)) • Limited sharp turns, gentle transitions	• Highly agile (Troub *et al.* (2017)) • Quick directional changes, precise control (Riboldi & Rolando (2023))
Sustainability	• Durable polyurethane bladder(envelope) • Helium reuse and careful management • Fewer electronics to discard	• Batteries & electronics produce e-waste (Kordos *et al.* (2024)) • Frame materials can have high embodied energy
Nuisance	• Very quiet, gentle motion (Bhat *et al.* (2024a)) • Large bladder(envelope) may be visually prominent but not disruptive	• Noticeable rotor noise • Fast maneuvers can be intrusive indoors
Energy Consumption & Flight Duration	• Extremely low power to remain aloft • Multi-hour flights possible (Bhat *et al.* (2024a))	• High power draw to maintain lift • Typically 5–20 min per battery (Palossi *et al.* (2019))
Safety for Humans	• Soft bladder(envelope), low speed (Troub *et al.* (2017)) • Inert helium; minimal injury risk	• Rotor blades can cause cuts • Higher-speed impacts, rare battery fire risk

CHAPTER 2

OBJECTIVE AND METHODOLOGY

The present research aims to design, fabricate, and validate ultra-light indoor SLTA systems capable of safe and efficient operation in confined or subterranean environments. The work is structured around two main objectives: (Objective 1) to develop and validate an ultra-light bladder(envelope) system for indoor LTA vehicles, based on a coated polymer envelope and an auxiliary lightweight structural framework, designed to improve gas retention, mechanical robustness, and damage tolerance without exceeding strict mass constraints; and (Objective 2) to establish a simulation framework to evaluate the pressurization and impact behavior of SLTA bladder(envelope) and to mitigate thin-bladder damage during flight in cluttered environments with multiple obstacles by employing a semi-rigid system configuration.

2.1 Objective 1: Development of an ultralight coated envelope for indoor airship envelopes

The first objective focused on the conception and experimental validation of an innovative airship envelope material that combines high flexibility, low surface density, and enhanced helium retention. Commercially available polymer films, such as PU and biaxially oriented polyethylene terephthalate (Mylar, BoPET), were found unsuitable for indoor operation due to excessive stiffness, relatively high mass, and insufficient gas-barrier performance. To address these limitations, an extensive screening of candidate materials was conducted, leading to the selection and modification of a low-density polyethylene (LDPE) film with a tailored sol–gel coating to enhance both barrier and mechanical properties. The resulting membrane, developed under the project name *VELUM – Vehicle Envelope with Lightweight Ultrafilm for Minimal Leakage*, preserves the foldability and elasticity of polyethylene while significantly improving helium retention and surface durability. This innovation led to a patent application filed by École de technologie supérieure (ÉTS)[1].

[1] This work is the subject of an international patent application (PCT/CA2025/050918), entitled "Aerostat envelope, aerostat comprising same, and method of manufacturing same," filed July 2, 2025, by École de technologie supérieure. Inventors: A. Kheirani, D. St-Onge, I. Tabiai, and N. Tepylo

2.1.1 Experimental Tools

Experimental work encompassed film coating, mechanical testing (tensile, tear, puncture, and burst), and leakage characterization, using specialized facilities and instrumentation at ÉTS, UQAM, and Polytechnique Montréal, in addition to the laboratories detailed in Appendix I. The results validated the membrane's suitability for confined-environment airship applications and provided essential input parameters for the finite-element simulations described in Objective 2.

2.2 Objective 2: Design of an airship simulation for impact and damage assessment to protect the thin envelope

The second objective is to develop a numerical framework for evaluating the mechanical behavior of indoor airship envelopes under internal pressurization and impact loading. Because buoyancy must be maintained with minimal envelope mass, these vehicles use fragile polymer membranes that are susceptible to large deformations, tearing, or rupture upon contact with obstacles. To address this vulnerability, the study investigates how incorporating a lightweight structural exoskeleton can enhance the envelope's robustness without significantly increasing weight. Finite element models are used to compare two configurations: a non-rigid envelope consisting solely of an inflatable bladder and a semi-rigid airship reinforced with a lightweight exoskeleton.

The first set of simulations examines deformation and stress distributions under static internal pressurization, assessing how reinforcement affects geometric stability, overall deformation, wrinkling, and load transfer within the membrane. A second series of simulations considers low-velocity impacts against rigid obstacles to evaluate the ability of the exoskeleton to reduce local strain concentrations and the likelihood of damage in the thin membrane, thereby providing a quantitative basis for assessing its influence on impact resilience and damage mitigation with direct implications for the safe operation of SLTA vehicles in environments with frequent obstacle interactions.

2.2.1 Modeling Tools

All simulations were conducted using Abaqus/CAE 2024 (Dassault Systèmes, SIMULIA), which employs explicit dynamic solvers capable of capturing large deformations and complex contact interactions. Geometry modeling, material assignment, and boundary condition definitions were performed within the Abaqus/CAE environment. At the same time, post-processing of results, including stress fields, contact response, and deformation patterns, was conducted in Abaqus/Viewer. This workflow provided quantitative insight into stress evolution, deformation control, and energy absorption mechanisms, serving as a virtual validation step before physical prototyping. The outcomes informed the design of safer and more durable semi-rigid SLTA tailored for confined, obstacle-rich indoor environments.

CHAPTER 3

VEHICLE ENVELOPE WITH LIGHTWEIGHT ULTRA-FILM FOR MINIMAL LEAKAGE (VELUM)

Afsaneh Kheirani[1] , Ilyass Tabiai[2] , David St-Onge[1]

[1] Department of Mechanical Engineering, INIT Robots Lab, École de technologie supérieure (ÉTS)
1100 Notre-Dame Ouest, Montréal, Québec, Canada H3C 1K3

[2] Department of Mechanical Engineering, LIPEC Lab, École de technologie supérieure (ÉTS),
1100 Notre-Dame Ouest, Montréal, Québec, Canada H3C 1K3

Article under review for the *Aerospace Science and Technology* Journal

3.1 Abstract

Indoor inspection and mapping missions in tunnels, industrial facilities, and subterranean environments require aerial platforms capable of long-duration operation in cluttered, humid, and navigation-denied conditions. While multirotor drones provide high maneuverability, their endurance and payload capacity are fundamentally limited by battery-powered lift. Small indoor lighter-than-air vehicles alleviate this constraint through buoyancy; however, at meter-scale volumes, envelope materials become a critical limitation, as they largely determine system mass, gas retention, durability, and resistance to handling and collisions. Commonly used films present persistent trade-offs: metallized polyester offers low gas permeability but limited mechanical robustness, whereas polyurethane is more durable but heavier and more permeable.

This work introduces and experimentally validates a lightweight composite envelope material based on low-density polyethylene combined with a fluoro-siloxane barrier coating. The proposed treatment significantly improves helium retention while preserving flexibility and resistance to handling. Mechanical and functional testing show that the coated material achieves substantially higher tear resistance than metallized polyester and improved durability compared to polyurethane, while remaining considerably lighter. A cylindrical airship fabricated from this membrane was deployed in a semi-autonomous underground mapping mission, demonstrating

reduced helium leakage, stable performance in humid conditions, and multi-day operation. These results show that fluoro-siloxane-coated polyethylene enables lightweight, durable, and gas-efficient envelopes, supporting persistent indoor operation of small lighter-than-air aerial platforms.

Keywords: Lighter-than-air (LTA) airship;Inflatable structures; Gas barrier membrane; Thin polymer film;LDPE film;sol gel Coating;Semi-rigid airship

3.2 Introduction

Mobile robots are increasingly deployed for inspection, mapping, scientific exploration, and safety-critical operations in environments where direct human intervention is hazardous or impractical Agrawal & et al. (2024); Awasthi & et al. (2023). Recent advances in sensing, autonomy, communication, and multi-robot coordination have broadened their use across industrial, civil, and scientific domains, with comprehensive surveys highlighting rapid progress in navigation, perception, swarm coordination, and task automation, particularly for indoor and infrastructure-focused applications Agrawal & et al. (2024); Awasthi & et al. (2023). As a result, aerial mobile robots are now routinely considered for missions in complex and previously inaccessible spaces Agrawal & et al. (2024).

In confined indoor environments, multirotor drones remain the dominant aerial platform due to their agility, maneuverability, and precise hovering capability Nooralishahi *et al.* (2021); Qubaa, Hamdon & Al Jawwadi (2021). They are widely employed in industrial facilities and warehouses Nooralishahi *et al.* (2021), tunnels Pahwa *et al.* (2019), and archaeological or heritage sites Qubaa *et al.* (2021); Themistocleous (2019), as well as in subterranean settings such as caves, mines, and underground infrastructures where uneven, flooded, or unstable terrain can render terrestrial robots ineffective Maity, Majumder & Ray (2013); Salas Gordoniz, Reeves & St-Onge (2021). Despite substantial advances in autonomy and control, these environments expose a fundamental limitation of multirotor systems: their reliance on continuous, battery-powered thrust to generate lift Agrawal & et al. (2024).

Recent work has primarily addressed this limitation through system- and control-level strategies, including improved navigation, energy-aware planning, swarm coordination Agrawal & et al. (2024); Escobar & Pereira (2025), and real-time mass and inertia estimation Sands (2025), in an effort to extend mission capability without modifying the underlying multirotor architecture. Although such approaches can increase the efficiency with which onboard energy is used, they do not remove the basic requirement for sustained propulsive lift. Consequently, limited flight time and restricted payload margins remain critical bottlenecks for indoor and long-duration missions, particularly in GPS-denied, humid, or geometrically constrained environments Agrawal & et al. (2024).

To overcome these constraints, Lighter-than-air (LTA) vehicles offer an alternative aerial paradigm by exploiting buoyant lift to sustain flight with minimal energy expenditure. By decoupling lift generation from continuous power consumption, LTA platforms directly address the endurance limitations inherent to multirotor systems. Their low noise, reduced vibration, and low-impact dynamics make them particularly well suited for sensitive or confined environments, while their inflatable structure enables lightweight construction, mechanical robustness, and compact storage Mandlekar, Joshi & Butola (2022); Liao & Pasternak (2009).

Although lighter-than-air vehicles have traditionally been used for entertainment and advertising, several research prototypes have demonstrated their feasibility for scientific and robotic applications Mulay & Pant (2013); Biju & Pant (2017); Adeel, Shoeb and Suvarna, Sohan (2017); Gorjup & Liarokapis (2020), including operation in underground or tunnel-like environments Faye (2015); St-Onge, Reeves, Gosselin & et al. (2017). These efforts confirmed the potential of small-scale LTA platforms for persistent aerial operation, while also revealing significant technical challenges. Multiple avenues have been explored to address these limitations, including refinements in vehicle geometry, control strategies, hybrid buoyant–propulsive configurations, and adaptive or compliant structures. However, at the indoor scale of roughly one cubic meter –compatible with doorways and confined passages– the envelope material remains a first-order system constraint. The limited lifting-gas volume leaves very narrow mass margins once essential onboard components such as actuators, sensors, and processing units are accounted

for Maity *et al.* (2013). As a result, the envelope often dominates the mass budget, in some designs accounting for more than 30% of the available lift Adeel, Shoeb and Suvarna, Sohan (2017); St-Onge *et al.* (2017). These material-level constraints bound achievable performance regardless of higher-level control or structural strategies, making envelope materials a critical and comparatively underexplored design dimension for persistent indoor LTA operation.

Existing materials such as Mylar and polyurethane (PU) involve fundamental compromises: the former offers low permeability but suffers from brittleness, while the latter provides flexibility at the expense of weight and gas retention. These persistent trade-offs indicate that neither material provides a fully balanced combination of mechanical robustness, mass efficiency, and gas retention for repeated field deployment in confined environments, motivating the exploration of alternative envelope materials.

Low-density polyethylene (LDPE) has recently emerged as a promising candidate in this context due to its favorable mechanical behavior and low areal density; however, its relatively high gas permeability remains a limiting factor for long-duration missions.

Accordingly, the objective of this work is to develop and experimentally validate a lightweight envelope material that reconciles mechanical robustness, mass efficiency, and gas retention for small indoor LTA vehicles. To this end, the study (i) quantitatively characterizes the mechanical and functional limitations of commonly used PU and Mylar membranes, (ii) evaluates LDPE as a mechanically advantageous alternative, (iii) addresses its remaining permeability limitation through a lightweight surface treatment, and (iv) validates the resulting material through laboratory testing and full-scale field deployment in a confined underground environment.

The remainder of the paper is structured as follows. Section 3.3 defines the performance requirements for indoor airship membranes, section 3.4 describes the materials and experimental methods, section 3.5 details the fabrication of laboratory and full-scale envelopes, section 3.6 presents the experimental results, and section 3.7 reports on field deployment.

3.3 Background: Membrane performance

While most LTA research has focused on autonomy and platform-level integration, less attention has been given to the envelope materials that determine sustained indoor operation. The following criteria provide a framework for evaluating candidate materials, capturing requirements that must be simultaneously satisfied for the efficient operation of both large- and small-scale LTA systems Li *et al.* (2022a); Dhawan & Jindal (2021):

- **High specific strength:**[1]The material should be lightweight to maximize payload while providing tensile strength under biaxial stress to resist pressurization loads, attachment forces, and handling stresses. Adequate strength reduces creep, permanent deformation, and rupture, preserving envelope stability during long-term operation.
- **Tear resistance:** Resistance to tear initiation and propagation is critical, as small cuts or stress concentrators may develop under bending, snagging, or folding Maekawa *et al.* (2008); Bai, Xiong & Cheng (2011). Whether defects remain stable depends on their size, material toughness, and in-service stresses (e.g., internal pressure, biaxial tension, environmental effects). In large outdoor airships, sub-critical slits may only cause slow leaks, allowing mooring Prentice & Ahmed (2017) and repair, whereas for small indoor vehicles, even minor leaks can terminate a mission. Complementary burst tests reveal thresholds beyond which cracks propagate rapidly under biaxial loading. Failure mode depends on toughness: brittle films fragment into multiple tears, while tougher films fail as a localized slit. Thus, adequate tear resistance is required both to prevent gradual lift loss and to avoid catastrophic rupture.
- **Puncture resistance:** The material must withstand concentrated forces without penetration, protecting against sharp objects during handling and in-flight collisions, a common risk indoors.
- **High gas barrier properties:** Low helium permeability is essential for maintaining flight duration and reducing operational costs. Helium permeability, expressed in $cm^3 \cdot mm/m^2 \cdot day \cdot atm$, quantifies the diffusion of helium through a standardized membrane

[1] Often defined in mechanics as *specific tensile strength* (strength divided by density). In aerospace and LTA literature, the equivalent concept is more commonly referred to as "strength-to-weight ratio" Li *et al.* (2022a); Dhawan & Jindal (2021).

area and thickness over 24 hours at one atmosphere. Lower values indicate stronger barrier performance. While most untreated polymer films exhibit relatively high helium permeability compared to advanced barrier materials, surface modifications and nanocomposite coatings can significantly reduce gas transmission by extending diffusion pathways and lowering free volume Nguyen-Tri, Nguyen, Carriere & Ngo Xuan (2018); Majeed, Arjmandi & Hassan (2018); Zhai & Euler (2005b); Vallabh *et al.* (2022).

- **Wettability and moisture resistance:** Wettability, which determines a material's hydrophobic or hydrophilic behavior, depends on chemical composition and surface morphology; rough, low-energy surfaces promote water repellency. The degree of wettability is commonly quantified by the *static water contact angle* (CA), defined as the angle between the tangent to a liquid droplet at the solid–liquid–vapor interface and the solid surface. Hydrophilic surfaces exhibit CA values below 90°, whereas hydrophobic surfaces show CA values greater than 90°. Superhydrophobicity requires CA values above 150° Zhang, Xia, Kim & Sun (2012). These surface properties mitigate moisture uptake Huang *et al.* (2019a), which would otherwise increase mass and compromise the mechanical consistency, thereby reducing the endurance and reliability of the envelope material.
- **Welding test:** Welding of polymers through the application of heat enables lightweight, strong joints without adhesives or mechanical fasteners, minimizing both weight and fabrication complexity. Thermal bonding is also necessary for unconventional envelope geometry, as heat welding allows continuous, airtight seams along complex curvatures. Industrial envelopes are generally limited to standard shapes and sizes, and custom manufacturing is often unavailable or prohibitively expensive.
- **Cost-effectiveness and maintenance:** Economically viable materials that can be repaired easily are essential for extending service life and reducing maintenance.

Among these factors, high specific strength and gas barrier properties are the most critical for indoor use due to the tight size and payload constraints. Single-layer films are lightweight but rarely satisfy all requirements simultaneously. Consequently, two complementary strategies are widely used Mandlekar *et al.* (2022); Chouhan, Ghosh, Butola & Joshi (2024); Li *et al.* (2022a);

Dhawan & Jindal (2021): *lamination*, which integrates gas-barrier layers between structural plies to extend diffusion paths and improve tear resistance; and *surface coating*, which fills micro-voids and reduces free volume to suppress helium transport.

Recent outdoor-focused research has advanced multi-layer laminates and high-performance fibers. Li et al. Li *et al.* (2022a) achieved permeability below 0.1 $cm^3 \cdot mm/m^2 \cdot day \cdot atm$ using Zylon® and Vectran® textiles with aluminum coatings, combining excellent barrier and UV resistance. Chouhan et al. Chouhan *et al.* (2024) and Joshi et al. Zhai & Euler (2005b) developed coated laminates with high durability, but such systems require complex fabrication and add weight, making them unsuitable for small-scale indoor LTA applications. Dhawan and Jindal Dhawan & Jindal (2021) improved PU laminates with fabric reinforcement, though at the cost of higher surface density. PU nanocomposites with graphene or layered silicates Joshi *et al.* (2018) reduce gas diffusion but demand precise dispersion control, increasing cost.

Other barrier polymers, including Mylar®, EVOH, and PVDC, have very good gas retention but poor low-temperature flexibility and sealability, and they can crack under repeated loading Joshi *et al.* (2018); Zhai & Euler (2005b). EVOH-based laminates, for example, can reach permeabilities as low as 0.04–0.8 cm^3 mm/m^2 day atm and surface densities of about 103–113 g/m^2 Vallabh *et al.* (2022), but they are optimized for outdoor conditions and are unnecessarily complex for indoor use.

In practice, compact indoor LTAs rely mostly on commercially available PU and Mylar® films Bansal *et al.* (2013); Motiwala, Khan, Yelve, Narkhede & Pant (2013).
Both materials present clear drawbacks. Mylar provides low permeability but is brittle and prone to failure under repeated folding, often requiring additional protective layers that offset weight savings Verheul, Breukels & Ockels (2009). PU offers flexibility and durability but suffers from high helium permeability due to its copolymer microstructure; heavier grades improve retention but at the expense of mass Joshi *et al.* (2018).

While helium is the primary lift gas, O_2 (atomic radius 0.35 nm) and CO_2(atomic radius 0.33 nm) permeabilities are commonly measured as proxies, since diffusion follows the

solution–diffusion model, where both molecular size and gas solubility in the polymer govern transport Dhawan & Jindal (2021); Joshi *et al.* (2018); Mandlekar *et al.* (2022). Table 3.1 summarizes reported permeabilities of common LTA films and advanced barrier materials. PU exhibits the highest helium permeability, whereas Mylar achieves substantially lower values. EVOH and PVDC demonstrate the strongest barrier performance across all gases Joshi *et al.* (2018); however, their use in indoor LTA systems is limited by moisture sensitivity, thermal instability, and poor weldability Blanchard, Gouanvé & Espuche (2017); Collins *et al.* (1999). Along with the higher basis weights required for durability, these drawbacks limit their practicality in lightweight indoor envelopes.

Given these limitations, this study investigated low-density polyethylene (LDPE) as a lightweight, tear-resistant alternative for indoor airship envelopes. LDPE is flexible, impact-resistant, and lighter than PU, while offering better tear resistance than Mylar®. However, its amorphous structure contains free-volume voids that allow helium diffusion (atomic radius 0.26 nm) Safandowska, Makarewicz & Rozanski (2024); Mandlekar *et al.* (2022). Despite this, LDPE exhibits lower O_2 and CO_2 permeability than PU Joshi *et al.* (2018), suggesting potential for improved helium retention. To address its intrinsic helium permeability, lightweight surface coatings and nanostructured fillers were investigated to reduce free volume and introduce tortuous diffusion pathways Nguyen-Tri *et al.* (2018); Song *et al.* (2018).

Table 3.1 Gas permeability of different polymeric and elastomeric film materials used for LTA envelope applications at standard testing conditions. Taken from Joshi *et al.* (2018); Shamini & Yusoh (2014).

Polymer/Elastomer	**O_2**	**CO_2**	**He**
PU	3–1067	175–2014	36–2340
BoPET (Mylar®)	1–2.4	5.9–8.9	71
EVOH	0.01–0.05	0.03–0.08	4–14
PVDC	0.03–0.04	0.47–3.2	–
LDPE	69–274	394–959	–

3.4 Materials and Methods

Potential candidate polymers for indoor LTA envelopes were studied through a series of mechanical and functional tests. The selected tests provided a comprehensive evaluation of membrane performance under conditions relevant to indoor LTA operation. Mechanical tests (tear, puncture, tensile, and burst) captured structural integrity and failure modes under localized and distributed loads, while functional tests (gas barrier, hydrophobicity, and thermal bonding) addressed envelope durability, lift retention, and manufacturability. Together, these methods established a consistent basis for comparing LDPE against conventional PU and Mylar membranes and for identifying trade-offs between mass efficiency, mechanical robustness, and gas retention.

LDPE is a widely used thermoplastic distinguished by its toughness, chemical resistance, and ease of processing. Within the polyethylene family, its highly branched molecular structure and broad weight distribution provide greater softness and flexibility than linear low-density polyethylene (LLDPE) and high-density polyethylene (HDPE) Xu, Wen & Xu (2023); Cheng (2024). These characteristics make LDPE particularly suitable for lightweight films requiring sealability and ease of fabrication. A commercial-grade LDPE was sourced Seifali Abbas-Abadi, Nekoomanesh Haghighi & Yeganeh (2012) and characterized with a Melt Flow Index (MFI) of 2.66 ± 0.12 g/10 min, measured according to ASTM D1238, Method A International (2023) (six samples, KAYJAY/2006/AC, 230 °C, 2.16 kg load).

3.4.1 Density and Thickness Measurements

Envelope mass is a critical design parameter; therefore, most results were reported relative to material density. Density was measured using a helium pycnometer (Micromeritics/Folio Instruments, AccuPyc 1340) with ten repetitions per sample. Helium was selected for its small atomic radius, which enables penetration into micro-voids and the accurate determination of true film volume. Film thickness was measured with a digital micrometer (0.001 mm resolution) at five distinct locations to capture potential heterogeneity.

3.4.2 Tear Test

Tear resistance was measured according to ASTM D1004 International (2021a) on an MTS Alliance RF/200 machine. Double-notch specimens were prepared using a Kongsberg X24 Edge cutting system (geometry shown in Fig.3.1). Tests were conducted in Mode III (anti-plane shear) Andreasson, Mehmood & Kao-Walter (2013), replicating tear initiation in envelopes subjected to snagging, bending, or uneven inflation. One grip remained fixed while the other displaced at 51 mm/min (2 in/min). A 100 N load cell (electrical sensitivity: 1.95 mV/V; resolution:0.01 N) recorded force–displacement curves for quantitative assessment. For statistical reliability, four specimens were tested for each material. LDPE films may exhibit direction-dependent tearing behavior due to processing-induced molecular orientation. During preliminary calibration trials, qualitative differences in tear propagation were observed when specimens were aligned along different in-plane directions. However, specimen orientation was not systematically controlled in the present test campaign. Accordingly, the reported tear results are provided without directional separation.

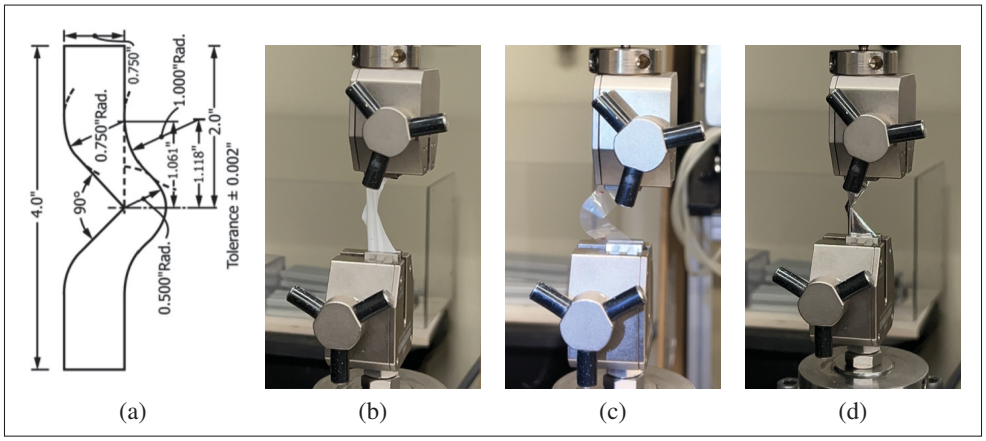

Figure 3.1 Tear test methodology: (a) Double-notch specimen geometry prepared in compliance with ASTM D1004 standards. Experimental setup for evaluating tear resistance in (b) PU film, (c) LDPE film, and (d) Mylar film.

3.4.3 Puncture Test

Puncture resistance was evaluated according to ASTM F1306 International (2021b) using the same MTS system. A hemispherical 3.2 mm plunger was driven at 25 mm/min into specimens (51 ×76 mm) clamped over a 34.9 mm hole. Four replicates were tested per material. A 100 N load cell (electrical sensitivity: 1.95 mV/V; resolution:0.01 N)recorded force-displacement curves for quantitative assessment. For statistical reliability, four specimens were tested for each material.

3.4.4 Tensile Strength of Sealed Joints

Sealed-joint tensile strength was assessed using two predefined joint configurations for LDPE, denoted as T1 (superimposed joint) and T2 (flap joint), while PU and Mylar were tested only in the T1 configuration (Fig. 3.2). Loop samples, 50 mm wide, were sealed on both edges following ASTM F88/F88M-21 International (2021c). Testing was performed on the same MTS RF/200 machine with cylindrical grips to minimize stress concentrations, using a 1000 N load cell (electrical sensitivity: 2 mV/V; resolution: 0.0005 N) and a crosshead speed of 200 mm/min. Maximum load and displacement at failure were recorded for four repeated tests(Fig. 3.3).

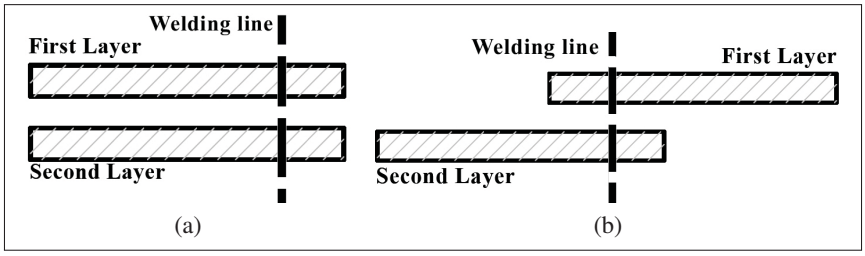

Figure 3.2 Joint configurations used in the sealed-joint tensile tests (ASTM F88/F88M-21): (a) T1, superimposed joint configuration; (b) T2, flap joint configuration. These labels (T1 and T2) are used throughout the paper to identify the tensile test configuration. The figure presents visual representations of these two joint configurations, which are commonly used in structural applications. Understanding the differences between these joint types is essential for selecting appropriate joining methods in engineering design.

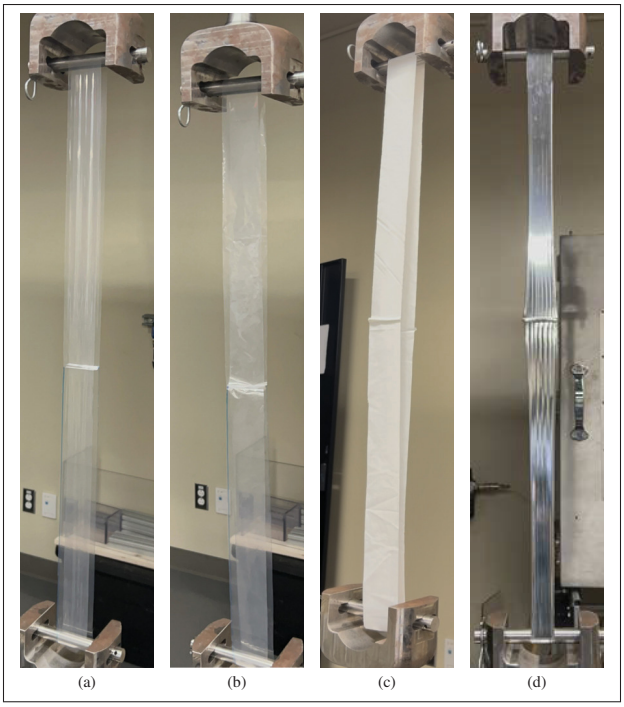

Figure 3.3 Representative tensile specimens prepared according to ASTM F88/F88M-21, showing the tested material–configuration combinations: (a) LDPE, configuration T1 (superimposed joint); (b) LDPE, configuration T2 (flap joint); (c) PU, configuration T1; (d) Mylar, configuration T1. Only LDPE was tested in both configurations (T1 and T2) to isolate the effect of joint geometry.

3.4.5 Gas Barrier Test

Gas barrier performance was evaluated through full-envelope helium retention, rather than localized permeation measurements (e.g., N500 Pant (2014)). This system-level approach captured the combined effects of polymer permeability, seam integrity, and geometry. It aligned with practices used in high-altitude balloon development, such as Loon LLC's stratospheric platforms X (2024) and Venus balloon prototypes Hall *et al.* (2009).

Custom pillow-shaped envelopes of identical dimensions were fabricated: LDPE envelopes were produced and coated in-house, while PU and Mylar envelopes were sourced commercially. Each envelope was inflated to 4 kPa with helium and suspended from a 50 N load cell (Fig. 3.4).

Internal pressure was monitored with a differential sensor (±25 kPa, Phidgets 1126_0)[2]). Lift was tracked at 1.5-minute intervals for six hours in a sealed room at 26–27 °C, with the first 10 minutes excluded to eliminate manipulation disturbances, including effects associated with manual suspension of the envelope, residual oscillations of the load-cell system, and short-term air disturbances immediately following release (Fig. 3.5). For each material, the helium retention test was repeated three times using independently fabricated envelopes. All tests were conducted in an isolated room with minimal airflow to ensure that subsequent measurements reflected steady-state helium leakage rather than external mechanical disturbances. Initial envelope weights were recorded and are reported in Tab. 3.2.

Durability was assessed by subjecting each deflated sample to 30 minutes of tumble agitation (air-fluff, no heat, two wool dryer balls), followed by reinflation and repetition of the helium retention protocol.

Table 3.2 Initial Weights of LDPE, PU, and Mylar Pillows for Gas Barrier Evaluation

Pillow Size (mm)	**Material**	**Pillow Weight (g)**
800 × 1200	Mylar	57.00
	PU	131.22
	Non-coated LDPE	124.15
	Coated LDPE	128.20

3.4.6 Wettability Properties

Wettability was assessed via static contact angle using a VCA Optima Video Contact Angle System[3]), following the sessile drop method. Samples (30 × 30 mm) were cleaned with compressed air before droplet deposition. A syringe filled with distilled water was used to dispense droplets onto the sample surfaces, and four measurements per specimen were taken across different locations. Average contact angle and standard deviation were computed.

[2] www.Phidgets.com

[3] www.astp.com

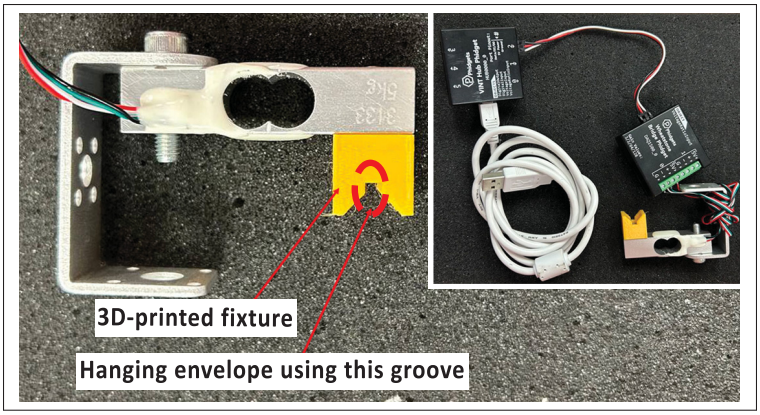

Figure 3.4 Schematic of load cell setup for helium leakage performance measurement in pillow-shaped samples. The load cell measured the lift force exerted by the pillow, which correlated with internal helium pressure and retention.

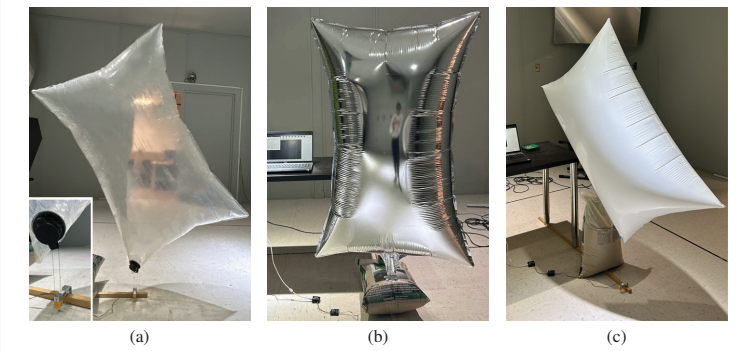

Figure 3.5 Gas barrier comparison of pillows made from (a) LDPE film, (b) Mylar film, and (c) PU film. All pillows had identical dimensions and were tested under the same conditions, inflated to the same internal pressure, and placed in a temperature-controlled, isolated room with minimal airflow or external disturbances (e.g., airflow or motion caused by nearby personnel).

3.4.7 Thermal Welding

Thermal welding trials were performed on LDPE, PU, and Mylar films using a manually actuated heat roller. Temperature was increased in 5–10 °C increments to identify welding temperature ranges that produced continuous, defect-free welds. The vertical load was estimated using a digital balance placed under the roller. After cooling, the welds were visually inspected for wrinkling, curling, or incomplete fusion to assess weld quality. The mechanical strength of

the welded joints was subsequently evaluated through dedicated tests, as described in 3.6.4. Identifying the appropriate welding temperature for each material was necessary to balance weld strength and film integrity. Excessively low temperatures resulted in incomplete fusion and weak, leak-prone joints, whereas overly high temperatures caused the membrane to thin or perforate, creating microscopic holes or thermal damage along the weld line. In this study, optimal thermal welding was defined as the temperature range that produced continuous welds without visible defects and yielded the highest joint strength in tensile testing. Determining this range ensured strong, continuous welds without compromising the structural or barrier properties of the film.

3.4.8 Validation of Burt Behavior

Burst resistance was assessed through inflation-to-failure tests, capturing biaxial stress response, tear propagation, and rupture mode Li *et al.* (2022c); Chen, Yang, Xie, Wang & Fu (2022); Li *et al.* (2024).

Pillow-shaped envelopes (800 × 1200 mm) were thermally welded and inflated with compressed air until rupture. Compressed air was used instead of helium because rupture pressure and failure behavior are governed by internal pressure and the resulting biaxial membrane stress, which are independent of the gas types at identical pressure levels. The objectives were to determine: (i) maximum internal pressure, (ii) rupture location (film vs. seal), and (iii) pressure-time behavior under biaxial loading.

Pressure was measured at 10 Hz using a differential sensor (±25 kPa range, 55 Pa resolution). Rupture events were recorded on video to document failure modes. One specimen per material ($n = 1$) was tested due to resource constraints, providing representative comparative data despite limited statistical robustness.

3.5 Fabrication of Coated LDPE Membranes

To overcome the limitations of conventional PU and Mylar films in indoor LTA applications, a custom in-house fabrication protocol was developed for coated LDPE envelopes, enabling systematic evaluation of material performance under representative operating conditions. The fabrication process was designed to maximize helium retention while maintaining gas-tightness, tear resistance, flexibility, and low mass. The sequential steps were outlined in Fig. 3.6 and are described below.

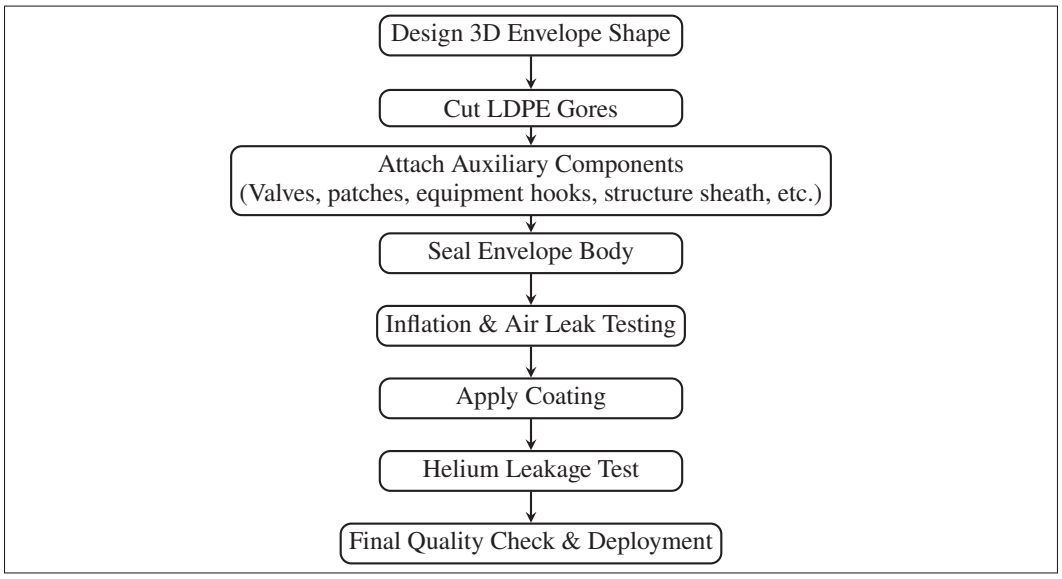

Figure 3.6 Flowchart illustrating the LDPE airship envelope fabrication process used in this study. The figure outlines the sequential steps involved, from the initial design of the envelope shape to the final quality check and deployment.

3.5.1 Gore Preparation

The number and arrangement of gores[4] were selected according to the target geometry and fabrication requirements. The gore layout balanced two competing factors: minimizing the number of welds to reduce leakage risk and ensuring geometric conformity after assembly. For symmetric or moderate-scale envelopes, two-gore configurations (e.g., pillow or cylindrical

[4] In this study, *gores* refer to the individual membrane panels thermally welded to form the main envelope body.

shapes) reduced fabrication complexity and leakage probability. Multi-gore designs provided better conformity for elongated or complex geometries but increased the number of welds, raising alignment and thermal welding demands.

Gore layouts were derived by flattening the 3D surface model of the envelope in CAD software (SolidWorks in this work). In addition to gores, *patches* were thermally welded locally to reinforce mounting points for structural components (e.g., carbon tubes), distributing concentrated loads without compromising gas-tightness. Gores were cut either manually or using a digital cutting system (Kongsberg X24 Edge in this work), the latter ensuring high precision and repeatability for prototypes.

3.5.2 LDPE Envelope Thermal Welding

Thermal welding was a critical step, particularly for complex geometries where curved weld seams or sharp transitions prevented the membrane from lying flat. Each gore was positioned over a rigid support, either flat on the table or on a fixture shaped to the envelope cross-section, ensuring alignment during thermal welding. Strong, airtight weld seams required uniform seam width, precise temperature control, and consistent pressure application.

Welding was performed using a heat roller with integrated digital temperature regulation (Fig. 3.7a). During welding, heat was supplied by the roller element, while pressure was applied manually by the operator through downward force on the roller along the weld seam. Compared to radio-frequency (RF) welding, which relies on dielectric heating Chouhan *et al.* (2024); Pant (2014); Gawale, Raina, Pant & Jahagirdar (2009), the heat-roller method enabled continuous thermal welding over long weld seams, accommodated non-uniform geometries, and was more cost-effective. During preliminary trials, the roller temperature was adjusted in discrete increments of 5–10 °C to identify a processing window that produced continuous, defect-free weld seams without film thinning or perforation. For LDPE, optimal thermal welding was achieved at a roller temperature of 170 °C.

A silicone mat was placed beneath the film to improve weld quality. Welding offsets (10 mm, corresponding to the roller tip width) were aligned and secured with tape or grippers. A silicone-coated parchment barrier prevented sticking. The applied pressure was generated by the operator through controlled manual force on the roller. The magnitude of this force was measured before welding by applying the roller onto a digital balance, corresponding to an equivalent load of approximately 300 g. During welding, the operator maintained a comparable pressure level guided by this reference. The adequacy and consistency of the applied pressure were verified indirectly through the uniformity, continuity, and repeatability of the resulting weld seams. Under these conditions, a uniform welded joint approximately 5 mm wide (corresponding to the roller tip width) was consistently produced.

Auxiliary components such as valves, sensor mounts, and structural patches (Fig. 3.7b) were pre-attached before envelope assembly. For simple two-gore designs, a sequential thermal welding approach was used. More complex geometries (e.g., cylindrical bodies with end caps Catar *et al.* (2024)) required custom fixtures to stabilize multi-gore intersections (Fig. 3.7c). Heat-resistant silicone mats were used on top surfaces to prevent deformation and protect the polycarbonate fixtures. Following assembly, each envelope was inflated and monitored for 24 h to confirm leak-free, gas-tight performance.

3.5.3 Surface Coating

After verifying air-tightness, envelopes were coated while inflated using an "under-load" technique. This approach prevented voids caused by material stretching during subsequent pressurization and ensured uniform surface coverage. Coating was applied only after all seams were welded, since applying it beforehand would have prevented the film layers from bonding during thermal welding.

Three application methods were compared:

a. *Spraying:* a high-pressure spray gun ensured broad coverage but produced discontinuous layers with droplet clustering.

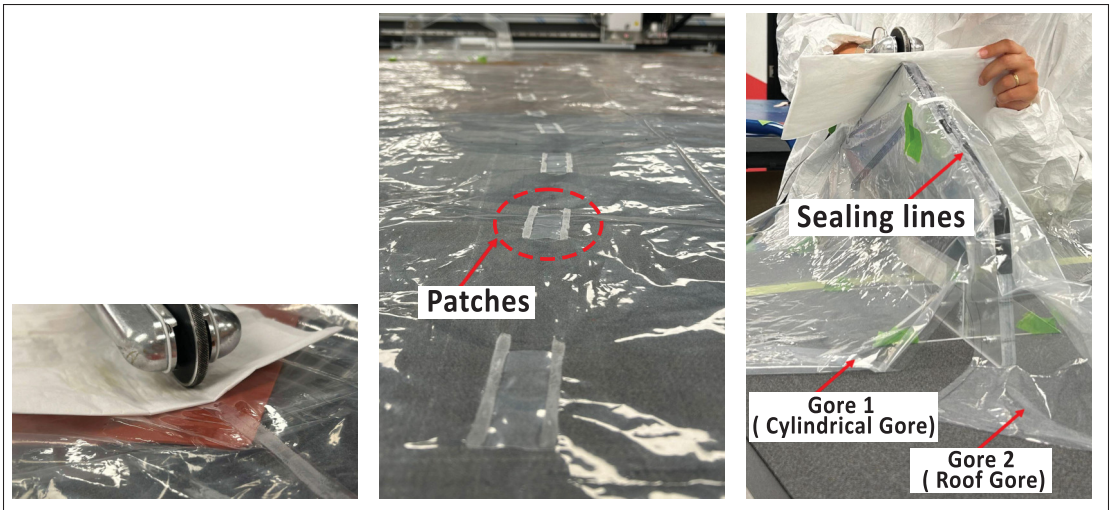

Figure 3.7 Components and setup for the envelope fabrication process: (a) Heat roller and mattress for thermal welding of gores and auxiliary components; (b) Thermally welded patches; (c) Envelope thermal welding using a custom-made fixture.

b. *Wiping:* nanofiber cloths distributed the coating manually, improving uniformity but leaving localized voids.
c. *Spray-wipe:* spraying provided initial coverage, followed by wiping to redistribute droplets into a continuous film. This hybrid method produced the smoothest, most homogeneous layer with strong adhesion.

Surface morphology was analyzed with a digital microscope (VHX-7000) on samples extracted from central, edge, and seam-adjacent zones. Non-coated LDPE (Fig.3.8a) exhibited micro-voids and irregularities acting as leakage pathways. Spray-only coatings (Fig.3.8b) showed macro-particles, micro-cracks, and particle clustering; wiping alone (Fig.3.8c) improved coverage but retained voids. The combined spray-wipe method (Fig.3.8d) achieved the most homogeneous, defect-free coating.

For coating, the inflated envelope was suspended in a rigid carbon-tube frame to prevent contact between the membrane and external surfaces (e.g., ground or supports). Suspension ensured unobstructed access to the entire envelope surface, enabling uniform coating coverage while

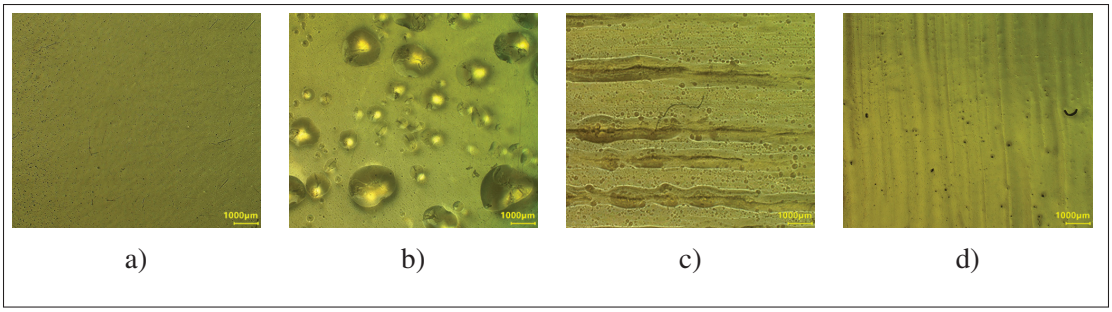

Figure 3.8 Surface morphology of LDPE samples observed with a VHX-7000 digital microscope: (a) non-coated surface, (b) after spraying, (c) after wiping, and (d) after spray-wipe coating. The spray-wipe method produced the most homogeneous and defect-free layer.

avoiding local deformation or non-uniformity in coating during application and curing. The frame also provided mechanical support for handling and repositioning. Before coating, the surface was cleaned using an alcohol-based solution sprayed at 5–6 bar from a distance of 500 mm, followed by wiping with microfiber cloths after a 2 min evaporation period.

The coating procedure consisted of three steps:

1. *Spraying:* the fluoro-siloxane sol-gel coating was applied with two passes at 5–6 bar and a 500 mm spray distance.
2. *Wiping:* after one minute of settling, the surface was wiped unidirectionally with a microfiber cloth lightly dampened with the coating solution to redistribute droplets and eliminate streaks. The coating entered a gel-like state within 10–15 min, requiring rapid execution.
3. *Curing:* the coated envelope was cured for 48 h under ventilation at 25 ± 1 °C. During curing, the surfaces became rougher and slightly opaque, consistent with surface modifications reported in plasma-treated LDPE films Sanchis, Blanes, Fenollar, Garcia & Balart (2006); Kong, Lee & Kim (2001).

The final coated LDPE envelope, suspended within its frame, is shown in Fig. 3.9.

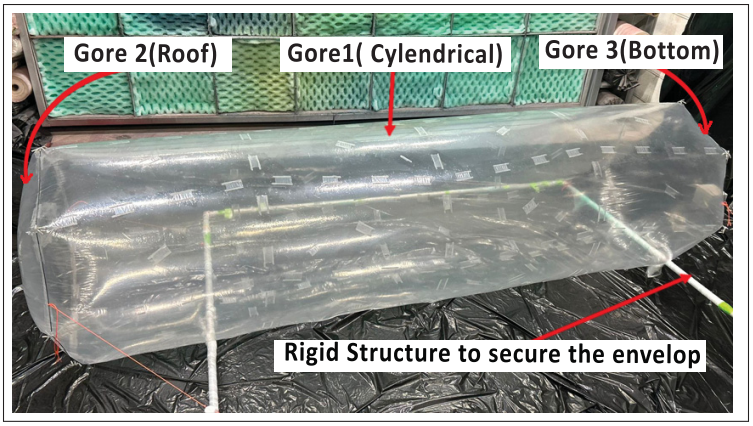

Figure 3.9 Coated envelope. The figure illustrates the main steps and resulting appearance of the coating.

The fabrication process yielded repeatable, defect-free coated LDPE envelopes that combined lightweight construction with enhanced gas retention, providing consistent test specimens for the performance evaluations presented in the following section.

3.6 Results and Discussion

This section presents a comparative evaluation of LDPE, PU, and Mylar membranes across the main performance criteria outlined in section 3.3 and 3.4. For each test, replicated trials are reported, average values are analyzed, and the observed differences are interpreted in relation to the requirements of small-scale LTA envelopes.

3.6.1 Density Measurements

Helium pycnometer measurements confirmed that raw LDPE (48 g/m^2) was substantially lighter than PU (70 g/m^2) but heavier than Mylar (27.6 g/m^2). After coating, LDPE reached 54.5 g/m^2, representing a 13.5% increase relative to the uncoated film, yet it remained 22.1% lighter than PU (Tab. 3.3). This result indicated that the coating added marginal mass while preserving LDPE's weight advantage over PU.

Table 3.3 Physical properties of selected materials: Mylar (silver), PU (white), and LDPE pure / coated (transparent). Reported density values correspond to mean values obtained from helium pycnometry (ten repetitions per sample; standard deviations were 0.0065, 0.0160, and 0.0044 g/cm^3 for Mylar, PU, and LDPE, respectively), and thickness was determined with a digital micrometer (0.001 mm device resolution, five measurements per sample). All measurements were conducted at ambient temperature (about 25 °C).

Material	Density (g/cm^3)	Thickness (mm)	Surface Density (g/m^2)
Mylar	1.0783	0.025	27.60
PU	1.3365	0.052	70.00
LDPE (Pure)	0.9674	0.049	48.00
LDPE (Coated)	0.9636	0.056	54.54

These results show that the surface treatment preserves the low areal density of LDPE while providing improved gas barrier performance. In contrast to multilayer laminates or barrier films discussed in Section 3.3, which typically achieve enhanced gas retention through substantial weight increases, the proposed coating strategy delivers functional improvement without compromising mass efficiency.

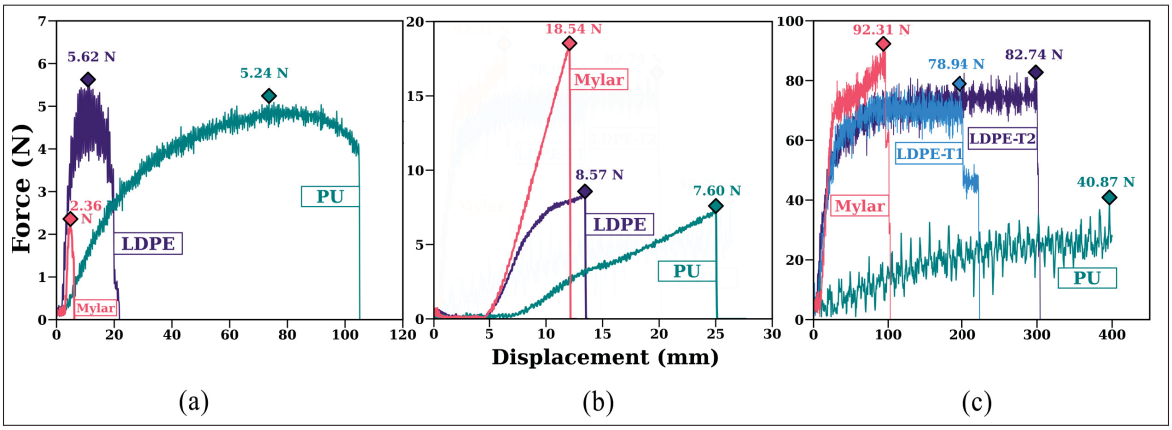

Figure 3.10 Force–displacement curves from mechanical testing: (a) tear resistance, (b) puncture resistance, and (c) tensile strength of sealed joints. Curves are representative responses from repeated tests; the annotated peak values correspond to the mean of four specimens for each material/configuration.

3.6.2 Tear Test

Tear resistance results (Fig. 3.10 a) showed LDPE as the strongest performer, averaging 5.62 ± 0.07 N, compared to PU (5.24 ± 0.08) N and Mylar (2.36 ± 0.14) N . LDPE thus exceeded PU by 9.1% and Mylar by 138.1%. The apparent fluctuations in Fig. 3.10a were attributed to electronic noise, since the measured load was small compared to the load cell capacity. These results highlighted LDPE's ability to withstand out-of-plane stresses and its clear advantage over Mylar, whose brittleness led to low tear resistance.

3.6.3 Puncture Test

Puncture resistance values (Fig. 3.10 b) revealed a different hierarchy. Mylar withstood the highest force (18.54 ± 0.20) N, but failed at relatively low displacement (11 mm), indicating a stiff yet brittle response. PU, in contrast, failed at the lowest force (7.60 ± 0.27) N, but endured the largest displacement (25 mm), demonstrating ductility without high puncture strength. LDPE exhibited an intermediate behavior (8.57 ± 0.28) N at 13 mm, offering a balance between load capacity and deformation. The larger standard deviation observed for PU indicated greater variability under localized loading.

3.6.4 Tensile Strength of welded joints

Across all configurations, failures occurred in the bulk material rather than at the joints, confirming that the thermal welding process produced interfaces stronger than the films themselves (Fig. 3.10 c). LDPE-T2 (flap joint) achieved the highest maximum load (82.74 ± 0.27) N, slightly above LDPE-T1 (78.94 ± 0.16) N, indicating that joint geometry influenced stress distribution. Mylar reached the highest absolute load (92.31 ± 0.29) N but fractured at low displacement, confirming its brittle character. PU exhibited the largest elongation (400 mm) but carried the lowest maximum load (40.87 ± 0.29) N, demonstrating ductility. The oscillations visible in the curves (Fig. 3.10 c) were attributed to a combination of stick–slip crack propagation,

as previously reported for thin polymer films Andreasson *et al.* (2013), and the large specimen extension (≈ 400 mm), which magnified displacement fluctuations during testing.

3.6.5 High specific strength

Normalizing the results by areal density (Tab. 3.4) provided insight into mechanical efficiency. Mylar achieved the best strength-to-weight performance in tensile and puncture tests, but its poor tear resistance and brittle failure undermined practical utility. LDPE provided the most balanced profile, offering moderate efficiency with superior tear resistance and ductility. PU, while flexible, underperformed in both normalized strength and permeability.

Table 3.4 Normalized strength-to-weight ratios for envelope materials (tear, puncture, and tensile performance), calculated as force (N) divided by surface density (g/m^2). The higher these values, the more mechanically efficient the material is for lightweight airship applications.

Metric (N·m^2/g)	**LDPE**	**PU**	**Mylar**
Tear Resistance	0.1171	0.0736	0.0855
Puncture Resistance	0.1781	0.1086	0.6725
Tensile Strength (Max Load)	1.723	0.584	3.345

3.6.6 Gas Barrier Test

Helium leakage tests (Fig. 3.11a) revealed Mylar as the most impermeable material, with a mean leakage rate of 0.14 g/h (98.5% lift retention over 6 h). LDPE exhibited intermediate performance (0.64 g/h, 93.6% retention), while PU performed the poorest (1.08 g/h, 84.5%). Reported values correspond to mean leakage rates obtained from repeated tests. When normalized, leakage rates were 0.84 g/h for Mylar, 3.8 g/h for LDPE, and 5.47 g/h for PU. Thus, coated LDPE retained 40.7% more lift than PU, confirming the effectiveness of the sol-gel coating.

Post-agitation tests (Fig. 3.11b) showed sharp degradation in Mylar, whose leakage rate increased eightfold (to 6.87 g/h) due to delamination of its aluminized layer. PU also worsened modestly

(to 6.47 g/h), while LDPE remained stable (3.8 g/h), reflecting the resilience of both the polymer and the applied coating under repeated deformation.

Large-scale validation using a cylindrical envelope (Sec. 3.7) confirmed these trends (Fig. 3.11c). PU leaked at 4.2 g/h, while LDPE lost only 1.7 g/h, consistent with diffusion scaling by surface area. The results are consistent with the behavior reported in prior studies and with permeability trends summarized in Sec. 3.3 and Table 3.1, accounting for differences in surface area.

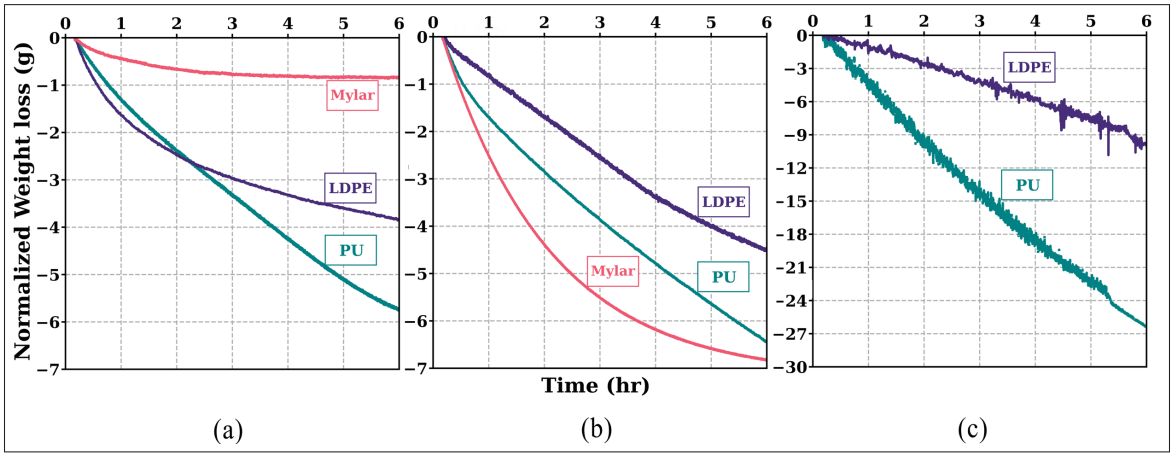

Figure 3.11 Results of gas barrier tests: (a) Helium leakage rates of pillow-shaped envelopes fabricated from LDPE, Mylar, and PU; (b) leakage rates of the same samples after mechanical agitation in a dryer; and (c) leakage rates of full-scale LDPE and PU envelopes. For cases (a) and (b), curves represent mean values obtained from three repeated tests per material. Together, these results highlight the relative effectiveness of each material in limiting gas loss, a critical parameter for assessing their suitability in practical airship applications.

3.6.7 Wettability Properties

Contact angle measurements (Fig. 3.12) confirmed that the coated LDPE surface was strongly hydrophobic (117.5°), surpassing PU (95.9°), uncoated LDPE (92.8°), and Mylar (73.9°). The coating thus significantly improved LDPE's water repellency, reducing risks of mass gain or mechanical degradation under humid conditions.

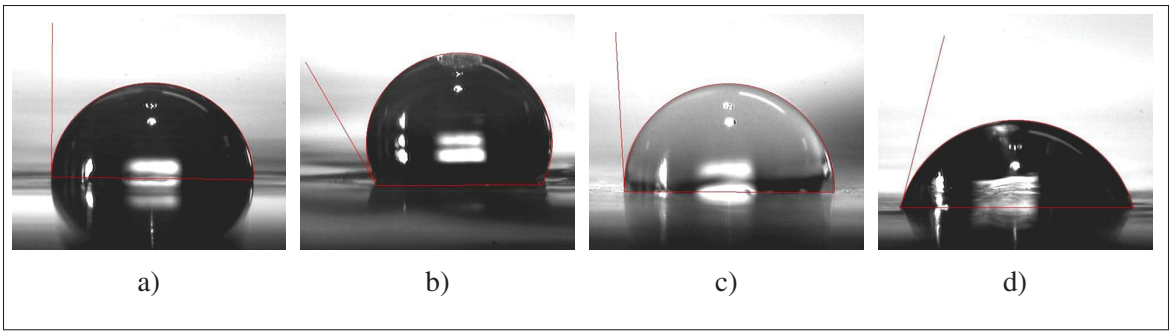

Figure 3.12 Mean contact angles of various films, illustrating wettability: (a) Uncoated LDPE film (92.75° ± 1.38°), (b) Fluoro-siloxane sol-gel coated LDPE (117.53° ± 1.89°), (c) PU film (95.88° ± 1.44°), and (d) Mylar film (73.95 ° ± 1.35 °)

3.6.8 Thermal Welding Test

Thermal welding trials highlighted clear differences in weldability among the materials. LDPE welded reliably at 170-175 °C, producing continuous weld seams with minimal deformation. PU was thermally welded at lower temperatures (110-125 °C with protective paper) but required tighter process control to avoid localized overheating. Mylar was thermally welded at 130-140 °C but was prone to wrinkling and distortion during manual handling, making fabrication more challenging. LDPE, therefore, demonstrated the widest tolerance to thermal welding conditions, supporting its use in semi-manual manufacturing.

3.6.9 Validation of Burt Behavior

Burst tests (Figs. 3.13–3.14) revealed distinct rupture behaviors. Mylar reached the highest pressure (3.53 kPa) but failed explosively, with rupture initiating at the weld transition zone, reflecting stress concentration and its brittle nature. PU failed at the lowest pressure (1.11 kPa) after a prolonged plateau, consistent with ductile deformation and gradual leakage from the film body. LDPE withstood 3.08 kPa before rupture, failing in the bulk film rather than at welds. Its controlled, non-explosive rupture indicated a balance between strength and ductility, as well as reliable weld integrity.

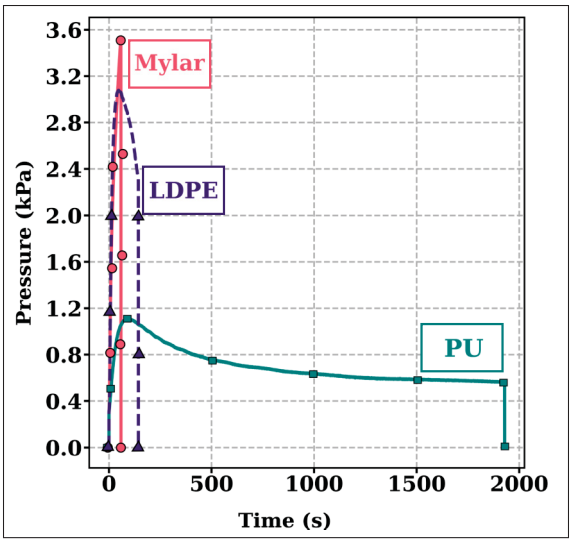

Figure 3.13 Pressure-time profiles from biaxial inflation burst tests of Mylar, PU, and LDPE envelopes, illustrating inflation behavior and rupture progression under increasing internal pressure.

3.7 Field Demonstration

A deployment trial was conducted in a partially flooded cave environment[5], characterized by narrow passages and fragile surfaces that precluded direct human exploration. The objective was to assess the capacity of an autonomous scout airship to operate reliably in confined, humid, and high-risk conditions.

In Table 3.5, for each criterion, the value in parentheses is a normalized rating on a 1–5 scale (5 = best performance, 1 = poorest), assigned by comparing the measured results of LDPE, PU, and Mylar. Based on this decision matrix, the comparative analysis of laboratory results identified coated LDPE as the most suitable candidate for envelope fabrication, achieving the highest weighted score (4.50) compared to Mylar (3.88) and PU (2.77). Although Mylar exhibited excellent helium retention, its low tear resistance, limited durability, and lack of reusability and sustainability disqualified it as a candidate, despite its higher score relative to PU. PU, while disadvantaged by high mass and rapid gas loss, was retained as a benchmark due to its

[5] Montreal's Saint-Léonard Cave

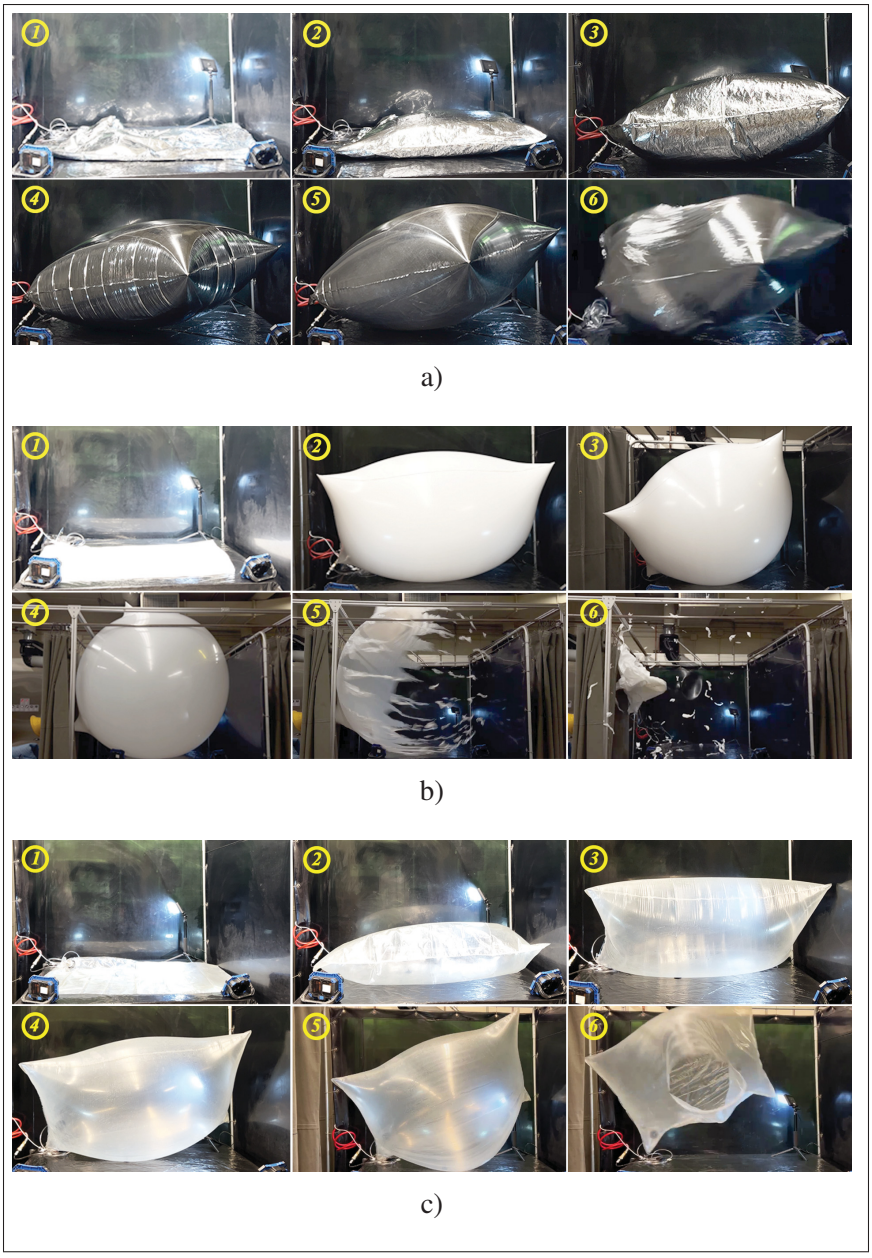

Figure 3.14 Rupture sequences for inflated envelopes (1200 × 800 mm): (a) Mylar, (b) PU, and (c) LDPE. Sequences show key stages of inflation and rupture under biaxial loading, highlighting material-specific rupture initiation, failure modes, and tear propagation.

robustness, demonstrated reusability, and established use in industrial practice. Coated LDPE provided the most balanced performance, combining durability, barrier properties, low weight, and hydrophobicity. Consequently, coated LDPE and PU were selected for full-scale field

validation. The LDPE envelope was fabricated following the protocol in sec. 3.5 and was compared with an industrially manufactured PU envelope of identical geometry (Fig. 3.15).

The most significant difference between the two materials was observed in their final envelope mass, which resulted from intrinsic material density. The LDPE envelope was lighter, thereby preserving a larger payload margin. This additional margin allowed the integration of a more secure, though heavier, valve assembly. Even with the inclusion of a heavier valve system (20.74 g including a 7 g cap), the coated LDPE envelope remained at 343 g, lighter than the PU envelope at 401 g. The coating applied to the LDPE contributed only 3 g/m^3 of additional mass, a negligible increase that remained well within operational tolerances and did not compromise payload capacity. Although it was technically feasible to employ the same one-way valve on PU, such an option has not been adopted in industrial practice, as the additional weight would have exacerbated PU's high mass, thereby reducing available payload.

Table 3.5 Decision matrix for material selection, comparing LDPE, PU, and Mylar across key parameters. Final ranking indicates overall performance for specific applications.

Technical requirement	**LDPE**	**PU**	**Mylar**	**Weight (%)**
Density (g/m^2)	48 (4)	70 (2)	27.60 (5)	20
Thickness (mm)	0.0498 (5)	0.0524 (4)	0.0256 (2)	8
Tear resistance (N)	5.62 (5)	5.15 (4)	2.36 (2)	15
Puncture resistance (N)	8.57 (3)	7.60 (2)	18.54 (5)	5
Tensile strength (N)	82.74 (4)	40.87 (2)	92.34 (5)	15
Gas-barrier performance (leakage rate)	0.64 (4)	1.08 (3)	0.14 (5)	15
Lift retention (%)	93.60 (4)	84.50 (2)	98.50 (5)	10
Hydrophobicity (CA, deg)	117.53 (5)	92.75 (2)	95.88 (2)	5
Burst pressure (structural integrity)	3.08 (5)	1.11 (4)	3.53 (1)	5
Reusable	High (5)	High (5)	Low (1)	2
Final rank	**4.50**	**2.77**	**3.88**	100

The results confirmed the laboratory findings and underscored LDPE's advantages in practical operation (Tab. 3.6). The LDPE envelope sustained a payload capacity of 250 g, significantly higher than the 164 g supported by PU, allowing the integration of both lidar and micro-camera sensors with additional mass margin for leakage compensation.

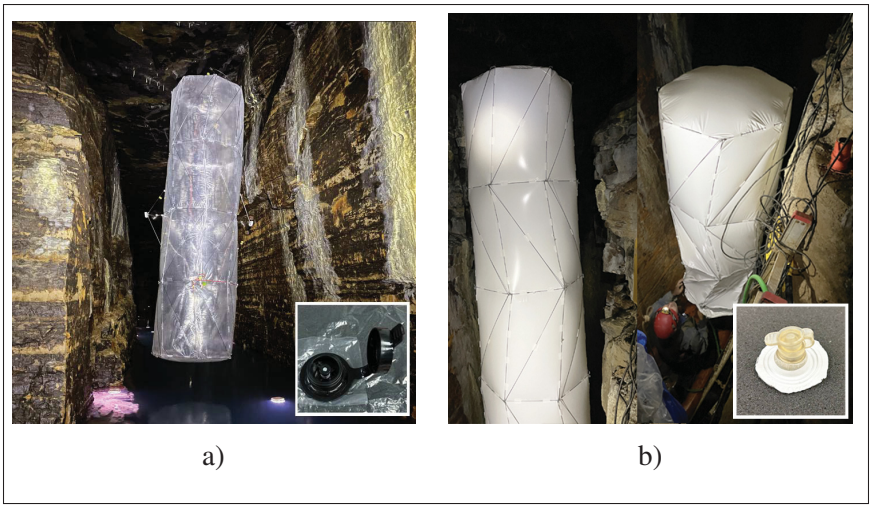

a) b)

Figure 3.15 Envelope performance during a mission in a cave environment: (a) LDPE envelope with a one-way valve assembled in the laboratory, and (b) PU envelope.

Table 3.6 Performance parameters for single-body indoor airships made from LDPE and PU, highlighting key metrics for material suitability.

Parameter	**LDPE**	**PU**
Envelope Volume (m^3)	0.86	0.86
Rigid Skeleton Weight (g)	215	215
Avionic Weight (g)	223.62	223.62
Envelope Weight (Non-Coated LDPE) (g)	325	401
Envelope Weight (Coated LDPE) (g)	343	401
Airship Free Payload Capacity (g)	250	164
Helium Loss Rate (g/h)	1.7	4.2
Moisture Absorption	None	High
Operational Endurance (hours)	72	24

Gas retention was markedly superior: the LDPE vehicle remained inflated for several days without refilling, whereas the PU envelope required replenishment twice a day. Under humid conditions, PU absorbed moisture, increasing weight and necessitating intermittent drying, while LDPE maintained stable mass and flight behavior due to its hydrophobic surface. Deployment time was also reduced: the LDPE envelope could be prepared in approximately 15 minutes, facilitated by an integrated one-way valve, compared to 25 minutes for PU using manufacturer-

supplied fittings. In terms of overall endurance, the LDPE airship sustained continuous flight for 72 hours before requiring intervention, representing a threefold improvement over the 24-hour operational lifespan of the PU envelope.

Taken together, these results validated coated LDPE as a robust alternative to conventional materials for indoor airship platforms. Its combination of lightweight structure, durability under mechanical stress, moisture resistance, and superior helium retention enabled extended mission duration in confined or humid environments, confirming its relevance for next-generation LTA systems designed for exploration and monitoring in inaccessible spaces.

3.8 Conclusion

This study developed and validated a coated LDPE composite film as an engineered solution for lightweight, gas-tight, and durable envelopes for LTA systems operating in confined spaces. By combining a thin LDPE film with a fluoro-siloxane sol–gel coating, the design achieved a balance between low surface density, high tear resistance, and improved helium retention. Comprehensive laboratory tests demonstrated that coated LDPE rivaled or exceeded the performance of conventional PU and Mylar films across key metrics, while maintaining superior flexibility, hydrophobicity, and compatibility with semi-manual thermal welding processes.

A field demonstration in a partially flooded cave further confirmed the composite film's practical viability, enabling higher payload capacity, easier deployment, and up to threefold longer flight endurance compared to PU. These findings not only established the coated LDPE film as a reliable structural-functional composite for indoor airships but also illustrated a generalizable materials-engineering pathway for lightweight polymer composites in soft robotic and aerospace applications.

Future work will extend this approach toward scalable manufacturing, optimization of envelope geometry to reduce seam length, and assessment under long-term or outdoor operation. In addition, future work will be required to quantitatively validate and characterize the anisotropy

of LDPE. These efforts will further consolidate coated LDPE as a versatile material for persistent aerial exploration in complex environments.

3.9 Acknowledgements

We would like to thank the Fonds de recherche du Québec – Nature et technologies (FRQNT) for their financial support (Team grant #283381), which made this work possible.

CHAPTER 4

FINITE ELEMENT SIMULATION OF SLTA ENVELOPES: NON-RIGID VS. SEMI-RIGID STRUCTURES

4.1 Introduction

This chapter presents finite element simulations aimed at comparing the structural response of two indoor SLTA envelope configurations:

(i) **Non-rigid airship (system I):** a purely inflatable configuration composed of a single bladder (Figure 4.1a);

(ii) **Semi-rigid airship (system II):** an inflatable bladder reinforced by a lightweight external exoskeleton (Figure 4.1b).

The goal of this chapter is to determine how adding a lightweight semi-rigid exoskeleton modifies the mechanical response of an indoor SLTA envelope relative to a purely inflatable bladder, with emphasis on impact events that are difficult to avoid in confined environments. By comparing load transfer, peak membrane stresses, indentation, wrinkling severity, and energy absorption during pressurization and low-velocity wall contact, the study identifies whether the semi-rigid architecture improves bladder protection and geometric stability, and provides design guidance for future indoor airships expected to experience repeated collisions.

4.2 Explicit Dynamic Analysis for thin-wall membranes

All numerical simulations in this study were performed using the Abaqus/Explicit solver, which is well-suited for problems involving large deformations, nonlinear material behavior, and evolving contact conditions. These characteristics are typical of thin, pressurized membrane structures subjected to internal inflation and low-velocity impact loads. The use of an explicit dynamic formulation for inflatable structures has been widely validated in the literature (Pecora, 2017; Dassault Systèmes Simulia Corp., 2024).

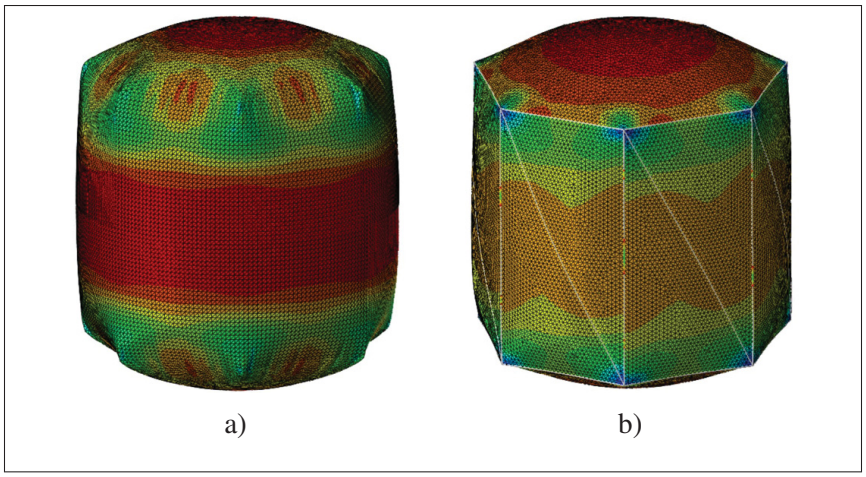

Figure 4.1 Airship configurations: (a) non-rigid/system I (main bladder) and (b) semi-rigid/system II (main bladder reinforced with a lightweight exoskeleton).

In Abaqus/Explicit, the structural response is integrated in time using an explicit central-difference scheme, in which the equations of motion are advanced incrementally without the need for global matrix inversion. The time increment is determined automatically based on the numerical stability criterion, resulting in a variable time-step formulation. This approach provides robust performance for highly nonlinear membrane problems and enables the system to evolve dynamically toward a quasi-static equilibrium during pressurization and impact events (see Appendix 1.

In this chapter, unless otherwise stated, results for the SLTA envelope are displayed as Abaqus contour plots using the default rainbow color spectrum, where red indicates high values and blue indicates low values of the reported quantity. When present, the contour legend provides the corresponding numerical scale.

4.3 Model Geometry and Discretization

Traditional geometries such as spheres, ellipsoids, and prolate bodies, although widely used in LTA systems, were found to be less suitable for indoor applications due to their limited adaptability to highly constrained environments. Such shapes can restrict maneuverability and reduce

compliance when navigating confined spaces with irregular layouts or rigid obstacles. During the early design phase, alternative configurations, including cubic, icosahedral (Schwemmer, Palazotto & Chrissis, 2018; Adorno-Rodríguez, 2014; Metlen, 2013; Cranston, 2016), pillow-shaped, and pyramidal geometries, were explored to identify a form compatible with modular reinforcement strategies and confined operation.

The geometry selected for numerical analysis was a cylindrical body with a regular heptagonal cross-section, developed within the same underground exploration research project (Catar *et al.*, 2024). Before prototyping, structural simulations were conducted to assess the mechanical feasibility of this configuration and to compare the structural response of non-rigid and semi-rigid airship systems.

To reduce computational cost while preserving the dominant load paths and deformation mechanisms, all simulations were performed on a quarter-section of a single heptagonal module, which is described in Chapter 3. This reduced-order model retains the essential geometric features and boundary conditions required to evaluate stress distribution, global deformation, and reinforcement effectiveness.

The numerical model comprises three primary components: the inflatable bladder (main envelope), the external exoskeleton, and a rigid obstacle used for impact simulations. The principal geometric dimensions of the bladder and exoskeleton are summarized in Table 4.1, and the overall geometry is illustrated in Figure 4.2.

4.3.1 Main bladder

The inflatable bladder was modeled as a three-dimensional deformable shell in Abaqus/CAE. The bladder geometry corresponds to a prismatic body with a regular heptagonal cross-section. A vertical partition was introduced to improve mesh control, ensure consistent orientation, and facilitate assembly with the exoskeleton and contact definitions (Figure 4.3a).

Table 4.1 Geometrical parameters of the bladder and bladder exoskeleton (in SI units).

Component	Parameter	Value	Unit
Bladder	Height (1/4 of final prototype)	0.6110	m
	Outer diameter of section (circumscribed)	0.7200	m
	Heptagon side length	0.3124	m
Exoskeleton	Height (1/4 of final prototype)	0.6111	m
	Outer diameter of section (circumscribed)	0.7200	m
	Heptagon side length	0.3124	m
	Outer tube radius	0.0020	m
	Tube Wall thickness	0.0005	m

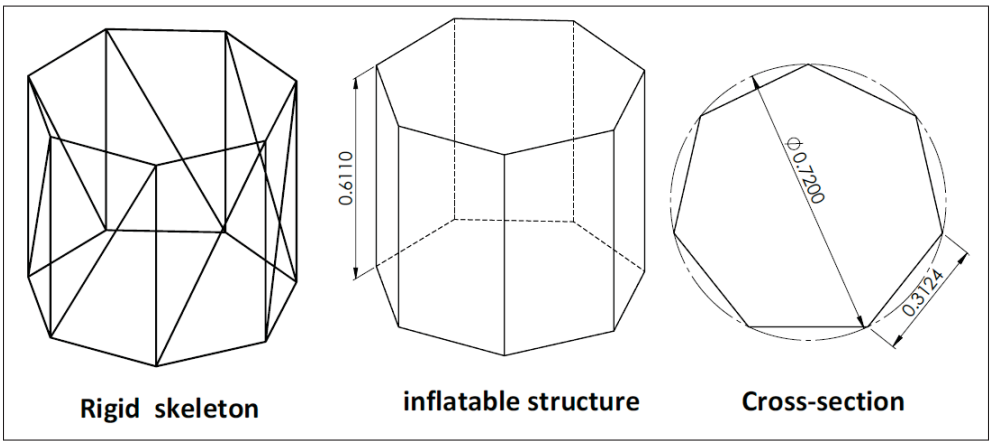

Figure 4.2 Cylindrical body with a heptagonal cross-section, designed by Louis Catar *et al.* within the framework of the same research project (Catar *et al.*, 2024).

The bladder was modeled as a single-layer LDPE membrane with a thickness of $t = 5 \times 10^{-5}$ m and a density of 967.4 kg/m^3. Mechanical properties were obtained from literature sources ((Martínez-Camacho *et al.*, 2013; International, 2024; Kaci *et al.*, 2005; Pecora, 2017)) and experimental characterization presented in Chapter 3. Although LDPE is commonly treated as an orthotropic material, comparative simulations showed negligible differences between orthotropic and isotropic formulations for the stress and deformation metrics of interest. An isotropic material model was therefore adopted for computational efficiency. The material parameters implemented in the simulations are summarized in Table 4.2.

The bladder was discretized using M3D3 triangular membrane elements, which transmit in-plane forces only and are well-suited for thin-film structures undergoing large deformations. Membrane normal orientation, required for correct pressure loading and contact assignment, was defined consistently across the model; details of the SPOS/SNEG convention used in Abaqus are provided in Appendix 2. A mapped triangular mesh with a global element size of 0.01 m was adopted as a compromise between geometric resolution and computational cost (Figure 4.4a).

Table 4.2 Mechanical properties of the LDPE implemented in simulation.

Property	**Value**	**Unit**
Density, ρ	967.4	kg/m^3
Thickness, t	5.0×10^{-5}	m
Young's modulus, E	27×10^6	Pa
Poisson's ratio, ν	0.35	–
Plasticity data		
Yield stress	**Plastic strain**	**Unit**
9.0×10^6	0.0	Pa
10.5×10^6	0.1	Pa
12.0×10^6	0.2	Pa
13.2×10^6	0.3	Pa
14.0×10^6	0.4	Pa
14.5×10^6	0.5	Pa
14.7×10^6	0.6	Pa
Ductile damage properties		
Fracture strain	3.27	–
Stress triaxiality	–0.33	–
Strain rate	0	s^{-1}
Damage evolution		
Fracture energy	1500	J/m^2
Softening	Linear	–
Degradation	Maximum	–

4.3.2 Bladder exoskeleton

The cross-sectional dimensions of the carbon tubes were selected based on a compromise between structural stiffness, mass efficiency, and integration constraints imposed by other design constraints of the SLTA, such as mecatronics fixtures, assembly, and impact protection patches. As demonstrated by the simulations below, this sizing provides sufficient bending stiffness to limit deformation during both pressurization and impact, while maintaining a negligible mass penalty relative to the overall buoyant capacity of the system. The exoskeleton was modeled as a three-dimensional deformable wire structure forming a lightweight reinforcement network along the edges and diagonals of the heptagonal envelope (Figure 4.3b). The structure was discretized using B32 quadratic beam elements, which accurately capture axial, bending, and torsional behavior of slender members.

A circular thin-walled pipe section was assigned to the beams, consistent with the carbon tubes used in fabrication. Material properties were specified based on the manufacturer's datasheet and implemented using an isotropic elastic–plastic model. The corresponding parameters are summarized in Table 4.3. Beam orientation and section definition were implemented using standard Abaqus procedures; implementation details are provided in Appendix 3. A global element size of 0.01 m was selected to ensure compatibility with the membrane discretization.

Table 4.3 Material properties of the exoskeleton (carbon tube).

Property	**Value**	**Unit**
Density	1570	kg/m^3
Young's Modulus	230×10^9	Pa
Poisson's Ratio	0.30	–
Yield Stress	230×10^6	Pa
Outer Radius (Beam Pipe)	0.002	m
Wall Thickness (Beam Pipe)	0.0005	m

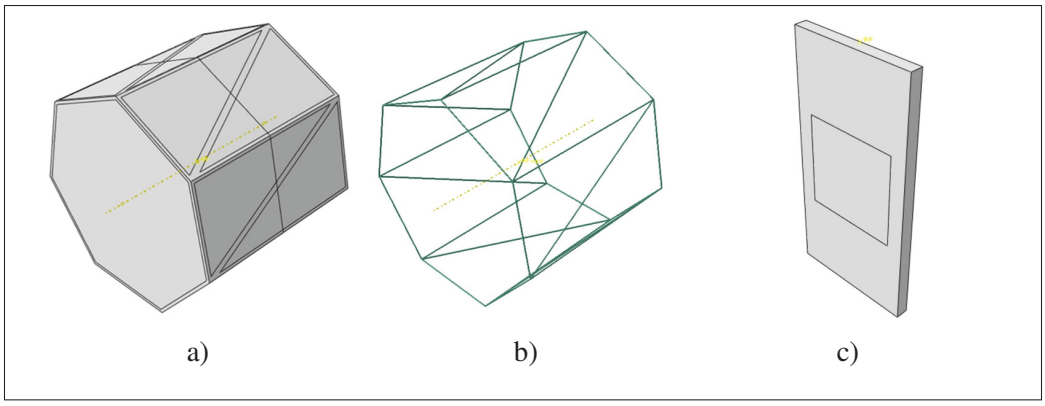

Figure 4.3 Finite element geometries used in simulations: (a) inflatable envelope (main bladder) with partitions, (b) exoskeleton, and (c) rigid obstacle for impact testing.

4.3.3 Rigid Obstacle

The rigid obstacle used in the impact simulations was modeled as a discrete rigid surface representing a planar wall encountered during indoor operation (Figure 4.3c). The wall was defined as a rectangular rigid plate with dimensions 2 m $\times$ 1 m and a thickness of 0.1 m. These dimensions were selected to fully encompass the maximum expected contact area of the deforming envelope during impact and to avoid edge effects.

The wall was modeled as analytically rigid, such that no deformation occurred during contact. This assumption isolates the structural response of the airship envelope and exoskeleton, ensuring that all observed deformation, stress localization, and energy dissipation originate from the inflatable structure rather than from the obstacle.

The obstacle was meshed using R3D3 rigid triangular elements, with local refinement in the contact region to ensure accurate surface-to-surface interaction. The rigid body motion was governed by an associated reference point (RP), enabling stable application of boundary conditions and contact enforcement. Further details regarding rigid body definition and meshing strategy are provided in Appendix 4.

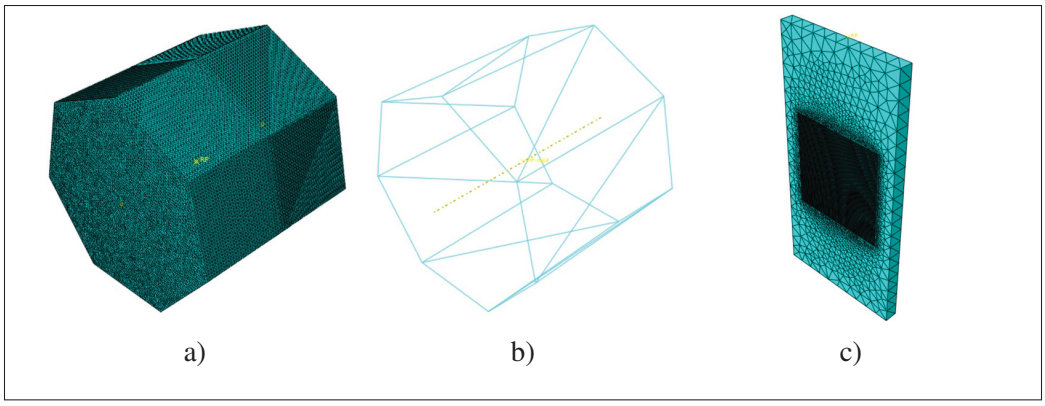

Figure 4.4 Finite element meshes used in simulations: (a) bladder with M3D3 elements, (b) exoskeleton with B32 beam elements, and (c) rigid obstacle with R3D3 elements.

4.4 Pressurization Behavior Analysis

4.4.1 Internal Pressurization Modeling

The pressurization analysis is first employed as a validation step to assess the ability of the proposed semi-rigid architecture to maintain the intended envelope geometry under operational inflation levels. Rather than serving as a primary load case, this analysis establishes the structural role of the exoskeleton in controlling deformation, suppressing excessive wrinkling, and preserving effective lifting volume before evaluating impact response. This distinction is essential, as geometric stability under inflation directly conditions the airship's behavior during subsequent contact events.

Internal pressurization of both system I and system II was modeled using the fluid cavity formulation in Abaqus/Explicit, which dynamically updates the internal gas pressure as a function of cavity volume and membrane deformation (Bonet, Wood, Mahaney & Heywood, 2000; Dassault Systèmes Simulia Corp., 2024). This approach ensures a consistent evaluation of stress and deformation during inflation and allows the influence of the exoskeleton on bladder response to be directly quantified. Helium was selected as the working gas and modeled under adiabatic conditions, which is appropriate for rapid pressurization, where heat exchange with the surroundings is negligible In Abaqus, the fluid cavity is bounded by the SNEG face of the

bladder surface and associated with a dedicated reference point (RP) that controls the pressure degree of freedom (DOF 8). Under adiabatic ideal-gas assumptions, the pressure evolution is governed by

$$P(t) = P_0 \left(\frac{V_0}{V(t)} \right)^{\gamma}, \tag{4.1}$$

where P_0 is the initial pressure, V_0 the initial cavity volume, $V(t)$ the instantaneous cavity volume, and $\gamma = c_p/c_v$ is the adiabatic index. For monatomic gases such as helium, $\gamma \approx 1.66$, implying that pressure variations arise solely from volumetric compression and expansion during inflation.

The simulation was initialized at $P_0 = 0$, and the internal pressure was ramped smoothly to a peak value of 1500 Pa, corresponding to the experimentally measured post-inflation pressure for the same bladder geometry. No external kinematic constraints were applied to the bladder during pressurization, allowing the internal pressure to drive the fully coupled fluid–structure response.

To contextualize the numerical stress levels, the maximum bladder stress was estimated using thin-shell theory for a combined cylindrical and hemispherical configuration:

$$\sigma_{\max} = \frac{P}{t} \left(R_{\text{cyl}} + R_{\text{cap}} \right), \tag{4.2}$$

where $P = 1500$ Pa, $t = 5 \times 10^{-5}$ m, $R_{\text{cyl}} = 0.342$ m, and $R_{\text{cap}} = 0.610$ m, yielding $\sigma_{\max} = 28.56$ MPa. A detailed derivation is provided in Appendix 6. This stress level exceeds the elastic limit of LDPE (yield stress 14.7 MPa, Table 4.2), indicating plastic deformation during inflation, while remaining below the failure threshold due to the material's ductile damage evolution. The selected peak pressure is consistent with the experimentally measured value of 1480 Pa, further validating the boundary conditions.

4.4.2 Mesh convergence evaluation and time-period selection

A mesh convergence and time-period sensitivity study was conducted to verify numerical robustness and determine an efficient simulation setup. Two global bladder mesh sizes were

evaluated: 0.03 m (4,436 elements) and 0.01 m (41,558 elements). While the coarser mesh captures the overall geometry, the finer mesh improves the resolution of localized wrinkling. The hoop stress component S_{11} was monitored in the central cylindrical region, where thin-shell assumptions are most applicable.

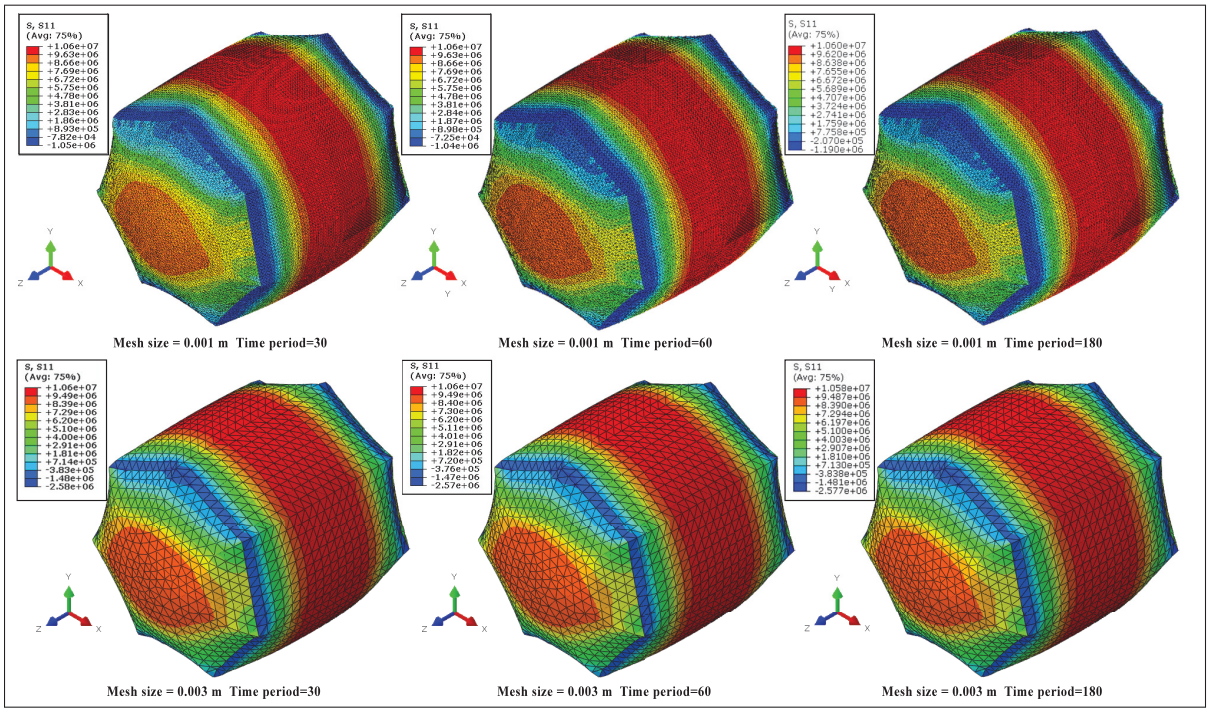

Figure 4.5 Comparison of the hoop stress component S_{11} in the central cylindrical region for two global mesh sizes (0.03 m and 0.01 m) and three simulation durations (180 s, 60 s, and 30 s). The color contours represent the magnitude of S_{11}, with red indicating higher stress levels and blue indicating lower stress levels. For the cases shown, the maximum stress value is approximately 10.5 MPa and the minimum stress value is approximately −2.6 MPa, as indicated by the contour legends.

Figure 4.5 compares the S_{11} distributions obtained for both meshes and for three simulation durations (180 s, 60 s, and 30 s). All configurations produced a converged maximum S_{11} of approximately 10.6 MPa, indicating spatial and temporal convergence.

For reference, the analytical hoop stress for a thin-walled cylinder is

$$\sigma_{\text{cyl}} = \frac{PR_{\text{cyl}}}{t} = \frac{1500 \times 0.342}{5 \times 10^{-5}} = 10.26 \text{ MPa}. \tag{4.3}$$

The FE-computed value $S_{11}^{\mathrm{FE}} = 10.60$ MPa yields a relative error of

$$\% \text{ Error} = \left| \frac{S_{11}^{\mathrm{FE}} - S_{11}^{\mathrm{analytical}}}{S_{11}^{\mathrm{analytical}}} \right| \times 100, \tag{4.4}$$

corresponding to 3.3% for all cases.

Explicit mass scaling was employed to achieve a stable time increment of 1.0×10^{-5} s, with Abaqus adjusting the effective density accordingly. Throughout inflation, the kinetic-to-internal energy ratio remained below 5%, confirming quasi-static conditions (see Appendix 5). Although a duration of 180 s matches the experimental inflation process, the objective of this study is the final inflated state rather than transient dynamics. A 30 s simulation reproduced identical S_{11} results while significantly reducing computational cost. The 0.01 m mesh was retained for all subsequent analyses due to its improved wrinkling resolution and closer agreement with experimentally observed post-inflation shapes.

4.4.3 Interaction Modeling (system II)

In system II, the exoskeleton was connected to the outer surface of the bladder through discrete attachment patches distributed along the edges of the heptagonal module (Figure 4.6). In the numerical model, these attachment regions were implemented by partitioning the bladder surface, forming a cage-like support layout that simplifies interaction modeling while reflecting the localized attachment strategy used in the physical prototype.

A surface-to-surface tie constraint was defined between the exoskeleton (secondary surface) and the corresponding bladder patches (main surface), ensuring full transfer of translational and rotational degrees of freedom at the attachment locations. The default position tolerance with automatic secondary surface adjustment was used to accommodate non-conforming meshes. This configuration idealizes a strong localized bond while allowing the remaining bladder surface to deform freely. Identical pressurization and boundary conditions were applied to system I and system II to enable direct comparison.

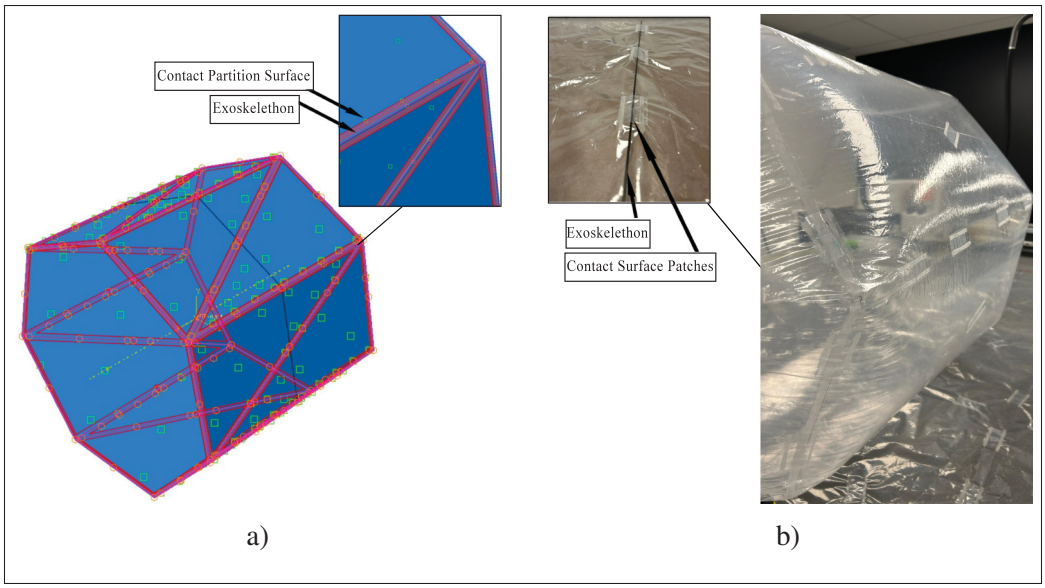

Figure 4.6 Interaction between the bladder and the exoskeleton: (a) attachment/contact surface on the bladder in the numerical model, (b) attachment patches on the physical bladder in the experiment.

The tie constraint used to model the bladder–exoskeleton interface idealizes the attachment as perfectly bonded, neglecting local compliance, slippage, or progressive de-bonding that may occur in practice. This assumption is conservative with respect to load transfer, as it maximizes force transmission from the bladder to the exoskeleton. While local attachment flexibility may slightly reduce peak stresses in the frame, the adopted model provides an upper-bound estimate of structural demand and is appropriate for evaluating global load redistribution.

4.4.4 Boundary Condition at Pressurization

During pressurization, a displacement/rotation boundary condition was applied to the bladder RP. All rotational degrees of freedom (UR1, UR2, UR3) were constrained, ensuring that the RP acted solely as a pressure control node, while translational degrees of freedom (U1, U2, U3) were left unconstrained to permit free membrane deformation. A spatially uniform, predefined temperature field with a value of zero was applied throughout the cavity region. In the Abaqus formulation, this value represents a thermally neutral reference state rather than a physical

temperature, ensuring that pressure evolution is governed exclusively by volumetric deformation under adiabatic conditions.

Inflation sequences for system I and system II are shown in Figures 4.7 and 4.8. System II preserves the intended geometry more effectively during inflation due to the stiffening effect of the exoskeleton, which limits severe local stretching, reduces stress concentrations at sharp corners, and helps maintain the effective lifting volume. In contrast, large local bulging or deep wrinkling in system I redistributes internal gas into folds or lobes, reducing local buoyancy and controllability. Over repeated inflation cycles, such distortions may accumulate, leading to degraded operational performance in confined environments.

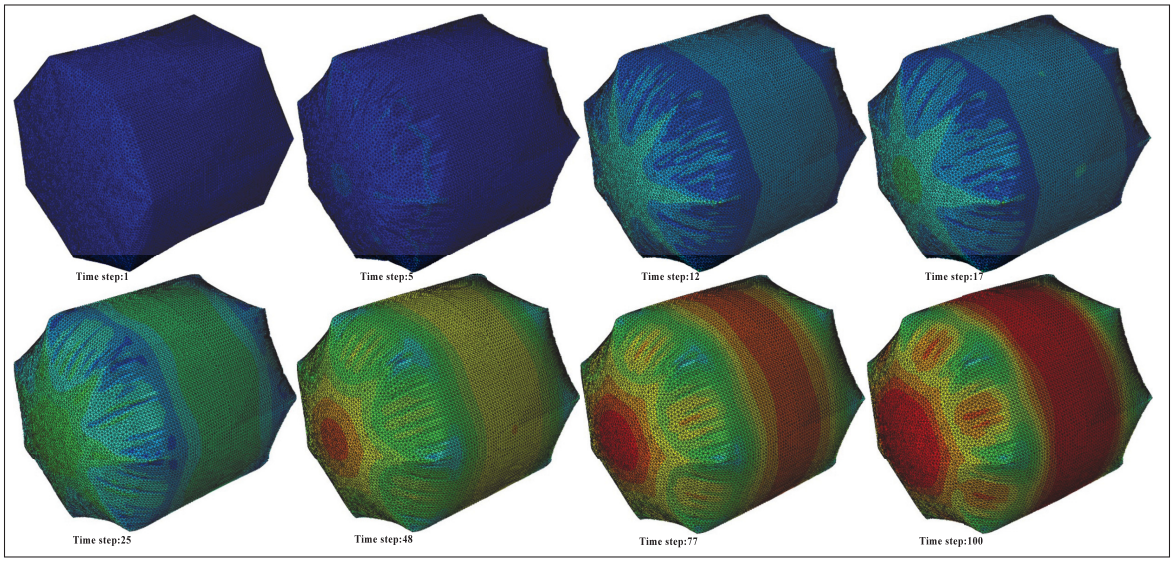

Figure 4.7 Inflation sequence of system I (non-rigid), extracted from the evolving von Mises stress field. The color contours represent the magnitude of the von Mises stress during inflation, with minimum and maximum values of approximately 2.05 MPa and 9.4 MPa, respectively. The values are summarized in Table 4.4

Because stress magnitudes differ significantly between the bladder and the exoskeleton in system II, separate display groups were used during post-processing to isolate component-level stress and deformation without visual dominance of the higher stresses carried by the reinforcing frame.

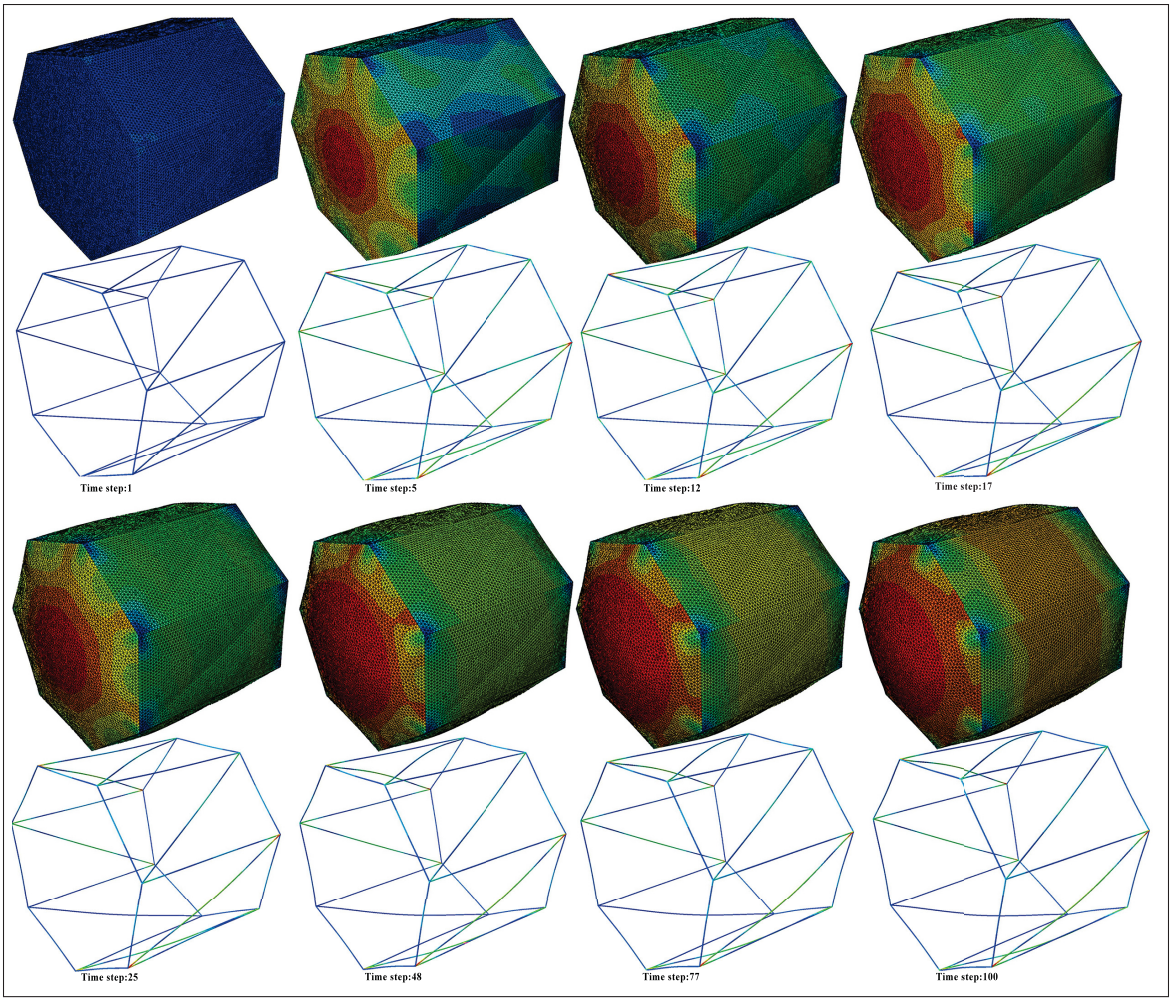

Figure 4.8 Inflation sequence of system II (semi-rigid), extracted from the evolving von Mises stress field. The maximum von Mises stress reaches 496 MPa (red) in the exoskeleton and 10.4 MPa (red) in the bladder, while the minimum stress value is approximately 0.20 MPa (blue) for both components. The values are summarized in Table 4.4.

4.5 Impact Behavior Analysis

The impact response of system I and system II was investigated using explicit dynamic simulations in Abaqus/Explicit. In these analyses, the inflated airship module was driven against a rigid obstacle to represent collisions encountered in confined or cluttered indoor environments. Contact interactions were modeled using a surface-to-surface general contact formulation with an explicit penalty method. Normal behavior was defined as hard contact, and a friction coefficient of 0.3

was prescribed to approximate polymer–wall interaction. Separation after contact was permitted to allow rebound following impact, consistent with experimental observations.

Contact between the LTA system and the rigid wall is modeled using a frictional surface-to-surface formulation with hard normal contact and a constant friction coefficient. This approach neglects surface roughness variability, local damping effects, and air cushioning at very small stand-off distances. These simplifications are acceptable for low-velocity indoor impacts, where structural compliance dominates the response. Nevertheless, the results should be interpreted as representative of worst-case rigid-contact scenarios rather than exact replicas of all real-world interactions.

For both configurations, the initial internal pressure and imposed impact velocity were kept identical. The contact domain included all external surfaces of the bladder, exoskeleton (for system II), and rigid obstacle. Key response metrics included peak bladder stress, maximum deformation, wrinkling development, and absorbed impact energy. The evolution of stress, deformation, and internal energy at the primary impact location was monitored to compare the impact tolerance of the two structural concepts.

4.5.1 Boundary Condition at Impact

During impact simulations, the rigid obstacle was fully constrained using an ENCASTRE boundary condition ($U_1 = U_2 = U_3 = UR_1 = UR_2 = UR_3 = 0$), ensuring that it remained fixed throughout the analysis. Before the explicit impact step, the bladder was re-pressurized again by a new internal pressure of 800 Pa, reduced from the nominal inflation pressure of approximately 1500 Pa. During the impact step, the cavity pressure was held constant and not actively driven.

Operating at a reduced internal pressure increases membrane compliance, thereby enhancing the visibility of contact-induced deformation, wrinkling, and rebound behavior. This choice also reflects realistic indoor operation, where airship envelopes are not maintained at their maximum allowable pressure to preserve structural integrity and safety during repeated contact events.

The selected pressure, therefore, represents a controlled yet operationally relevant condition for comparing reinforced and non-rigid configurations.

The impact sequences shown in Figures 4.10 and 4.11 illustrate the deformation process during contact for the two configurations. These sequences capture localized indentation at the impact site, the development of contact-induced wrinkling, and the subsequent rebound motion. Distinct differences in stress localization, wrinkling patterns, and deformation at the impacted corner are evident, as highlighted in the close-up view shown in Figure 4.9.

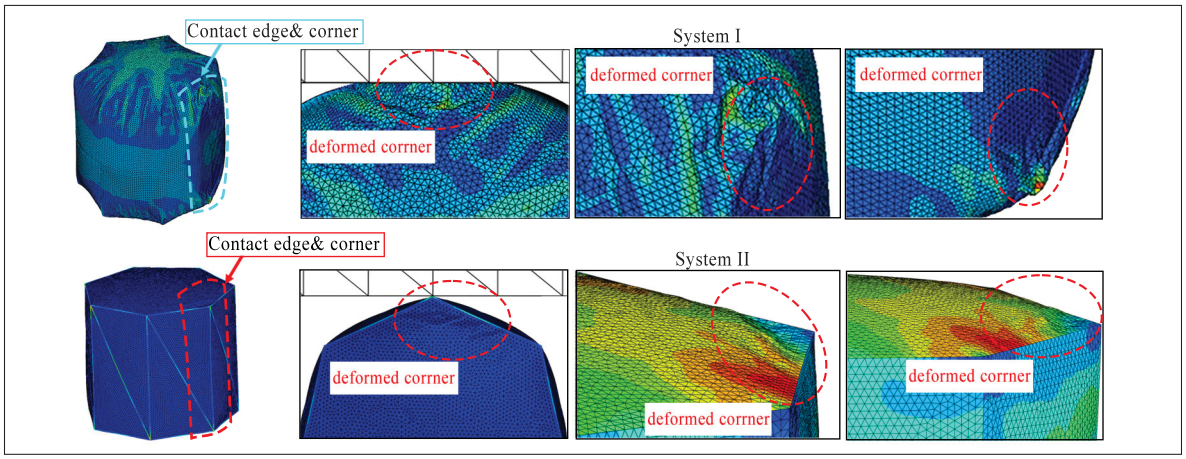

Figure 4.9 Close-up view of the corner region involved in impact, highlighting local stress concentration, wrinkling, and deformation for system I, system II, and the bladder. The corresponding maximum deformation values are summarized in Table 4.5.

In system II, the presence of the exoskeleton introduces additional load paths that participate in the contact response. As in the pressurization analysis, stress and deformation fields in the bladder and exoskeleton were evaluated separately using component-specific display groups, ensuring that bladder-level behavior was not visually masked by higher stress levels in the reinforcing frame. Quantitative comparisons of deformation amplitude, stress distribution, wrinkling extent, and energy absorption are presented in the following results section.

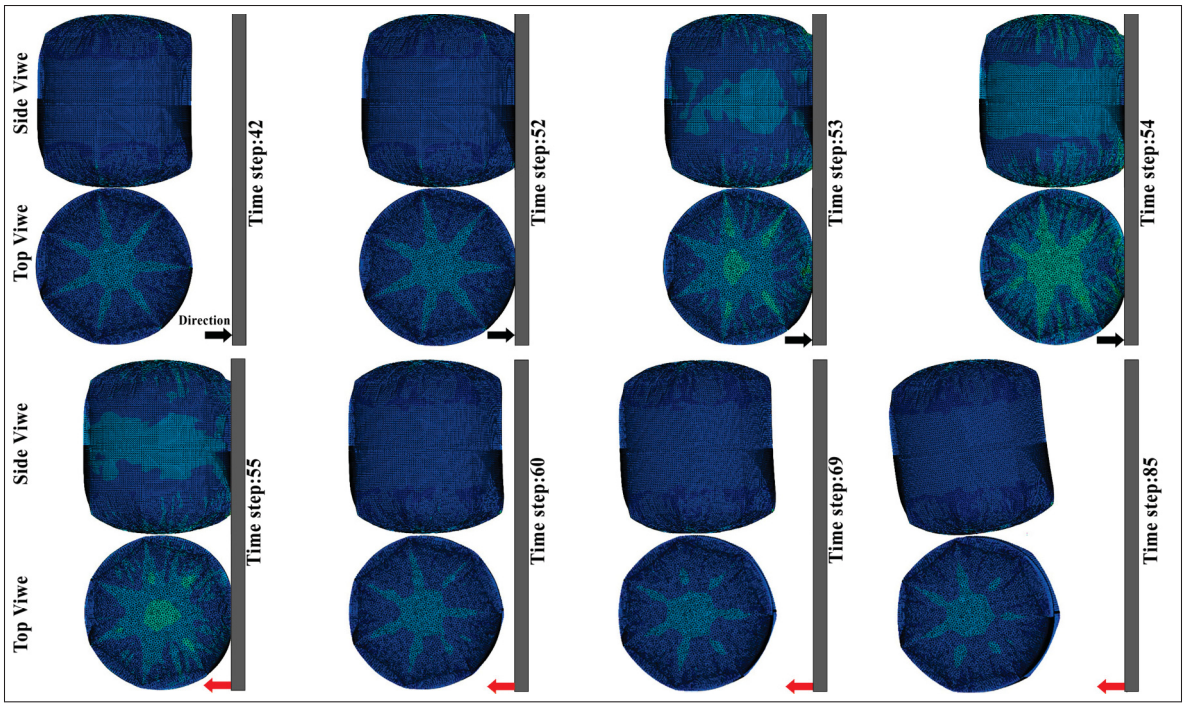

Figure 4.10 Impact sequence of the first system (system I). Quantitative peak stress and deformation values corresponding to this impact event are summarized in Table 4.5.

4.5.2 Impact step duration and time-window selection

The explicit impact step was defined to include the complete approach, contact, and rebound sequence, starting from the onset of motion following pressurization. Identical initial velocity, internal pressure, and boundary conditions were prescribed for both structural configurations.

An initial impact duration of 0.88 s was sufficient for system I to complete approach, contact, maximum indentation, and rebound. Extending the step duration did not affect peak stress, deformation, or energy metrics. For system II, however, no contact occurred within this time window due to increased stiffness and inertia introduced by the exoskeleton. The impact step for system II was therefore extended to 5 s to capture the full contact and rebound sequence. These different durations reflect differences in dynamic response rather than differences in loading.

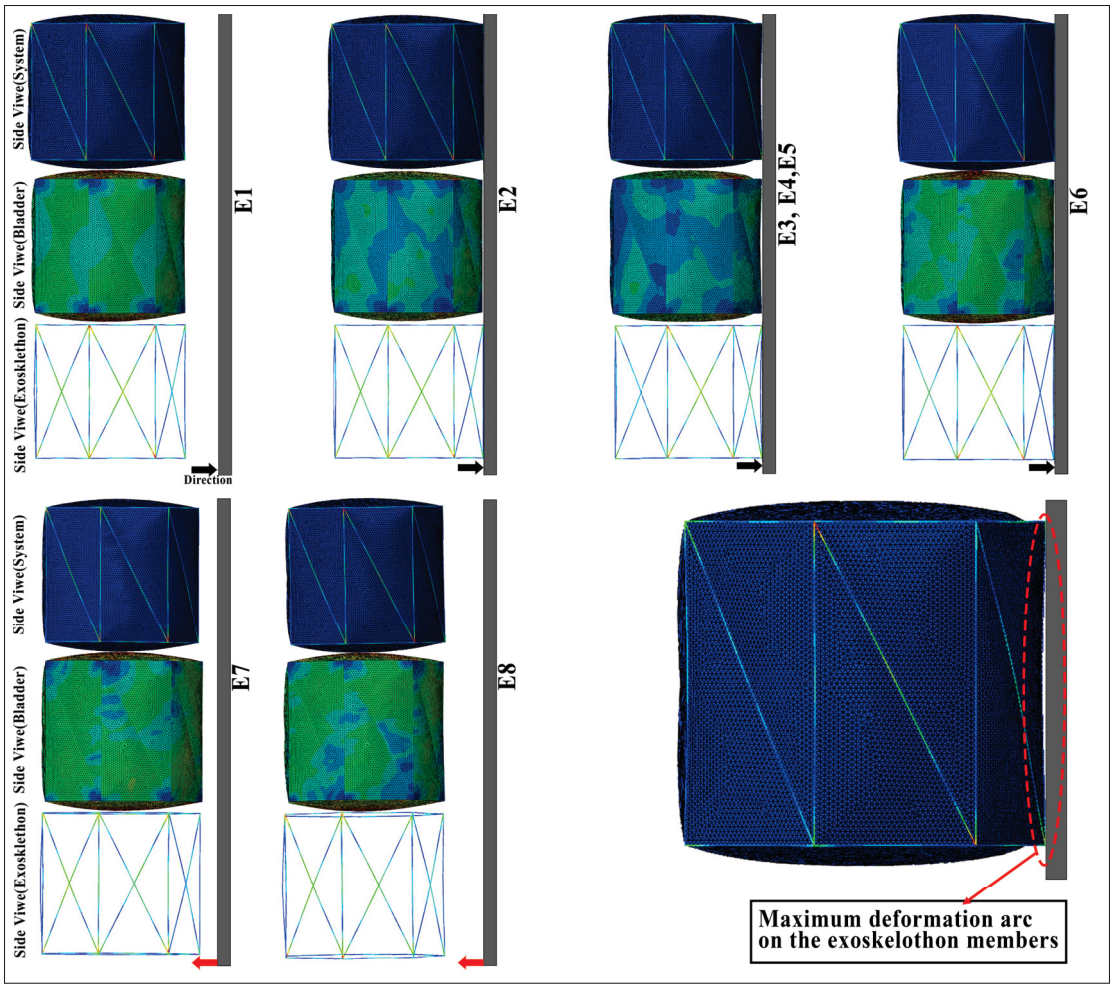

Figure 4.11 Impact sequence of the first system (system II). Quantitative peak stress and deformation values corresponding to this impact event are summarized in Table 4.5.

To enable consistent comparison between configurations, results are evaluated at characteristic impact events rather than at identical simulation times. The impact process was decomposed into eight events:

- **E1**: approach before contact,
- **E2**: first contact,
- **E3**: early contact loading,
- **E4**: maximum indentation,
- **E5**: late loading and onset of recovery,
- **E6**: unloading and rebound while still in contact,

- **E7**: post-impact rebound after separation,
- **E8**: post-impact recovery during free flight.

All impact-related stress, deformation, and internal-energy results are reported with respect to these event labels (E1–E8) to ensure physically consistent comparison between systems I and II.

4.5.3 Load

To represent a typical collision event, the airship was assigned a uniform initial impact velocity of 3 m/s. This value corresponds to the upper range of translational speeds expected during indoor SLTA operation in confined environments, based on propulsion capability, controllability requirements, and safety considerations for human-adjacent operation. As such, it represents a conservative scenario intended to bound the severity of typical wall or obstacle contacts.

This velocity range was further validated experimentally. The complete SLTA system was freely flown in an indoor environment, and its motion was recorded using a camera. Post-processing of the recorded footage using the *Tracker* motion analysis software showed translational velocities consistently close to 3 m/s. In parallel, onboard motor data logging confirmed that the commanded and measured propulsion speeds during normal operation remained within the same range. These experimental observations confirm that the selected impact velocity is representative of realistic operational conditions rather than an arbitrary or overly conservative assumption.

At this velocity level, the associated strain rates in the bladder remain low, and the membrane response is dominated by elastic and ductile plastic behavior, consistent with the quasi-static tensile and burst tests reported in Chapter 3. Rate-dependent viscoelastic effects are therefore neglected without compromising the validity of the comparative impact analysis.

4.6 Results and Discussion

4.6.1 Stress and global deformation at pressurization

Stress distribution, global deformation, and wrinkling behavior are evaluated at the pressurization equilibrium state reached at an internal overpressure of $P = 1500$ Pa. This enables a direct comparison between the system I configuration and the system II configuration as well as an assessment of how the semi-rigid frame contributes to protecting the thin bladder from damage under sustained internal pressure. Contours of von Mises stress and the longitudinal membrane stress component S_{11}

For system I, the equilibrium stress state remains within the membrane scale, with $\sigma_{\mathrm{vM}}^{\max} \approx 9.40$ MPa and $S_{11}^{\max} \approx 10.7$ MPa. In system II, the maximum stresses reported at the assembly level are substantially higher because they are governed by the exoskeleton response rather than by the bladder. The semi-rigid assembly reaches $\sigma_{\mathrm{vM}}^{\max} \approx 496$ MPa and $S_{11}^{\max} \approx 448$ MPa, reflecting load transfer and stress concentration within the frame members during inflation.

To avoid ambiguity in interpreting stress levels in the semi-rigid configuration, results are discussed at two scales: (i) *assembly-level* maxima, which characterize global load demand in the coupled system, and (ii) *component-level* fields extracted separately for the bladder and the exoskeleton using dedicated display groups.

Component-level results confirm that bladder stresses remain of the same order in both configurations. When the bladder-only fields of system II are isolated, von Mises and longitudinal stresses remain close to 10 MPa, comparable to system I. By contrast, the exoskeleton carries substantially higher stress, increasing from approximately 224 MPa to 448 MPa during pressurization (Table 4.4). Overall, the semi-rigid architecture primarily *redistributes* pressurization loads from the bladder into the structural frame rather than increasing membrane stress.

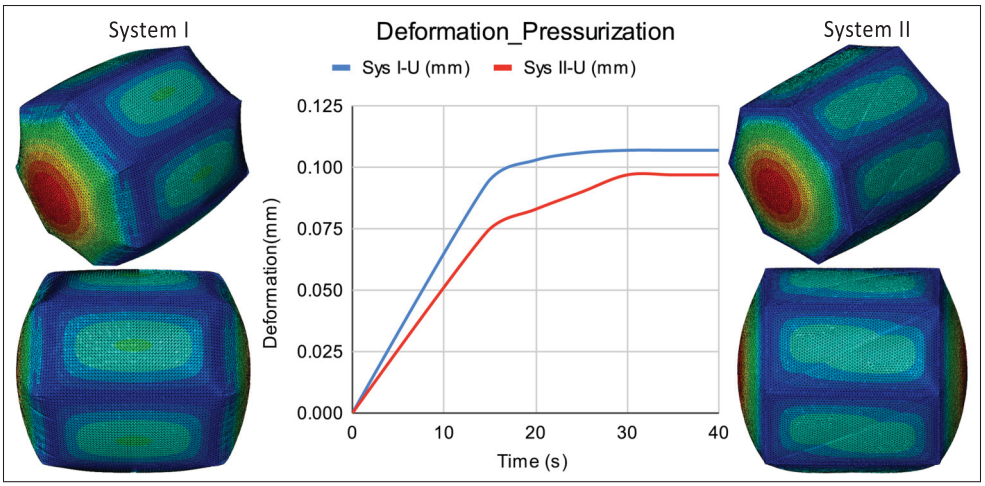

Figure 4.12 Maximum displacement magnitude at the pressurization equilibrium state (P = 1500 Pa) for system I and system II. The corresponding quantitative displacement values are summarized in Table 4.4.

Regarding deformation (Figure 4.12), the maximum displacement magnitude decreases from $U_{\max}$ = 10.7 cm for system I to 9.76 cm for system II. This reduction indicates that the exoskeleton limits global expansion and maintains the bladder geometry closer to the intended shape, with reduced bulging under pressurization.

Directional displacement components (U_1, U_2, U_3) further show that, in both configurations, the largest bladder motion occurs in the axial direction (U_3), typically near the end-cap regions (Figure 4.13). In system I, the unsupported bladder develops pronounced axial bulging and extensive wrinkling. In system II, the exoskeleton constrains deformation along panel edges and attachment regions, suppressing large-amplitude radial expansion and associated wrinkling; however, central portions of the end-cap surfaces remain intentionally unsupported to minimize structural mass, which explains the persistence of peak axial bladder displacement despite the overall reduction in global deformation.

Exoskeleton-only displacement fields indicate that frame deformation is primarily radial (U_1) and localized where lattice members interact with the pressurized bladder. This controlled elastic deformation is consistent with the intended role of the exoskeleton as a load-sharing

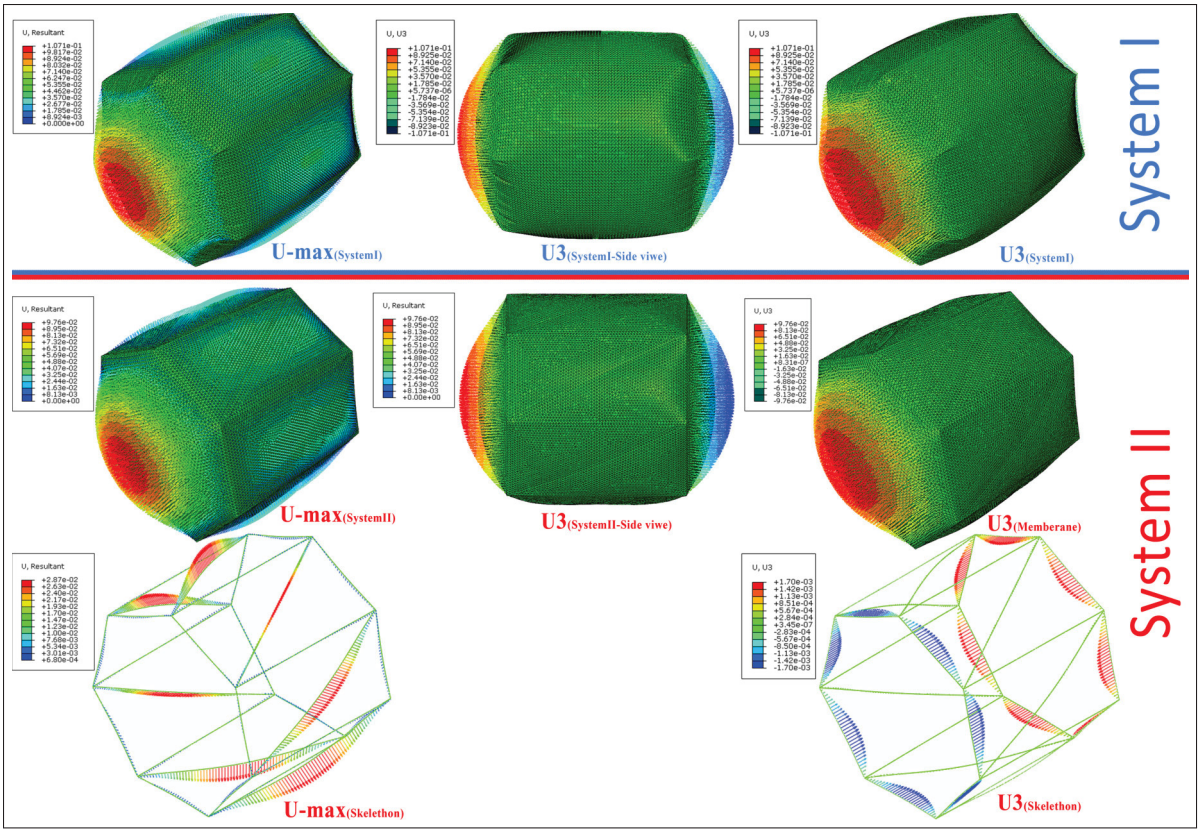

Figure 4.13 Directional displacement components at the pressurization equilibrium state (P = 1500 Pa) for system I and system II.

framework that resists outward expansion and redistributes pressurization-induced forces through its structural network.

Table 4.4 Summary of peak stress and deformation metrics during the pressurization step for system I and system II.

Metric	**System I**	**System II**		
		System	**Exoskeleton**	**Bladder**
$\sigma_{\mathrm{vM,press}}^{\max}$ (MPa)	9.40	496	496	10.4
$S_{11,\mathrm{press}}^{\max}$ (MPa)	10.7	448	448	10.4
$U_{\mathrm{max,press}}$ (m)	0.107	0.0976	0.0286	0.0976
$U_{1,\mathrm{press}}^{\max}$ (radial, m)	0.0354	0.0312	0.0279	0.0312
$U_{2,\mathrm{press}}^{\max}$ (circumferential, m)	0.0328	0.0293	0.0258	0.0293
$U_{3,\mathrm{press}}^{\max}$ (axial, m)	0.107	0.0976	0.0017	0.0976

These results highlight that exoskeleton geometry and attachment layout govern the deformation response of semi-rigid LTA bladders. In practice, the design of the reinforcing exoskeleton cannot be treated independently of the overall system architecture, since avionics placement, internal layout constraints, and mission-specific functional requirements inherently influence its geometry and connectivity. Increasing member density could further constrain axial deformation, but would increase structural mass and complexity. For SLTA platforms, this implies a fundamental trade-off between deformation control, mass efficiency, and functional integration. The selected architecture represents a compromise that stabilizes the bladder and suppresses wrinkling while preserving the ultra-lightweight character required for the intended mission. In the present work, the exoskeleton configuration was developed in conjunction with the anticipated avionics arrangement and operational objectives of the platform, resulting in a deliberately uniform and repeatable constraint pattern that provides consistent structural stabilization across the bladder.

These pressurization results, therefore, validate the use of a lightweight exoskeleton primarily as a geometric stabilizer, ensuring shape preservation and controlled deformation under nominal operating pressure. While pressurization establishes the structural role of the exoskeleton, impact resistance remains the dominant design driver for indoor SLTA operation in confined environments. On this basis, the following sections focus on low-velocity impact behavior, which represents the most critical loading scenario for evaluating bladder protection and structural robustness.

4.6.2 Stress and global deformation at impact

Low-velocity impact simulations were performed against a rigid wall using an internal pressure of 800 Pa and an initial impact velocity of 3 m/s for both configurations. The objective is to assess how structural reinforcement modifies stress transmission, global deformation, wrinkling behavior, and bladder protection during collisions representative of cluttered indoor or subterranean environments. For system II, assembly-level results are complemented by component-level fields for the bladder and the exoskeleton using dedicated display groups.

Figure 4.14 compares the evolution of von Mises stress up to the instant of maximum contact. In system I, stresses remain localized in the bladder near the impact region and geometric discontinuities, with a peak 10 MPa, accompanied by pronounced wrinkling. At the assembly level, system II exhibits higher peak stresses (179.6 MPa), which reflects activation of the exoskeleton as an additional load path rather than increased membrane demand. Component-level results show that impact loads are redirected through the exoskeleton members and discrete attachment regions, reducing the peak bladder stress to approximately 6.2 MPa and suppressing wrinkling in critical regions.

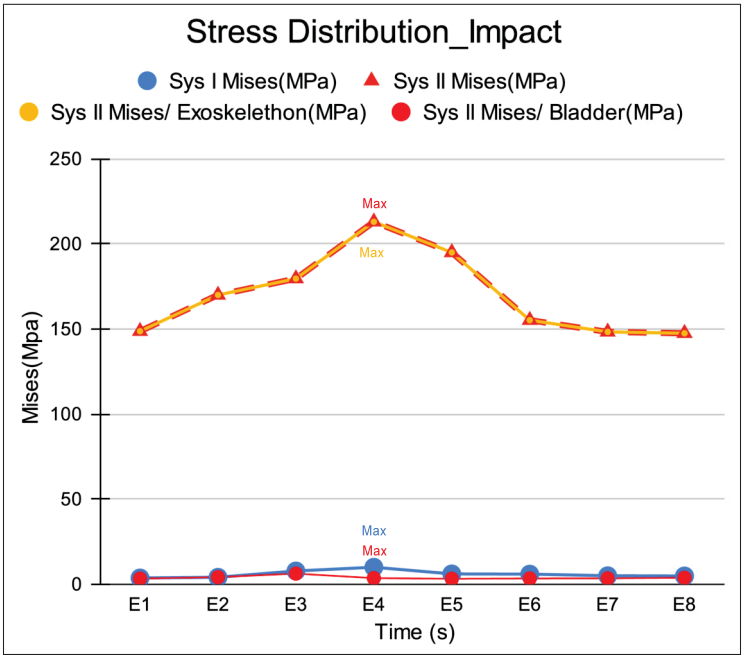

Figure 4.14 Comparison of maximum von Mises stress at impact. The plot shows stress evolution for system I, system II at the assembly level, and the bladder and exoskeleton components of system II plotted separately.

System II also limits global indentation. The peak displacement decreases from 0.022 m for system I to 0.003 m for system II, indicating a stiffer global response and reduced bladder flattening against the wall. The internal energy evolution (Figure 4.15) shows a higher peak for system II (0.59J) than for system I (0.39J), consistent with greater conversion of impact work into recoverable strain energy in the coupled semi-rigid structure under constrained deformation. Peak metrics are summarized in Table 4.5.

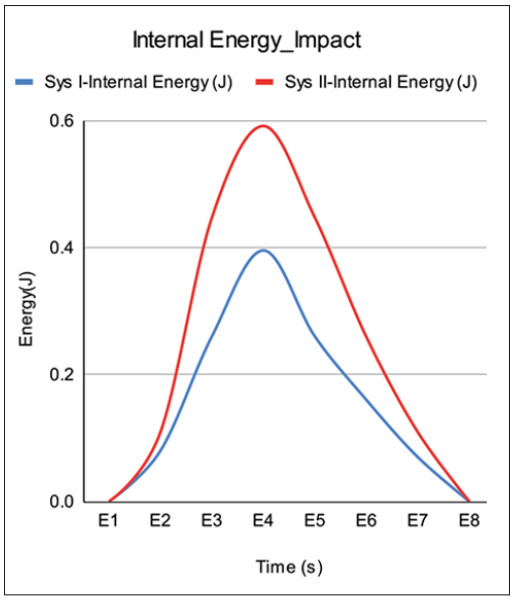

Figure 4.15 Internal energy in system I and system II at impact.

The stress levels predicted in the bladder during impact can be directly related to the experimentally measured mechanical limits of the coated LDPE membrane presented in Chapter 3. Tensile characterization showed the onset of plastic deformation at approximately 9 MPa, followed by a stable ductile regime before failure. In the non-rigid configuration (system I), peak bladder stresses during impact reach approximately 10 MPa, approaching the experimentally observed yield threshold, which indicates an increased likelihood of localized plastic deformation, thinning, or damage initiation under repeated contact events. In contrast, the semi-rigid configuration (system II) limits peak bladder stresses to approximately 6.2 MPa, which remains below the measured tensile yield stress and well below the equivalent burst stress levels observed experimentally. This stress reduction is consistent with the absence of abrupt rupture and with the ductile deformation behavior identified in material-level testing. This quantitative correspondence confirms that the numerical impact response is physically consistent with the experimentally measured stress thresholds and deformation modes of the coated LDPE membrane, and it supports the protective role of the exoskeleton in maintaining bladder stresses within a safe operating regime during low-velocity impacts.

Together, these results demonstrate a clear contrast between the two configurations. System I dissipates impact through large bladder deformation and wrinkling, at the expense of increased risk of localized damage. System II redirects a substantial fraction of the impact load into the exoskeleton, limiting bladder stress concentration, suppressing wrinkling, and preserving the overall bladder geometry.

Table 4.5 Summary of peak stress, deformation, and internal energy metrics during the impact step for system I and system II.

Metric	**System I**	**System II**		
		System	**Exoskeleton**	**Bladder**
$\sigma^{\max}_{\mathrm{vM,impact}}$ (von Mises stress, MPa)	10	179.6	179.6	6.2
$U_{\mathrm{max,impact}}$ (total, m)	0.022	0.0030	0.0033	0.0030
$E^{\max}_{\mathrm{int,impact}}$ (max. internal energy, J)	0.39	0.59	0.59	0.59

To qualitatively validate the impact modeling strategy adopted in this study, a simplified inflatable case was defined as a square Mylar (BoPET) pillow representative of a thin-film bladder component. This auxiliary case isolates the numerical methodology from the heptagonal SLTA geometry and the LDPE material model while preserving the same contact and pressurized-membrane modeling assumptions, thereby enabling an assessment of repeatability under changes in geometry and material.

The experimental specimen was a flat pillow with in-plane dimensions of 0.6×0.6 m and a uniform film thickness of $t = 25$ μm, inflated to 100 Pa to maintain a highly compliant shape. The pillow was released from an initial distance of approximately 0.5 m normal to a rigid wall and impacted at $v_0 \approx 1.5$ m/s. The impact velocity was obtained from experimental video using the Tracker analysis tool (version 6.3.1) Brown (2012); Brown, Christian & Hanson (2024).

An equivalent numerical model of the Mylar pillow was developed in Abaqus/Explicit, matching the experimental geometry, material properties, internal pressure, initial velocity, and initial distance from the rigid wall, with constitutive parameters taken from Appendix 7 and gravitational effects neglected. The simulation duration was set to 3 s, exceeding the experimentally observed interaction time of approximately 1.7 s to fully capture contact, deformation, and rebound;

differences in absolute impact timing are expected because the model prescribes a constant initial velocity and neglects air drag, launcher compliance, and other dissipative effects.

4.6.3 Impact visualization and experimental reference

A qualitative experimental–numerical comparison was performed to validate the impact modeling framework. Figure 4.16 compares the experimental impact sequence of a pressurized square Mylar (BoPET) pillow with the corresponding Abaqus/Explicit simulation. Close agreement is observed in the overall deformation mode, evolution of the contact region, and rebound behavior. In both the experiment and the simulation, the pillow undergoes the same behavior for bladder deformation upon impact, followed by localized flattening at the contact interface and gradual recovery driven by internal pressure. The consistency of these deformation mechanisms indicates that the numerical model captures the dominant physical response of thin, pressurized membranes during low-velocity collisions, supporting its applicability to the SLTA envelope impact analyses presented in this chapter.

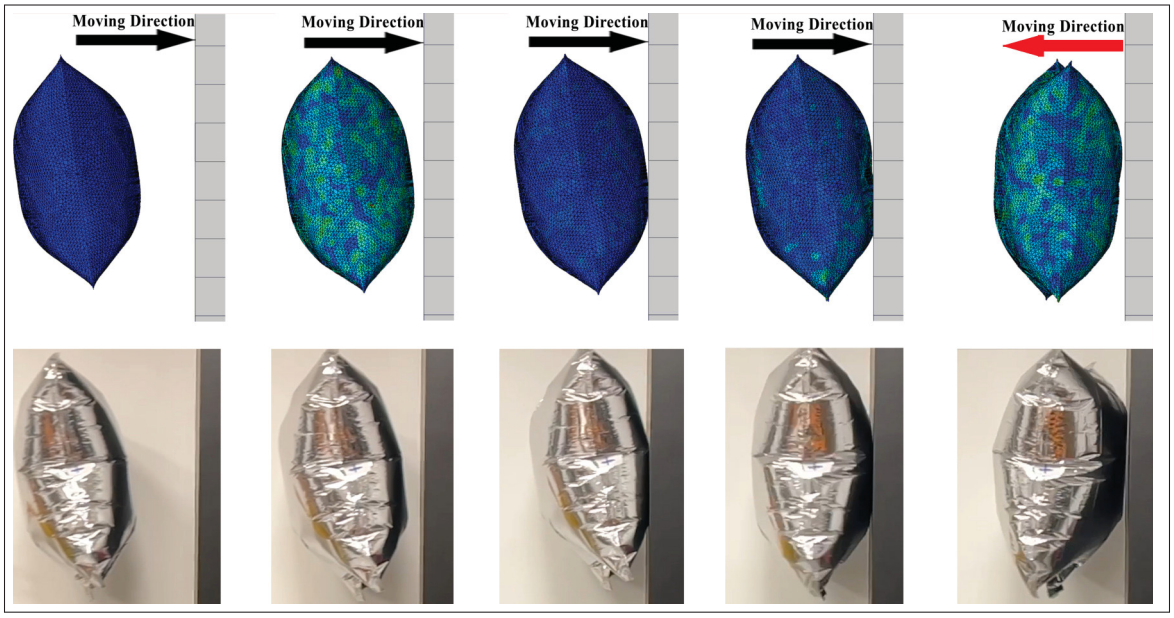

Figure 4.16 Experimental impact sequence of a pressurized Mylar pillow impacting a rigid wall, used for qualitative validation of the impact simulation methodology.

4.7 Structural behavior and operational implications for SLTA Operation

Taken together, the pressurization and impact simulations reveal a clear structural trade-off between the two configurations. The non-rigid airship (system I) behaves as a highly compliant energy absorber: impact energy is primarily dissipated through large bladder deformation, resulting in greater global indentation, localized stress concentrations, and pronounced wrinkling during both pressurization and collision events. While this compliance reduces peak reaction forces, it also exposes the thin bladder to direct contact with obstacles, large cyclic strains, and concentrated loading along seams and geometric discontinuities, increasing the risk of fatigue damage or tearing under repeated impacts.

By contrast, the semi-rigid configuration (system II) fundamentally alters load transmission through the introduction of a lightweight exoskeleton. Component-level analyses show that a substantial portion of the contact force is redirected through the frame and its attachment regions, such that the rigid wall interacts primarily with the exoskeleton rather than directly with the bladder. This shielding effect limits indentation, stabilizes the global geometry, and markedly suppresses severe wrinkling, particularly near corners and edges where stress concentrations are most critical in system I. The higher peak stresses observed at the assembly level, therefore, reflect a stiffer and more controlled load path, rather than degraded structural performance; within the range of loads and geometries considered, these stresses remain acceptable according to the adopted material models.

These structural behaviors have direct operational implications for indoor SLTA missions, where unpredictable contacts are difficult to avoid. In such contexts, the compliant response of system I provides energy absorption but at the expense of bladder durability and geometric stability. System II preserves the advantages of buoyant flight while significantly enhancing impact tolerance. The frame maintains hull shape under pressure variations, mitigates wrinkle formation, and provides an additional protective barrier against collisions with walls, ceilings, or obstacles. Improved geometric stability is particularly beneficial for controllability, sensor alignment, and repeated operation in constrained spaces.

From a design perspective, these results support the adoption of a semi-rigid architecture as a preferred baseline for ultra-light indoor airships. A thin, optimized bladder, such as the VELUM bladder presented in Chapter 3, can be effectively reinforced by a lightweight exoskeleton tuned to the expected impact severity and allowable mass budget. Exoskeleton topology, attachment layout, and local reinforcement near critical contact regions should be co-designed with bladder material properties to balance three competing objectives: limiting peak bladder strain and wrinkling, maintaining global shape for controllability, and preserving sufficient compliance to avoid excessive load transmission to onboard components. By quantifying these trade-offs, the present FEM analysis provides a rational basis for the semi-rigid SLTA configuration adopted in this work.

CONCLUSION AND RECOMMENDATIONS

This thesis investigated the design, fabrication, and structural evaluation of ultra-light indoor LTA systems intended for operation in confined and obstacle-rich environments such as caves, tunnels, and industrial interiors. The work addressed two key challenges limiting the deployment of SLTA in such settings: (i) the need for a lightweight bladder with sufficient mechanical robustness and low gas permeability to enable sustained operation, and (ii) the vulnerability of thin bladder material to excessive deformation and damage under pressurization and impact. To address these challenges, the research combined material development, experimental characterization, and explicit finite element analysis to propose and evaluate a semi-rigid structural concept for safer and more reliable indoor LTA operation.

In the first stage, a systematic assessment of commercially available polymer films highlighted the limitations of commonly used materials such as polyurethane and Mylar for indoor buoyant vehicles. These materials were found to be unable to simultaneously satisfy the stringent requirements of low surface density, flexibility, tear resistance, and helium retention imposed by small buoyant volumes. To overcome these limitations, a coated LDPE bladder material was developed and experimentally characterized. The results demonstrated that the proposed bladder achieves a favorable balance between mechanical durability and gas-barrier performance while maintaining an exceptionally low mass, making it well-suited for ultra-light indoor airships. This material development, formalized under the VELUM concept (Chapter 3), constitutes a central contribution of this work and led to a patent application.

In the second stage, the structural behavior of an indoor SLTA was investigated using an explicit dynamic finite element framework implemented in Abaqus/CAE 2024. Simulations were performed on a modular heptagonal geometry representative of an underground exploration platform and considered two configurations: a purely inflatable non-rigid system (system I) and a semi-rigid system (system II) reinforced by a lightweight carbon exoskeleton. Under

internal pressurization, the numerical results showed good agreement with analytical thin-shell stress estimates. Under impact loading, the semi-rigid configuration significantly reduced global deformation, suppressed severe wrinkling, and redirected contact loads away from the bladder, at the expense of localized stress concentrations near attachment regions that remained within acceptable limits. These results confirm that a carefully designed exoskeleton can act as a protective load-bearing cage, improving geometric stability and mitigating damage risk in cluttered indoor environments.

Beyond cave exploration, the semi-rigid indoor airship architecture developed in this thesis provides a versatile platform applicable to a broad range of indoor missions. By combining an optimized thin-film bladder with distributed structural reinforcement, the proposed concept reconciles minimal mass, collision tolerance, and shape preservation. Potential applications include industrial inspection in large tanks or warehouses, monitoring of cultural heritage sites, deployment of long-duration indoor sensing networks, and operation in sensitive or human-occupied environments where high endurance, low disturbance, soft contact, and safety are critical. Future work may therefore focus on mission-specific geometric variants, payload integration strategies, and the co-design of control and navigation algorithms tailored to the dynamics and impact resilience of semi-rigid SLTA vehicles. More broadly, this work contributes to expanding the role of buoyant systems as a safe and energy-efficient alternative to multicopter drones for operation in constrained and hazardous environments.

Recommendations

Based on the results obtained in this thesis, several directions are recommended to further advance the structural understanding and practical deployment of ultra-light indoor LTA systems.

First, future work should extend the present envelope-level analyses toward a full-body structural model of the complete airship. While detailed flight dynamics are not required, a three-dimensional finite element model of the assembled system, including the coated LDPE envelope, carbon exoskeleton, 3D-printed joints, integrated dampers, and interfaces with the gondola and propulsion units, would enable a more comprehensive assessment of global stiffness, load paths, and stress concentrations at structural connections. Such a model would also allow evaluation of local impact absorbers and their effectiveness in protecting both the bladder and critical onboard components during collisions in cluttered environments.

Second, further investigation of the lifting gas and its interaction with the VELUM bladder is recommended, with particular attention to hydrogen as an alternative to helium. Given the rising cost and limited availability of helium, hydrogen represents a compelling option for long-duration or repeated missions. Future studies should therefore assess the permeability, mechanical response, ageing behaviour, and seam integrity of the coated LDPE bladder when exposed to hydrogen. This material investigation must be accompanied by a rigorous safety analysis tailored to indoor and subterranean operation, including acceptable pressure levels, ventilation, and leak-detection strategies, risk mitigation measures, and safe failure modes.

Third, dedicated experimental campaigns should be conducted to evaluate the long-term structural reliability of the semi-rigid architecture under realistic mission conditions. These should include fatigue testing of the coated bladder under repeated pressurization cycles, durability assessment of welded or bonded seams, and evaluation of the residual stiffness and energy-absorption capacity of 3D-printed joints and dampers after multiple impacts. Coupling such experiments

with refined numerical models incorporating simplified damage or fracture criteria would support the identification of critical regions, the definition of appropriate safety factors, and the development of design guidelines for future generations of semi-rigid indoor airships. In parallel, the structural framework developed in this work could be adapted to alternative geometries and exoskeleton layouts optimized for different mission profiles, such as industrial inspection or heritage monitoring.

Finally, the industrialization and automation of the bladder manufacturing process should be pursued. In the present work, cutting, coating, and joining operations were largely manual, which was appropriate for exploratory development but introduced variability in coating thickness, seam quality, alignment, and tightness. Future efforts should investigate controlled coating techniques combined with automated sewing or sealing processes tailored to thin coated films. Such developments would improve repeatability, strengthen joints, reduce production time, and facilitate the transition from single prototypes to small-series manufacturing of ultra-light indoor airship bladders.

APPENDIX I

FACILITIES

1. Experimental and characterization facilities

This appendix summarizes the experimental facilities, laboratories, and equipment used for material characterization and prototype testing in this study.

Table-A I-1 Experimental and characterization facilities used in this study.

Activity	**Equipment / facility**	**Institution**
Sample coating	Ventilated chemical coating bench (ducted fume hood)	ÉTS
Big-scale coating	Dedicated painting room equipped with ventilation	ÉTS
Film cutting and specimen preparation	Laser cutting (Kongsberg X24 Edge)	ÉTS
Tensile testing	MTS Alliance RF/200 machine	ÉTS
Puncture testing	MTS Alliance RF/200 machine	ÉTS
Tear testing	MTS Alliance RF/200 machine	ÉTS
Surface morphology observation	VHX-7000 digital microscope	ÉTS
Thin-film density measurements	Helium pycnometer	Polytechnique Montréal
Thickness Measurements	Micrometer, Micromeritics/Folio Instruments, AccuPyc 1340	Welding lab–ÉTS
Laser cutting of Plexiglas components	Laser cutter for acrylic and polymer sheets	FabLab–ÉTS
Isolated room for the gas barrier test	Laser cutter for acrylic and polymer sheets	ÉTS
Leakage testing	Enclosed, non-ventilated test room	ÉTS
Wettability	VCA Optima Video Contact Angle System	ÉTS
Melt flow characterization (MFI)–polymer rheological properties	KAYJAY/2006/AC	ÉTS

APPENDIX II

ABAQUS MODELING DETAILS

1. Explicit Time Integration Formulation

In Abaqus/Explicit, the structural response is computed using an explicit central-difference time integration scheme. At each time increment, the dynamic equilibrium is expressed as

$$\mathbf{M}\ddot{\mathbf{u}}_t = \mathbf{P}_t^{\text{ext}} - \mathbf{P}_t^{\text{int}}, \tag{A II-1}$$

where $\mathbf{M}$ is the mass matrix, $\ddot{\mathbf{u}}_t$ is the nodal acceleration vector, and $\mathbf{P}_t^{\text{ext}}$ and $\mathbf{P}_t^{\text{int}}$ denote the external and internal force vectors, respectively. In the present analyses, the time increment was determined automatically based on the stability criterion, resulting in a variable time-step formulation consistent with prior studies on inflatable structures (Pecora, 2017).

Nodal velocities and displacements are updated according to

$$\dot{\mathbf{u}}_{t+\frac{\Delta t}{2}} = \dot{\mathbf{u}}_{t-\frac{\Delta t}{2}} + \left(\frac{\Delta t_{(t+\Delta t)} + \Delta t_{(t)}}{2}\right)\ddot{\mathbf{u}}_t, \tag{A II-2}$$

$$\mathbf{u}_{t+\Delta t} = \mathbf{u}_t + \Delta t_{(t+\Delta t)}\,\dot{\mathbf{u}}_{t+\frac{\Delta t}{2}}, \tag{A II-3}$$

allowing the membrane system to evolve dynamically toward equilibrium through successive small time increments.

2. Membrane normal orientation and fluid cavity assignment

In Abaqus, membrane and shell elements possess two distinct faces, denoted as the SPOS (positive normal) and SNEG (negative normal) sides(Figure II-1). Correct assignment of these faces is essential for the application of internal pressure loads and for defining contact interactions. In the present work, the SNEG face of the bladder was consistently assigned to the internal fluid cavity, while the SPOS face was exposed for interaction with rigid obstacles. This

convention ensures physically consistent pressure loading and contact response during inflation and impact simulations (Dassault Systèmes Simulia Corp., 2024).

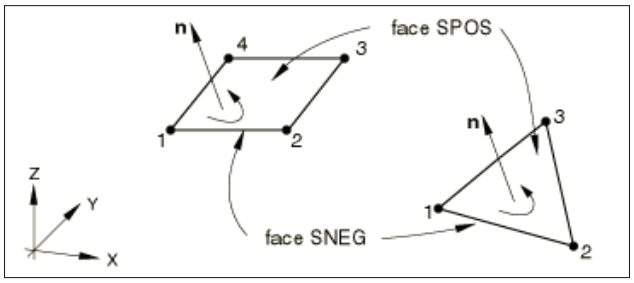

Figure-A II-1 Normal orientation for bladder elements in Abaqus: SPOS and SNEG faces used for defining fluid cavity and contact interactions.(Dassault Systèmes Simulia Corp., 2024)[web:22]

3. Beam orientation and exoskeleton section definition

The exoskeleton was modeled using beam elements with circular thin-walled pipe sections. Proper beam orientation was ensured by defining tangent vectors along each beam axis, allowing accurate representation of bending and torsional behavior. Section properties were assigned uniformly across the exoskeleton network to match the fabricated carbon tube geometry. These modeling choices follow standard Abaqus recommendations for slender structural members (Dassault Systèmes Simulia Corp., 2024).

4. Rigid body definition and meshing strategy

Rigid obstacles were implemented as discrete rigid surfaces composed of R3D3 triangular elements. Each rigid surface was associated with a reference point (RP) controlling its motion and boundary conditions. Local mesh refinement was applied in regions expected to experience contact with the inflatable envelope, while coarser discretization was used elsewhere to reduce computational cost. This approach ensures accurate contact resolution while maintaining numerical efficiency.

5. Mass Scaling

Despite its strengths, the explicit method requires extremely small time increments to maintain numerical stability, especially in models with fine meshes or high stiffness. The critical time increment (Δt_{crit}) is governed by the stability criterion: (Dassault Systèmes Simulia Corp., 2024).

$$\Delta t_{\text{crit}} \approx \frac{L_{\text{min}}}{c_d} \tag{A II-4}$$

where L_{min} is the smallest element length and c_d is the dilatational wave speed of the material, given by: (Dassault Systèmes Simulia Corp., 2024).

$$c_d = \sqrt{\frac{\lambda + 2\mu}{\rho}} \tag{A II-5}$$

with λ and μ being the Lamé constants and ρ the material density.

When thin structural elements such as membranes are used, L_{min} can become very small, causing the stable time increment to fall below practical simulation times. To alleviate this limitation and simulate slowly evolving structural responses (quasi-static behavior), mass scaling is employed. This technique artificially increases the material density to raise the stable time increment, allowing the simulation to advance more quickly while maintaining numerical stability.

The core principle of mass scaling lies in the dependency of the stable time increment on wave speed and element size. Since wave speed c_d is inversely proportional to the square root of material density ρ:

$$c_d \propto \sqrt{\frac{1}{\rho}} \Rightarrow \Delta t \propto \sqrt{\rho} \tag{A II-6}$$

Increasing the density by a factor of f^2 increases the stable time increment by a factor of f, significantly reducing the computational cost. However, as noted in (Pecora, 2017), mass scaling must be used carefully. Overuse can introduce artificial inertial effects, distorting the physical behavior of the system. It is especially important in quasi-static simulations that the ratio of kinetic energy to internal energy remains low throughout the analysis. A common rule of thumb

is to ensure: (Dassault Systèmes Simulia Corp., 2024)

$$\frac{\text{Kinetic Energy}}{\text{Internal Energy}} < 5\% \tag{A II-7}$$

In this work, a fixed mass scaling strategy was adopted, where the entire model was assigned an increased density factor at the beginning of the simulation step. This allowed for reduced computational time without compromising the accuracy of results. Care was taken to monitor inertial forces and verify that the structure reached a quasi-static equilibrium, satisfying the typical threshold for quasi-static explicit analysis Dassault Systèmes Simulia Corp. (2024)

Table-A II-1 Effects of Mass Scaling on Simulation Features (Dassault Systèmes Simulia Corp., 2024)

Simulation Feature	**Affected by Mass Scaling**
Element mass and rotary inertia (beams, shells)	Yes
Bulk viscosity and mass proportional damping	Yes
Infinite elements	Yes
Gravity loads	No
Thermal heat transfer / conduction	No
Fully coupled thermal-stress simulations	No
Fluid, acoustic, and link elements	No
Spring and dashpot elements	No

This approach, as demonstrated in (Pecora, 2017), has proven efficient for simulating large-scale confined inflatable structures and remains widely accepted in studies where small time steps arise from fine mesh resolution rather than transient excitation.

6. Stress Calculation Details

The following values were used for the analytical stress calculation on thin Inflatable Shell at Pressurized step: $P = 1500$ Pa (applied internal pressure), $R_{\text{cyl}} = 0.342$ m (radius of the cylindrical midsection), $R_{\text{cap}} = 0.610$ m (hemispherical cap radius), and $t = 5 \times 10^{-5}$ m (bladder thickness). This approach assumes a thin-wall approximation and uniform pressure loading. The maximum hoop stress for a cylindrical bladder under pressure P is:

$$\sigma_{\text{cyl}} = \frac{PR_{\text{cyl}}}{t}$$

For hemispherical caps, the corresponding bladder stress is:

$$\sigma_{\text{cap}} = \frac{PR_{\text{cap}}}{2t}$$

Summing the contribution from the cylindrical section and the two hemispherical end caps gives:

$$\sigma_{\text{max}} = \frac{P}{t}(R_{\text{cyl}} + R_{\text{cap}})$$

Plugging in the given values:

$$\sigma_{\text{max}} = \frac{1500}{5 \times 10^{-5}}(0.342 + 0.610) \approx 28.56 \text{ MPa}$$

For LDPE properties (elastic limit, yield, fracture values), see Table 4.2 in the main text.

7. Mylar pillow properties for impact validation

This appendix summarizes the material, geometric, and loading parameters used to model the Mylar (BoPET) pillow employed in the impact validation study described in Section 4.6.3. The mechanical properties are based on published data for biaxially oriented PET films and metallized Mylar foils, complemented by values estimated to match the range of tensile strength and stiffness reported in the literature.(Holenstein *et al.*, 2010; González, 2004)

Table-A II-2 Mechanical properties of Mylar (BoPET) used in the impact validation model.

Property	**Value**	**Unit**
Density	1478	kg/m^3
Young's Modulus	4.1×10^9	Pa
Poisson's Ratio	0.38	–
Yield Stress	2.3×10^7	Pa
Plastic Strain at Yield	0.0	–
Fracture Strain	0.05	–
Stress Triaxiality	−0.33	–
Fracture Energy	0.7	J/m^2
Damage Evolution	Linear (energy-based)	–

Table-A II-3 Geometric and loading parameters of the Mylar pillow used for impact validation.

Parameter	**Value**	**Unit**
Pillow Length	0.60	m
Pillow Width	0.60	m
Bladder Thickness	2.5×10^{-5}	m
Internal Pressure (overpressure)	100	Pa
Initial Distance to Wall	0.50	m
Initial Impact Velocity	1.5	m/s
Simulation Duration	3.0	s
Experimental Interaction Time	≈ 1.7	s

BIBLIOGRAPHY

Adeel, Shoeb and Suvarna, Sohan. (2017). Design and Development of an Easily Deployable Indoor Finless Airship. *International Conference on Advances in Robotics, Mechanical Engineering and Automation*, 1–6.

Adorno-Rodríguez, R. (2014). *Nonlinear Structural Analysis of an Icosahedron and Its Application to Lighter-than-Air Vehicles under a Vacuum*. (Master's Thesis, Air Force Institute of Technology (AFIT), Wright-Patterson Air Force Base, Ohio, USA). Retrieved from: Accessed: 2025-10-08.

Aerospace/LTAS, W. (2025). Lenticular, toroidal, variable geometry airships. Retrieved from: TechnicalReport,Lynceans.org.

Agrawal, P. S. & et al. (2024). Advancements and challenges in drone technology: A comprehensive review. *2024 4th International Conference on Pervasive Computing and Social Networking (ICPCSN)*.

Alam, M. I. (2016). Multidisciplinary Design Optimization of Stratospheric Airship. *Proceedings of the 30th Congress of the International Council of the Aeronautical Sciences (ICAS 2016)*.

Andreasson, E., Mehmood, N. & Kao-Walter, S. (2013). Trouser tear tests of two thin polymer films. *13th International Conference on Fracture (ICF13)*.

Awasthi, S. & et al. (2023). Micro UAV swarm for industrial applications in indoor environment: a systematic literature review. *Logistics Research*, 16(1), 1–43. doi: 10.1007/s12159-023-01002-8.

Bai, J., Xiong, J. & Cheng, X. (2011). Tear resistance of orthogonal Kevlar-PWF-reinforced TPU film. *Chinese Journal of Aeronautics*, 24(1), 113-118. doi: 10.1016/S1000-9361(11)60014-9.

Bansal, G., Bhardwaj, U., Jain, N., Mulay, S. S., Sawardekar, S. & Pant, R. S. (2013). Design fabrication and flight testing of a non-rigid indoor airship. *AIAA Lighter-Than-Air Systems Technology (LTA) Conference*, 1–7. doi: 10.2514/6.2013-1297.

Bhat, S. S. et al. (2024a). Review of Autonomous Outdoor Blimps and Their Applications. Retrieved from: DroneSystemsandApplications,Vol.12,pp.1--21.

Bhat, S. S. et al. (2024b). Review of Autonomous Outdoor Blimps and Their Applications. *Drone Systems and Applications*, 12, 1–21. doi: N/A.

Biju, M. & Pant, R. S. (2017). Design and development of an indoor autonomous airship. *AIAA Lighter-Than-Air Systems Technology Conference Proceedings*, 2017(1), 1–8. doi: 10.2514/6.2017-3996.

Blanchard, A., Gouanvé, F. & Espuche, E. (2017). Effect of humidity on mechanical, thermal and barrier properties of EVOH films. *Journal of Membrane Science*, 540, 1–9. doi: 10.1016/j.memsci.2017.06.031.

Bonet, J., Wood, R., Mahaney, J. & Heywood, P. (2000). Finite Element Analysis of Air Supported Membrane Structures. *Engineering Structures*, 22(7), 660–668. doi: 10.1016/S0141-0296(99)00051-6.

Brown, D. (2012). Tracker Free Video Analysis and Modeling Tool. Retrieved from: Computerprogram.

Brown, D., Christian, W. & Hanson, R. [Version 6.3.1]. (2024). Tracker Video Analysis and Modeling Tool.

Bruyneel, M., Delsemme, J., Gort, P. et al. (2019). Design and sizing of an airship supported by CAE. *Proceedings of the NAFEMS World Congress*.

Burri, M. et al. (2013). Design and Control of a Spherical Omnidirectional Blimp. Retrieved from: Proceedingsofthe2013IEEE/RSJInternationalConferenceonIntelligentRobotsandSystems(IROS).

Catar, L., Tabiai, I. & St-Onge, D. (2024). CAVERNAUTE: A Design and Manufacturing Pipeline of a Rigid but Foldable Indoor Airship Aerial System for Cave Exploration. *arXiv preprint arXiv:2409.07591*, 1–36. doi: 10.48550/arXiv.2409.07591.

Chen, Y., Yang, W., Xie, W., Wang, X. & Fu, G. (2022). Meso-Scale tearing mechanism analysis of flexible fabric composite for stratospheric airship via experiment and numerical simulation. *Journal of Shanghai Jiaotong University (Science)*, 27(6), 873–884. doi: 10.1007/s12204-022-2431-8.

Cheng, C. [Master's thesis, KTH Royal Institute of Technology. Accessed on October 2, 2025]. (2024). Exploring alternative Functional Thin Layers (FTL's) for high tear packaging applications.

Chouhan, S., Ghosh, S., Butola, B. S. & Joshi, M. (2024). Studies of high-performance fabric-based laminated hull material for stratospheric airship. *Journal of Reinforced Plastics and Composites*, 43(17-18), 1008–1023. doi: 10.1177/07316844231198301.

Collins, S. et al. (1999). The thermal stability of some vinylidene chloride copolymers. *Polymer Degradation and Stability*, 66(1), 87–94. doi: 10.1016/S0141-3910(99)00056-7.

Cranston, B. C. (2016). *Conceptual design, structural analysis, and design space exploration of a vacuum lighter than air vehicle*. (Master's thesis, University of Maryland, College Park).

Dai, W., Zhang, M. & Low, K. H. (2024). Data-Efficient Modeling for Power Consumption Estimation of Quadrotor Operations Using Ensemble Learning. Retrieved from: AerospaceScienceandTechnology,Vol.144,Article108791.

Dai, Z. et al. (2021). Helium Separation Using Membrane Technology: Recent Advances and Perspectives. Retrieved from: SeparationandPurificationTechnology,Vol.274, Article119044.

Dassault Systèmes Simulia Corp. (2024). Abaqus Documentation 2024.

Dhawan, A. & Jindal, P. (2021). A review on use of polyurethane in lighter-than-air systems. *Materials Today: Proceedings*, 43, 746-752. doi: 10.1016/j.matpr.2020.12.962.

Eissing, C. S., Richter, A. & Schlipf, D. (2022). CPACS LTA—Using Common Data Structures for Visualization and Optimization of Airship Designs. *Lighter Than Air Systems: Proceedings of the International Conference on Design and Engineering of Lighter-Than-Air Systems 2022 (DELTAs-2022)*, pp. 25–37. doi: 10.1007/978-981-99-1659-1_3.

Emimi, M., Khaleel, M. & Alkrash, A. (2023). The current opportunities and challenges in drone technology. *International Journal of Electrical Engineering and Sustainable Development*, 10(2), 74–89. doi: 10.34104/ijeasd.023.074089.

Escobar, L. & Pereira, G. A. S. (2025). Energy-Aware Coverage Path Planner for Multirotor UAVs. *2025 International Conference on Unmanned Aircraft Systems (ICUAS)*.

Faye, M. [Accessed on October 2, 2025]. (2015). Un cube flottant dans la Verna: histoire d'une singulière grotte.

Feinerman, A., Sabatino, D. R., Ma, M., Lynch, T. & Tavana, H. (2022). A novel rigidizable inflatable lunar habitation system: Design concept and material characterization. *Acta Astronautica*, 196, 12–22. doi: 10.1016/j.actaastro.2022.03.007.

Gao, W., Zhang, J., Ma, T., Lin, G., Liu, Y., Wang, C. & Tan, H. (2023). A novel inflatable rings supported design and buoyancy-weight balance deformation analysis of stratosphere airships. *Aerospace Science and Technology*, 138, 108232. doi: 10.1016/j.ast.2023.108232.

Gawale, A., Raina, A., Pant, R. & Jahagirdar, Y. (2009). Design, fabrication and operation of remotely controlled airships in India. *18th AIAA Lighter-Than-Air Systems Technology Conference*, pp. 2855. doi: 10.2514/6.2009-2855.

González, G. J. [Academic thesis]. (2004). Design of a Compact, Lightweight, and Low-Cost Solar Concentrator. Retrieved from: MasterâĂŹsThesis, MassachusettsInstituteofTechnology.

Gordoniz, J. E. S., Saad, M. & St-Onge, D. [ASME Journal publication]. (2025). Simple Tuning for an Adaptive and Model-Free Control of Indoor Airships. Retrieved from: JournalofComputationalandNonlinearDynamics,Vol.20,No.8, Article081012.

Gorjup, G. & Liarokapis, M. (2020). A low-cost, open-source, robotic airship for education and research. *IEEE Access*, 8(1), 70713–70721. doi: 10.1109/ACCESS.2020.2986772.

Hall, J. L., Jones, J. A., Clark, B., Cutts, J. A., Young, R. E. & Crisp, D. (2008). Prototype design and testing of a Venus long duration, high altitude balloon. *Advances in Space Research*, 42(10), 1648–1655. doi: 10.1016/j.asr.2007.03.017.

Hall, J. L., Jones, J. A., Clark, B., Cutts, J. A., Young, R. E. & Crisp, D. (2009). Second generation prototype design and testing for a high altitude Venus balloon. *Advances in Space Research*, 44(1), 93-105. doi: 10.1016/j.asr.2008.10.033.

Hamm, K., Imtiaz, K. S. & Raju, I. S. (2021). Some Remaining Challenges in Aerospace Structures. *AIAA SciTech 2021 Forum*.

Harrison, D. [Accessed October 2025]. (2023). *Lighter-than-Air Flight*. Introduction to Aerospace Flight Vehicles. Embry–Riddle Aeronautical University Scholarly Commons. Retrieved from: https://eaglepubs.erau.edu/introductiontoaerospaceflightvehicles/chapter/lth/.

Hasan, M. [Doctoral thesis]. (2021). Novel Efficient Wing Buoyant Aircraft Design for Enhanced Aerodynamic Performance. Retrieved from: PhDDissertation,UniversityofSheffield.

Havill, C. D. (1974). *Some factors affecting the use of lighter than air systems* (Report n°NASA-TM-X-62374).

Holenstein, B. D. et al. [Book chapter]. (2010). Experiments with Pneumatically-Formed Metalized Polyester Mirrors. Retrieved from: In:LightweightAlt-AzimuthTelescopeDevelopments,CollinsFoundationPress,SantaMargarita,pp.381--394.

Huang, X., Tepylo, N., Pommier-Budinger, V., Budinger, M., Bonaccurso, E., Villedieu, P. & Bennani, L. (2019a). A survey of icephobic coatings and their potential use in a hybrid coating/active ice protection system for aerospace applications. *Progress in Aerospace Sciences*, 105, 74–97. doi: 10.1016/j.paerosci.2019.01.002.

Huang, Y.-W., Alonso-Mora, J. & Paull, L. (2019b). Duckiefloat: A Collision-Tolerant Resource-Constrained Blimp for Long-Term Autonomy in Subterranean Environments. *arXiv preprint arXiv:1910.14275*, 1–7. doi: 10.48550/arXiv.1910.14275.

Hunt, J. D. (1982). Structural Analysis of Aerostat Flexible Structure by the Finite-Element Method. Retrieved from: JournalofAircraft,Vol.19,No.8,pp.674--678.

International, A. [Accessed on October 2, 2025]. (2021a). ASTM-D1004-21:Standard Test Method for Tear Resistance of Plastic Film and Sheeting.

International, A. [Accessed on October 2, 2025]. (2021b). ASTM F1306-21: Standard test method for slow rate penetration resistance of flexible barrier films and laminates.

International, A. [Accessed on October 2, 2025]. (2021c). ASTM F88/F88M-21: Standard Test Method for Seal Strength of Flexible Barrier Materials.

International, A. [Accessed on October 2, 2025]. (2023). ASTM D1238-23a: Standard Test Method for Melt Flow Rates of Thermoplastics by Extrusion Plastometer.

International, P. (2024). LDPE (Low-Density Polyethylene). Retrieved from: TechnicalMaterialDataSheet.

Joshi, M., Adak, B. & Butola, B. S. (2018). Polyurethane nanocomposite based gas barrier films, membranes and coatings: A review on synthesis, characterization and potential applications. *Progress in Materials Science*, 97, 230-282. doi: 10.1016/j.pmatsci.2018.05.001.

Joshi, M., Chatterjee, U., Adak, B., Tiwari, R., Mandlekar, N., Chouhan, S. & Butola, B. S. (2024). A critical review on the development and technology of aerostat and airship hull material. *The Journal of The Textile Institute*, 1-16. doi: 10.1080/00405000.2024.2343123.

Kaci, M. et al. (2005). Waste and Virgin LDPE/PET Blends Compatibilized with an Ethylene–Butyl Acrylate–Glycidyl Methacrylate (EBAGMA) Terpolymer. Retrieved from: MacromolecularMaterialsandEngineering,Vol.290,No.10,pp.987--995.

Kong, J.-S., Lee, D.-J. & Kim, H.-D. (2001). Surface modification of low-density polyethylene (LDPE) film and improvement of adhesion between evaporated copper metal film and LDPE. *Journal of Applied Polymer Science*, 82(7), 1677-1690. doi: 10.1002/app.2008.

Kordos, A. et al. (2024). The Problem of Recycling of Unmanned Aerial Vehicles. Retrieved from: AdvancesinScienceandTechnology.ResearchJournal,Vol.18,No.7.

Li, A., Vallabh, R., Bradford, P. D., Kim, D. & Seyam, A. F. (2022a). Development of hull material for high-altitude airship: A parametric study. *Journal of Reinforced Plastics and Composites*, 41(11-12), 444-458. doi: 10.1177/07316844211054852.

Li, A., Vallabh, R., Bradford, P. D., Kim, D. & Seyam, A. F. (2022b). Development of hull material for high-altitude airship: A parametric study. *Journal of Reinforced Plastics and Composites*, 41(11-12), 444-458. doi: 10.1177/07316844211054852.

Li, S., Chen, L., Song, Y., Mi, X., Chen, W. & Zhao, H. (2022c). Pressure-bearing performance of sliding poly-*p*-phenylene benzobisoxazole-rope-reinforced spherical composite envelope structures. *Thin-Walled Structures*, 180, 109929. doi: 10.1016/j.tws.2022.109929.

Li, S., Chen, W., Chen, L., Song, Y., Hu, J., Zhao, H. & Zhang, D. (2024). Experimental study and refined numerical simulation of ultimate pressure-bearing performance of rope-reinforced airship envelope structures. *Advances in Structural Engineering*, 27(7), 1266–1282. doi: 10.1177/13694332241246376.

Liao, L. & Pasternak, I. (2009). A review of airship structural research and development. *Progress in Aerospace Sciences*, 45(4-5), 83–96. doi: 10.1016/j.paerosci.2009.01.001.

Liu, Z., Zhang, Y., Wang, H. et al. (2025). Advancements in airship design and construction: a comprehensive review of structure, propulsion, and aerodynamics. *Proceedings of the Third International Conference on Advanced Materials and Equipment Manufacturing (AMEM 2024)*, 13691, 1–18. doi: 10.1117/12.3014820.

Lobner, P. (2024a). Modern Airships – Part 2, Revision 6. Retrieved from: TechnicalReport, LynceansInitiative.

Lobner, P. (2024b). Modern Airships – Part 2. Retrieved from: TechnicalReport, LynceansInitiative.

Lopes, C. M. A. & Felisberti, M. I. (2006). Composite of Low-Density Polyethylene and Aluminum Obtained from the Recycling of Postconsumer Aseptic Packaging. Retrieved from: JournalofAppliedPolymerScience,Vol.101,No.5,pp.3183--3191.

Lv, J. et al. (2022). Study of Performance of Aerostat Envelope Materials on the Coast. Retrieved from: FrontiersinMaterials,Vol.9,Article992984.

Maekawa, S., Shibasaki, K., Kurose, T., Maeda, T., Sasaki, Y. & Yoshino, T. (2008). Tear propagation of a high-performance airship envelope material. *Journal of Aircraft*, 45(5), 1546-1553. doi: 10.2514/1.32264.

Maity, A., Majumder, S. & Ray, D. N. (2013). Amphibian Subterranean Robot for Mine Exploration. *2013 International Conference on Robotics, Biomimetics, Intelligent Computational Systems*, pp. 65–70. doi: 10.1109/ROBIONETICS.2013.6743612.

Majeed, K., Arjmandi, R. & Hassan, A. (2018). Mechanical and Oxygen Barrier Properties of LDPE/MMT/MAPE and LDPE/MMT/EVA Nanocomposite Films: A Comparison Study. *Journal of Physical Science*, 29(1), 77-88. doi: 10.21315/jps2018.29.1.4.

Mandlekar, N., Joshi, M. & Butola, B. S. (2022). A review on specialty elastomers based potential inflatable structures and applications. *Advanced Industrial and Engineering Polymer Research*, 5(1), 33–45. doi: 10.1016/j.aiepr.2021.05.004.

Manikandan, M. & Pant, R. S. (2021). Research and advancements in hybrid airships—A review. *Progress in Aerospace Sciences*, 127, 100741. doi: 10.1016/j.paerosci.2021.100741.

Martínez-Camacho, A. P. et al. (2013). Extruded Films of Blended Chitosan, Low Density Polyethylene and Ethylene Acrylic Acid. Retrieved from: CarbohydratePolymers,Vol.91, No.2,pp.666--674.

May, M. & Strohbach, T. (2025). A Review on Collisions Between Drones and Aerostructures – Experimental Studies, Numerical Simulation, and Regulation. Retrieved from: DefenceTechnology.

Mazzei, F., Teofili, L., Curti, F. & Gargiulo, C. (2023a). Mission Analysis, Dynamics and Robust Control of an Indoor Blimp in a CERN Detector Magnetic Environment. *Frontiers in Robotics and AI*, 10, 1238081. doi: 10.3389/frobt.2023.1238081.

Mazzei, F. et al. (2023b). Mission Analysis, Dynamics and Robust Control of an Indoor Blimp in a CERN Detector Magnetic Environment. Retrieved from: FrontiersinRoboticsandAI, Vol.10,Article1238081.

Melton, J. E. & Hochstetler, R. D. (2012). *Airships 101: Rediscovering the Potential of Lighter-Than-Air (LTA)* (Report n°ARC-E-DAA-TN4810).

Metlen, T. T. (2013). *Design of a lighter than air vehicle that achieves positive buoyancy in air using a vacuum*. (Master's thesis, University of Idaho).

Miller, S. H., Smith, I., Johnson, R. et al. (2014). Airships: a new horizon for science. *arXiv preprint arXiv:1402.6706*, 1–60.

Mitra, A. et al. [Available via NASA Technical Reports Server]. (2024). Enhancing Cargo Transportation by Reducing Airship Operating Costs. Retrieved from: NASATechnicalMemorandum,NASA/TM-20240012628.

Motiwala, N. I., Khan, I. A., Yelve, N. P., Narkhede, B. E. & Pant, R. S. (2013). Conceptual approach for design, fabrication and testing of indoor remotely controlled airship. *Advanced Materials Research*, 690, 3390-3395. doi: 10.4028/www.scientific.net/AMR.690-693.3390.

Mulay, S. S. & Pant, R. S. (2013). Design, fabrication and flight testing of a non-rigid indoor airship. *AIAA Lighter-Than-Air Systems Technology Conference Proceedings*, 2013(1), 1–9. doi: 10.2514/6.2013-1297.

Nguyen-Tri, P., Nguyen, T. A., Carriere, P. & Ngo Xuan, C. (2018). Nanocomposite coatings: preparation, characterization, properties, and applications. *International Journal of Corrosion*, 2018, 4749501. doi: 10.1155/2018/4749501.

Nooralishahi, P. et al. (2021). Drone-based non-destructive inspection of industrial sites: A review and case studies. *Drones*, 5(4), 106. doi: 10.3390/drones5040106.

Pahwa, R. S. et al. (2019). Dense 3D reconstruction for visual tunnel inspection using unmanned aerial vehicle. *2019 IEEE/RSJ International Conference on Intelligent Robots and Systems (IROS)*, pp. 5128–5133. doi: 10.1109/IROS40897.2019.8967577.

Palossi, D. et al. (2019). Extending the Lifetime of Nano-Blimps via Dynamic Motor Control. Retrieved from: JournalofSignalProcessingSystems,Vol.91,No.3,pp.339--361.

Pant, R. S. (2014). Design, fabrication and flight demonstration of a remotely controlled airship for snow scientists. *Journal of Aerospace Technology and Management*, 6(1), 19–27. doi: 10.5028/jatm.v6i1.313.

Pecora, I. (2017). *Finite Element Simulation of Large-Scale Confined Inflatable Structures*. (Master's thesis, University of Toronto).

Prentice, B. E. & Ahmed, S. (2017). Ground-Handling Systems for Cargo Airships. *52nd Annual Meeting Proceedings: Canadian Transportation Research Forum*.

Qubaa, A. R., Hamdon, A. N. & Al Jawwadi, T. A. (2021). Morphology detection in archaeological ancient sites by using UAVs/drones data and GIS techniques. *Iraqi Journal of Science*, 62(11 (SI)), 4557–4570. doi: 10.24996/ijs.2021.62.11(SI).35.

Riboldi, C. E. D. & Rolando, A. (2023). Autonomous Flight in Hover and Near-Hover for Thrust-Controlled Unmanned Airships. Retrieved from: Drones,Vol.7,No.9,Article545.

Rozhok, A. (2023). *Modeling of Innovative Lighter-than-Air UAV for Logistics, Surveillance and Rescue Operations*. (Master's Thesis, Toulouse INP – Institut National Polytechnique de Toulouse, Toulouse, France). Retrieved from: Accessed: 2025-10-08.

Ryan, D. E. J. (2017). *The Airship's Potential for Intertheater and Intratheater Airlift* (Report n°T_RYAN_AIRSHIP_POTENTIAL). Retrieved from: https://www.airuniversity.af.edu/Portals/10/AUPress/Papers/t_ryan_airship_potential.pdf.

Ryan,D. E., J. (1992). The Airship's Potential for Intertheater and Intratheater Airlift: Eye in the Sky, Airship Surveillance. School of Advanced Airpower Studies, Air University, Maxwell Air Force Base, Alabama, 1992. Accessed on October 3, 2025.

Safandowska, M., Makarewicz, C. & Rozanski, A. (2024). Tuning Barrier Properties of Low-Density Polyethylene: Impact of Amorphous Region Nanostructure on Gas Transmission Rate. *Molecules*, 29(20), 4950. doi: 10.3390/molecules29204950.

Salas Gordoniz, J. E., Reeves, N. & St-Onge, D. (2021). Modular Foldable Airship Concept for Subterranean Exploration. *Proceedings of the ASME International Design Engineering Technical Conferences (IDETC)*, 85451, V08BT08A018-1–V08BT08A018-9. doi: 10.1115/DETC2021-69954.

Sanchis, M. R., Blanes, M., Fenollar, O., Garcia, D. & Balart, R. (2006). Surface modification of low density polyethylene (LDPE) film by low pressure O2 plasma treatment. *European Polymer Journal*, 42(7), 1558-1568. doi: 10.1016/j.eurpolymj.2006.02.001.

Sands, T. (2025). Autonomous Real-Time Mass Center Location and Inertia Identification for Grappling Space Robotics. *Technologies*, 13(4), 148. doi: 10.3390/technologies13040148.

Schwemmer, J. R., Palazotto, A. N. & Chrissis, J. (2018). Optimal design of a hexakis icosahedron vacuum-based lighter-than-air vehicle. *AIAA Journal*, 56(6), 2131–2137. doi: 10.2514/1.J056762.

Seifali Abbas-Abadi, M., Nekoomanesh Haghighi, M. & Yeganeh, H. (2012). Effect of the melt flow index and melt flow rate on the thermal degradation kinetics of commercial polyolefins. *Journal of Applied Polymer Science*, 126(5), 1739-1745. doi: 10.1002/app.36775.

Shamini, G. & Yusoh, K. (2014). Gas permeability properties of thermoplastic polyurethane modified clay nanocomposites. *International Journal of Chemical Engineering and Applications*, 5(1), 64–68. doi: 10.7763/IJCEA.2014.V5.352.

Shi, H., Geng, S. & Qian, X. (2019). Thermodynamics analysis of a stratospheric airship with hovering capability. *Applied Thermal Engineering*, 146, 600–607. doi: 10.1016/j.applthermaleng.2018.10.063.

Shi, T. et al. (2018). Investigation of Mechanical Behavior of Weld Seams of Composite Envelopes in Airship Structures. Retrieved from: CompositeStructures,Vol.201,pp.1--12.

Song, W., Li, Z., Li, Y., You, H., Qi, P., Liu, F. & Loy, D. A. (2018). Facile sol-gel coating process for anti-biofouling modification of poly (vinylidene fluoride) microfiltration membrane based on novel zwitterionic organosilica. *Journal of Membrane Science*, 550, 266–277. doi: 10.1016/j.memsci.2017.12.076.

Spearman, L. (2002). A lighter-than-air system enhanced with kinetic lift. *AIAA Aircraft Technology, Integration, and Operations (ATIO) 2002 Technical Forum*.

St-Onge, D., Reeves, N., Gosselin, C. & et al. (2017). Control, localization and human interaction with an autonomous lighter-than-air performer. *Robotics and Autonomous Systems*, 88(1), 165–186. doi: 10.1016/j.robot.2016.10.013.

Stockbridge, C., Ceruti, A. & Marzocca, P. (2012). Airship Research and Development in the Areas of Design, Structures, Dynamics and Energy Systems. Retrieved from: InternationalJournalofAeronauticalandSpaceSciences,Vol.13,No.2,pp. 170--187.

Suefuku, H., Hirayama, T., Hirakawa, Y. & Takayama, T. (2014). Torus-type airship aiming at high airworthiness quality. *Proceedings of the International Council of the Aeronautical Sciences (ICAS)*.

Taillandier, P. & Farcy, D. (2022). Lighter than air activities at ONERA: a comprehensive overview. *Proceedings of the 9th European Conference for Aerospace Sciences (EUCASS)*.

Tatham, P., Neal, C. & Wu, Y. (2017). Hybrid Cargo Airships: A Humanitarian Logistic Game Changer? Retrieved from: JournalofHumanitarianLogisticsandSupplyChainManagement, Vol.7,No.2,pp.102--125.

Themistocleous, K. (2019). The use of UAVs for cultural heritage and archaeology. In *Handbook of Research on Emerging Technologies for Digital Preservation and Information Modeling* (pp. 297–319). Springer. doi: 10.1007/978-3-030-10979-0_14.

Tiwari, M. (2024). Lighter-Than-Air Revolution: Advancements in Airship and Aerostat Materials. *International Journal of Scientific Research and Engineering Trends*, 10(3), 851–864. doi: N/A.

Troub, B., DePineuil, B. & Montalvo, C. (2017). Simulation Analysis of a Collision-Tolerant Micro-Airship Fleet. Retrieved from: InternationalJournalofMicroAirVehicles,Vol.9,No. 4,pp.297--305.

Vallabh, R. et al. (2022). Ultra-lightweight fiber-reinforced envelope material for high-altitude airship. *The Journal of The Textile Institute*, 113(9), 1799-1805. doi: 10.1080/00405000.2021.1948695.

Verheul, R. F., Breukels, J. & Ockels, W. J. (2009). Material selection and joining methods for the purpose of a high-altitude inflatable kite. *Proceedings of the Structures, Structural Dynamics, and Materials Conference*. doi: 10.2514/6.2009-2338.

Wang, F. et al. (2017). Experimental Study on Uniaxial Tensile and Welding Performance of a New Coated Fabric for Airship Envelopes. Retrieved from: JournalofIndustrialTextiles, Vol.46,No.7,pp.1474--1497.

Wang, J. T. & Nefske, D. J. (1988). A New CAL3D Airbag Inflation Model. *SAE Transactions*, 97(6), 697–706.

Wong, J. C. (2015). *Modeling of High Pressure Confined Inflatable Structures*. (Master's thesis, West Virginia University).

X, T. M. F. [Accessed on October 2, 2025]. (2024). Loon Project Collection.

Xu, K., Wen, Y. & Xu, X. (2023). Melt flow ratio: A way to identify the type of polyethylene. *Advanced Industrial and Engineering Polymer Research*, 6(1), 79–82. doi: 10.1016/j.aiepr.2022.08.001.

Yang, Y. et al. (2019). Design Method for Precise-Forming of Air-Supported Structures Considering Weld Seams. Retrieved from: Thin-WalledStructures,Vol.145, Article106397.

Zhai, H. & Euler, A. (2005a). Material challenges for lighter-than-air systems in high altitude applications. *AIAA 5th Aircraft Technology, Integration, and Operations (ATIO) Conference and 16th Lighter-Than-Air Systems Technology and Balloon Systems Conferences*.

Zhai, H. & Euler, A. (2005b). Material challenges for lighter-than-air systems in high altitude applications. *AIAA 5th ATIO and 16th Lighter-Than-Air Systems Technology and Balloon Systems Conferences*, pp. 1–12. doi: 10.2514/6.2005-7461.

Zhang, L. et al. (2019). Mission-Based Multidisciplinary Optimization of Solar-Powered Hybrid Airship. Retrieved from: EnergyConversionandManagement,Vol.185,pp.44--54.

Zhang, Y.-L., Xia, H., Kim, E. & Sun, H.-B. (2012). Recent developments in superhydrophobic surfaces with unique structural and functional properties. *Soft Matter*, 8(44), 11217–11231. doi: 10.1039/C2SM26517F.

Zhao, H., Chen, Z. & Chen, J. (2022). Optimisation analysis of reinforced cable distribution on the airship. *The Aeronautical Journal*, 126(1293), 607–616. doi: 10.1017/aer.2021.84.